RICE UNIVERSITY

High Angular Momentum Rydberg Wave Packets

by

Brendan Wyker

A Thesis Submitted
in Partial Fulfillment of the
Requirements for the Degree

Doctor of Philosophy

Approved, Thesis Committee:

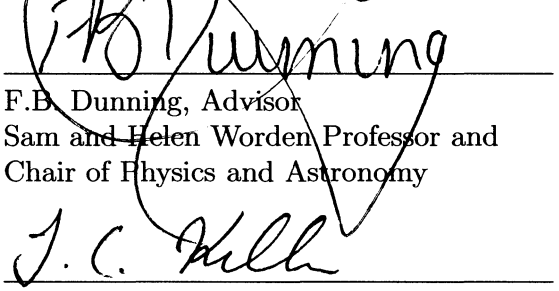

F.B. Dunning, Advisor
Sam and Helen Worden Professor and
Chair of Physics and Astronomy

T.C. Killian
Professor of Physics and Astronomy

D.M. Mittleman
Professor of Electrical and Computer
Engineering

Houston, Texas

April, 2011

High Angular Momentum Rydberg Wave Packets

Brendan Wyker

Abstract

High angular momentum Rydberg wave packets are studied. Application of carefully tailored electric fields to low angular momentum, high-n ($n \sim 300$) Rydberg atoms creates coherent superpositions of Stark states with near extreme values of angular momentum, ℓ. Wave packet components orbit the parent nucleus at rates that depend on their energy, leading to periods of localization and delocalization as the components come into and go out of phase with each other. Monitoring survival probability signals in the presence of position dependent probing leads to observation of characteristic oscillations based on the composition of the wave packet. The discrete nature of electron energy levels is observed through the measurement of quantum revivals in the wave packet localization signal. Time-domain spectroscopy of these signals allows determination of both the population and phase of individual superposition components. Precise manipulation of wave packets is achieved through further application of pulsed electric fields. Decoherence effects due to background gas collisions and electrical noise are also detailed. Quantized classical trajectory Monte-Carlo simulations are introduced and agree remarkably well with experimental results.

Acknowledgments

The work presented in this thesis could not have been accomplished without the help of many people. I would like to thank my advisor, Dr. Barry Dunning, for his guidance and insight during my time in his group. His leadership always keeps the project on task, directing the students to seriously think about the causes of any unexpected behavior and to verify the results of any experiment, simulation, or calculation. I have learned from him, among many other things, not to accept results without making sure they make physical sense.

I would like to thank Dr. Shuhei Yoshida for the extensive theoretical and computational work he has done to help us all understand the new phenomena we see in our work. His work is thorough and informative. Dr. Carlos Reinhold shares those qualities. He has been a patient teacher to me and our conversations and correspondence have been greatly appreciated. I would also like to thank Dr. Joachim Burgdörfer for his contributions to our work.

Among my coworkers in the lab Dr. Matthew Cannon spent the most time discussing physics (and any other topic) with me, allowing me an outlet for ideas and an informed response. I greatly value his friendship. Dr. Jeffrey Mestayer laid the groundwork for the experiments presented here. His work updating and improving

the apparatus and data acquisition systems made my work orders of magnitude easier. Dr. Leonard Suess was a valuable sounding board, and he kept the laser system running smoothly, even returning from time to time after leaving the lab to help us out. I would also like to thank Shuzhen Ye for his help running the apparatus and taking data.

I would like to thank my family for their support. My father has been a constant support for me over the years, and his example of professionalism and responsibility is one I work hard to follow.

Most importantly, I would like to thank my wife, Margaret. She has supported me unconditionally, showing infinite patience during my studies. I thank her for putting up with me after hard days at work and cheering me up every day. She knows that I love her and would follow her anywhere.

Contents

Figures

Chapter 1

Introduction

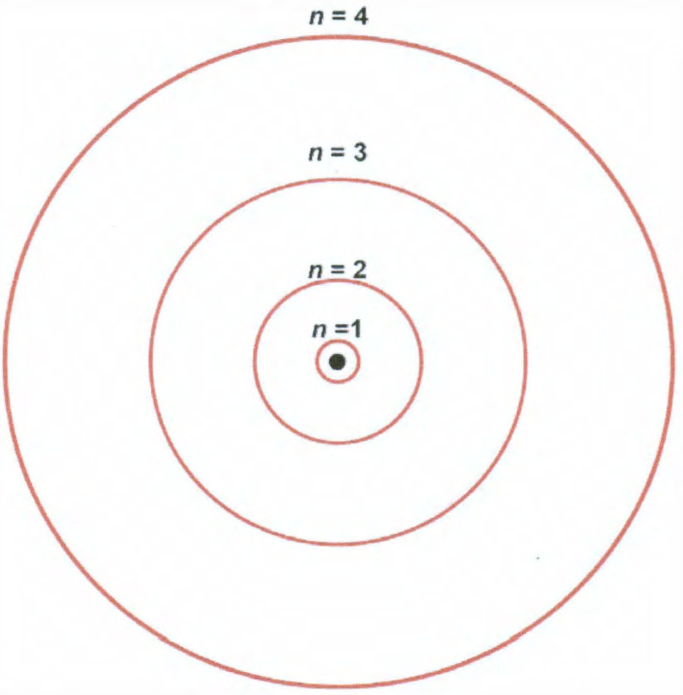

Figure 1.1 : Bohr model of Rydberg energy levels for Hydrogen. Orbital radii scale as n^2.

Rydberg atoms are defined as atoms with one or more electrons excited into a high-n state, where n represents the principal quantum number of the atom. Here, discussion will be limited to the case where only one electron, the valence electron of an alkali atom (potassium), is in an excited state. In terms of the classical Bohr theory

Table 1.1 : Scaling properties of Rydberg atoms.

Property	Scaling (a.u.)	$n = 1$	$n = 30$	$n = 306$
Mean Radius	n^2	5.3×10^{-9} cm	4.8×10^{-6} cm	5.0 μm
Orbital Period	$2\pi n^3$	1.5×10^{-4} ps	4.1 ps	4.3 ns
Binding Energy	$-1/2n^2$	-13.6 eV	-15 meV	-145 μeV
Energy Spacing	$1/n^3$	10.2 eV	1.0 meV	0.94 μeV
Classical Field Ionization Threshold	$1/16n^4$	3.0×10^8 V/cm	400 V/cm	38 mV/cm

the valence electron is excited to a high lying orbit of large radius as demonstrated in Fig. 1.1. Unlike electrons in the Bohr theory, however, electrons in quantum theory are described by distributions (wavefunctions) which may or may not be well localized, and are related to the probability of finding an electron in a given region. In fact, the radial extent of the electronic distribution in a Rydberg atom does indeed increase rapidly with n, reaching a classical diameter ~ 10 μm (the typical size of a biological cell) when $n = 306$. Table 1.1 outlines this dependence along with some of the more interesting characteristics of Rydberg atoms, with properties of the Hydrogen ground state, $n = 1$, given for comparison. Scaling equations are given in atomic units (see Sec. B.1), which are used throughout this text.

The sensitivity of Rydberg atoms to external magnetic and electric fields makes precise engineering of their electron wavefunctions into a wide array of final states possible. Wavefunction engineering, where coherent control of quantum matter is exercised, finds applications in a wide range of scientific study, *e.g.*, gas phase chemistry, nanophotonics, probing molecular dynamics, and quantum information processing [1–7]. More directly, Rydberg wavefunction control is also of interest in the study of antihydrogen, which is produced in high Rydberg states that must be controllably de-excited in order to remain trapped [8–11]. As will be discussed in Ch. 3, high angular momentum, *i.e.*, high-ℓ, Rydberg atoms have longer radiative lifetimes, larger magnetic dipole moments, and more narrowly defined collision velocities than low-ℓ states. These properties make production of such states desirable for research in information processing, cavity quantum electrodynamics, and precision spectroscopy [12–16]. To that end, a number of techniques have been devised for the production of high angular momentum *stationary states* [17–22], which are radially localized, but are spread in azimuth and do not evolve with time. The present work describes the production, characterization, and manipulation of high-ℓ wave packets that are radially localized and evolve in such a manner as to be intermittently localized in azimuth, resembling the classical Bohr atom.

Preparation of high-n Rydberg atoms is accomplished in the present work through a single photon transition from the ground, 4s, state of potassium. A property of photoexcitation is that for each photon absorbed an atom can only gain one unit

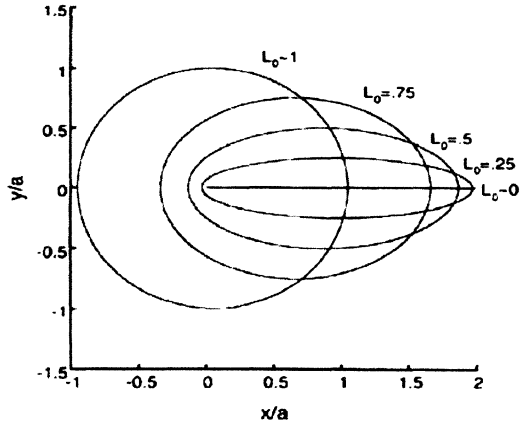

Figure 1.2 : Orbits of varying eccentricity in scaled units. Low L orbits are highly elliptical, while high L orbits are near circular. [23]

of angular momentum. Photoexcitation, then, populates only low-ℓ excited states, while the maximum value allowable for ℓ is $n-1$. A scaled angular momentum can then be defined as

$$L_0 = \frac{\ell}{(n-1)}, \tag{1.1}$$

for $n > 1$. Fig. 1.2 illustrates the shape of sample classical orbits with varying degrees of eccentricity. Low angular momentum states follow highly elliptical orbits, while maximum angular momentum is necessary in order to create a circular orbit. The low-ℓ states produced by photoexcitation are exposed to carefully tailored electric field pulses that break the symmetry of the Coulomb potential, allowing angular momentum precession, leading to the production of high-ℓ wave packets.

The most basic distinction between the classical and quantum descriptions of electron orbits is that a continuous distribution of energy is allowed classically, while

in quantum mechanics the energy of a bound electron must take discrete values. The behavior of a representative time dependent variable with a continuous frequency distribution is shown in Fig. 1.3, along with that of a variable with a similar, but discrete, frequency distribution. The components of each distribution are all initially in phase with each other, leading to a large amplitude of oscillation. Each component of the distributions, however, evolves at its own characteristic frequency leading to dephasing demonstrated by the reduction in amplitude of the oscillations with time. For a continuous distribution there is no later time at which all components rephase with each other (though smaller amplitude partial revivals may occur depending on the distribution). For the discrete distribution a time exists when all components will simultaneously rephase leading to what is termed a *quantum revival.* The components then continue to evolve at their characteristic rates and dephase once again.

The time scale for observation of quantum revivals depends on the difference in frequencies associated with the components of the wave packet, similar to a beat pattern in acoustics, $T_{rev} = (f_1 - f_2)^{-1}$. The frequency of each component arises from the difference between neighboring energy levels, $\omega_n = E_{n+1} - E_n = 1/n^3$. For large n, the difference between frequencies is small and the revival time can be approximated as

$$T_{rev} \approx \frac{2\pi}{\left|\frac{\partial}{\partial n}\frac{1}{n^3}\right|} = \frac{2\pi n^4}{3}. \tag{1.2}$$

For $n = 306$, this corresponds to a revival time of $T_{rev} \approx 440$ ns compared with ≈ 40 ps for $n = 30$.

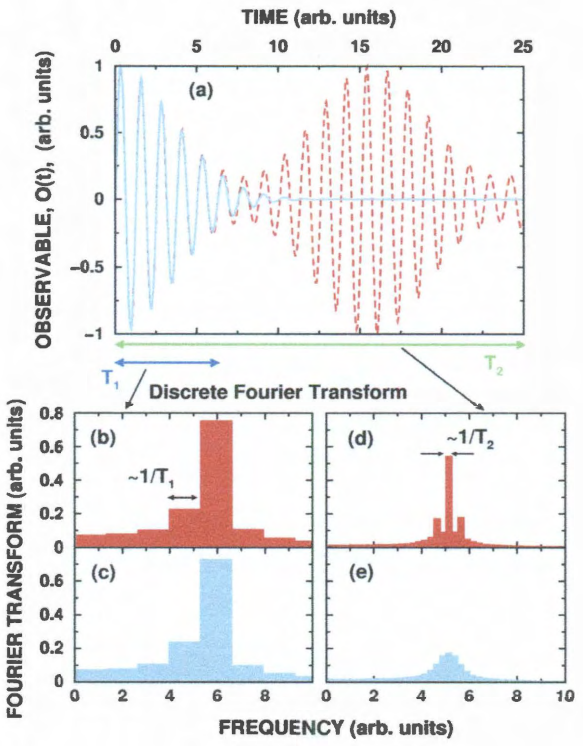

Figure 1.3 : (a) Continuous (——) and discrete (- - -) distributions. (b) and (c) Discrete Fourier transforms of the distributions taken over time T_1. The resolution is such that the distributions cannot be distinguished. (d) and (e) Discrete Fourier transforms taken over time T_2. The discrete nature of the distributions can be resolved. [24].

For times less than T_{rev} the discrete nature of the wave packet is undetectable. The frequency spectrum observable over a time interval, t, has a resolution $\Delta\omega \sim 2\pi/t$. If $\Delta\omega > \partial\omega_n/\partial n$ the overlapping frequency components will appear to be smoothed out as demonstrated in Fig. 1.3. Only when the distributions have been observed over a sufficiently long time can the differences be resolved. The high-ℓ wave packets produced in the present work are observed over microsecond time scales, with sub-nanosecond precision. This allows the resolution of frequencies smaller than the

differences between frequencies associated with orbits of neighboring high-n levels. Time-domain analysis, as discussed in Ch. 4, provides population and phase information with single n resolution, far superior to the capabilities of conventional n level population measurements, such as selective field ionization (see Ch. 3), at such high n. The n levels studied in the current work allow for observation of around 100 orbits of "classical" behavior while the continuous and discrete distributions mirror each other and the system can be modeled by purely classical calculations, followed by "quantum" behavior as the nature of the discrete distribution becomes evident. As such, $n \sim 300$ Rydberg atoms provide an attractive regime in which to study the transition from classical to quantum behavior. Compare this to $n = 30$, where only around 10 orbits of "classical" behavior can be observed, and techniques to probe on sub-picosecond time scales would be required.

Armed with detailed information about the initial conditions of these wave packets, protocols are demonstrated in Ch. 5 involving their precise manipulation into desired final states using high speed electric field pulses. Impulsive momentum kicks provided by half-cycle pulses (HCPs) act to narrow or broaden the n distributions of wave packets, while trains of such pulses inhibit dephasing, leading to the production of nondispersive Bohr-like wave packets. These nondispersive states are also produced using sine wave driving, and are transported to higher or lower n, near circular states by chirping the frequency of the sine driving from resonance with the initial state to that of the desired final state.

Due to interactions with the cloud of core electrons in a Rydberg atom, high-n electrons couple strongly to stray electric fields while in low-ℓ orbits. High-ℓ electrons, however, spend little or no time near the Rydberg core, making them robust against perturbations from background gas collisions and electrical noise. This dependence is studied in Ch. 6, showing strong insensitivity to background collisions. Application of synthesized electrical noise allows the study of effects from both inhomogeneous broadening and energy diffusion on the electron wave packet evolution. These studies further demonstrate the robustness of high-n, high-ℓ wave packets.

Overall, the present work demonstrates that with precise control of electric fields novel high-n, high-ℓ Rydberg electron wave packets can be produced, characterized, and manipulated. These wave packets display semi-classical behavior, providing insight about the classical to quantum transition, and are robust against external perturbations.

Chapter 2

The Experimental Apparatus

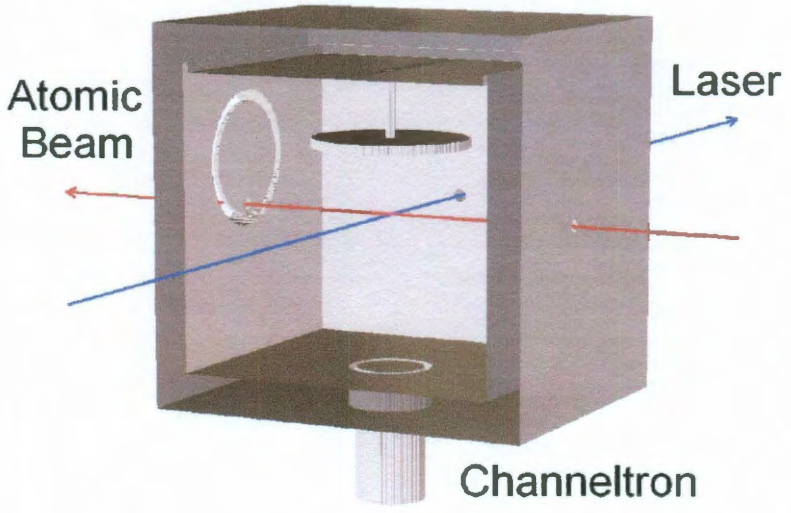

Figure 2.1 : Diagram of the apparatus with the front face removed for illustrative purposes. A UV laser pulse intersects a collimated alkali beam exciting high-n Rydberg states. Half-cycle electric field pulses (HCPs) and electric field steps are applied by the two electrodes, while the channeltron electron multiplier measures electrons resulting from field ionization.

As discussed in Ch. 3, Rydberg atoms, being composed of a loosely bound pair of charges, are quite susceptible to the effects of electric fields. Consequently, the control of such fields is of primary concern in their experimental study. The present experimental apparatus is a slight modification of that used with much success in previous studies of Rydberg atoms [25, 26]. It is comprised of three pairs of copper

plate electrodes arranged as a cube, which defines the interaction region. The electrodes are electrically isolated so they may be individually biased to reduce residual electric fields in the interaction region to $\lesssim 50\,\mu$V/cm. Two electrodes are also incorporated for the application of field steps and HCPs, along with a channeltron electron multiplier for the detection of field-ionized electrons.

High-n Rydberg atoms are produced in the interaction region via single photon excitation using a frequency doubled Coherent 699-21 CW Rhodamine 6G (Rh6G) dye laser whose output is chopped by an acousto-optic modulator into a train of $1\,\mu$s duration pulses. The laser is focused into the center of the interaction region where it intersects a thermal potassium beam originating from a potassium oven. Following excitation, the Rydberg atoms are subject to one or more carefully tailored electric field pulses. Surviving Rydberg atoms are measured by application of a field ionization pulse, after some delay, and the resulting electrons are detected by a Channeltron electron multiplier. Measurements with no HCPs applied are repeated at routine intervals to determine the number of Rydberg atoms initially created and obtain survival probabilities. Due to the low probability of Rydberg excitation during a given cycle, data are accumulated following many cycles to improve statistical accuracy. Experimental cycles are repeated approximately every $40\,\mu$s.

2.1 The Vacuum System

The vacuum system consists of two stainless steel chambers connected by a 0.7 mm aperture. An initial vacuum on the order of 10 mTorr is produced by a Welch Duo Seal mechanical backing pump. Next, a vacuum of 2.0×10^{-8} Torr is produced using Varian VHS-6 and VHS-4 diffusion pumps. Bayard-Alpert ionization gauges are located in each chamber to monitor pressure.

The source chamber houses the potassium beam oven and is pumped by the 4" diffusion pump. The oven contains a 5 g ampule of potassium. The body of the oven is heated to 300 °C by applying current to resistive heater cartridges inserted into the oven body. Heater cartridges are also placed in the nose of the oven which is heated to 345 °C; the temperature difference is maintained in order to prevent potassium from condensing on, and thereby clogging, the nose aperture. Thermocouples placed on the nose and body of the oven relay temperature information to a set of Omega CN9000A microprocessor temperature controllers which regulate the current applied to the heater cartridges.

Thermal radiation transfer from the oven to the rest of the apparatus is reduced through the use of heat shielding and water cooling. An aluminum heat shield surrounds the oven, reducing heat transfer and containing excess potassium vapor. The oven and heat shield are further surrounded by a copper enclosure, to which copper tubing has been brazed. Chilled water is routed by vacuum feed-throughs into the copper tubing.

Potassium exits the oven through a 0.38 mm aperture in the nose and travels approximately 10 cm before passing through the 0.7 mm aperture which leads to the main chamber. A rough estimate of the beam's angular divergence may then be calculated using the expression

$$\theta_d = 2arctan\Big(\frac{d_f - d_i}{2l}\Big), \tag{2.1}$$

where θ_d denotes the angular divergence, d_f and d_i denote the diameters of the two apertures, and l denotes the distance between the apertures. With the values given the angular divergence is estimated to be $\sim 0.2°$.

The velocity distribution of a thermal beam goes as [27]

$$f_{Beam}(v) \sim v^3 e^{-\frac{mv^2}{2k_bT}}, \tag{2.2}$$

where f_{Beam} is the Maxwell-Boltzmann velocity distribution. The number of Rydberg atoms produced during photoexcitation is proportional to the amount of time the atoms are exposed to the laser radiation. Slower moving atoms spend more time in the photoexcitation region and therefore have a larger probability of being excited to Rydberg levels. As such, the velocity distribution of Rydberg atoms scales as v^2, rather than v^3, and is given by

$$f_{Ryd}(v) = 4\pi\Big(\frac{m}{2\pi k_bT}\Big)^{\frac{3}{2}} v^2 e^{-\frac{mv^2}{2k_bT}}. \tag{2.3}$$

The first moment of the velocity distribution, $\langle v^n \rangle = \int v^n f(v)\, \mathrm{d}^3v$ with $n = 1$, yields an average velocity of

$$\overline{v} = \sqrt{\frac{8k_bT}{\pi m}}, \tag{2.4}$$

which, with the values given above, is $\overline{v} = 570$ m/s. Further characterization of the beam will be described as needed throughout the text.

The main chamber houses the interaction region (discussed in detail in Sec. 2.3) and is pumped by the 6" diffusion pump. Stray magnetic fields in the chamber are reduced by μ-metal shielding to values $\leq$ 20 mG. Laser light enters and exits the chamber through quartz windows set at Brewster's angle, preferentially passing vertically polarized light. All electrical signals are routed through the chamber using semi-rigid coaxial copper cables.

2.2 The Laser System

Essential to the creation of Rydberg atoms is precise control of the excitation laser system, an extracavity doubled CR-699-21 Rh6G dye laser. A Coherent Verdi V8 laser is used to pump this laser. Rh6G laser dye, dissolved in ethelyne glycol, acts as the lasing medium yielding approximately 1 W of laser radiation over a tunable wavelength range of $570 - 610$ nm. A Spectra-Physics Wavetrain frequency doubler is used to produce the near UV laser radiation needed for single photon Rydberg excitation.

The Verdi is a diode pumped solid state laser which reliably provides powerful and stable 532 nm pumping radiation, with a linewidth of 5 MHz and $< 0.03\,\%$ rms noise. The 7.5 W pump beam is focused into a jet of Rh6G flowing at approximately 10 m/s, expanding from a stainless steel nozzle into a flat laminar stream whose face

is oriented at Brewster's angle to the incoming pump beam in order to minimize reflection loss [28]. A 380 GHz bandwidth birefringent filter, a 225 GHz free spectral range (FSR) thin etalon, and a 10 GHz FSR thick etalon combine to produce single frequency operation. The efficiency of single frequency operation is enhanced through the use of a polarization rotating element referred to as an optical diode. This component ensures unidirectional operation through the use of optical activity and the Faraday effect, by slightly rotating the polarization of waves traveling in one direction, while leaving unchanged the polarization of waves traveling in the other direction [29]. Reflection losses at an intracavity Brewster plate then suppress the propagation of the unwanted traveling wave.

A portion of the CR-699 output beam is split off for use in active stabilization. Two detectors compare the intensities of an unmodified beam and one that passes through an oven stabilized Fabry-Perot interferometer containing a galvo driven Brewster plate, collectively known as the reference cavity. The interferometer output intensity varies with laser frequency providing the means to produce an error signal that is fed into the controls for varying the position of the intracavity Brewster plate and a piezoelectric-mounted cavity mirror. The position of the galvo driven Brewster plate, in the reference cavity, can be externally controlled allowing for a linear 30 GHz frequency scan. Active stabilization of the CR-699 maintains a linewidth of ≤ 500 kHz with a long term frequency drift of ≤ 50 MHz per hour.

Long-term stability is enhanced to ≤ 1 MHz per day by the Superlock system [30].

Another small portion of the CR-699 output is superposed with an orthogonally polarized beam from a Melles Griot frequency stabilized Helium-Neon laser (HeNe). This combination is directed into a Burleigh confocal scanning Fabry-Perot etalon with a FSR of 750 MHz, controlled by a Burleigh RC45 etalon controller. A piezoelectric transducer (PZT) scans one of the mirrors of the etalon leading to transmission peaks related to each laser's frequency. After passing through the etalon each beam is separately directed into a pair of photodiodes. Given a linear PZT response, the separation of a HeNe intensity peak from that of a CR-699 peak should be constant while the CR-699 is in a stable state. The PZT scan voltage at the time of each intensity peak is stored by a sample and hold circuit and the difference of the two values is compared to a reference voltage producing an error signal that is fed into the CR-699 control circuitry. Setting the reference voltage to a linear ramp enables frequency scans over a range of 800 MHz, while setting the reference voltage to a constant value allows for precise frequency locking. A scanning Michelson interferometer monitors the overall CR-699 wavelength [31].

The 1 W output of the CR-699 is then directed into the Wavetrain frequency doubler [32] producing, typically, $10 - 50$ mW of the near UV light needed for Rydberg excitation. A beta barium borate (BBO) crystal located in one arm of a triangular ring resonator is used as the nonlinear medium for second harmonic generation (SHG). Two curved mirrors and a PZT-mounted prism act as the vertices of the resonator. Phase matching, where the phase velocity of the harmonic wave matches that

of the fundamental wave in the nonlinear material, is necessary in order to maximize conversion efficiency. This is achieved through the use of the birefringence of the BBO crystal, in that the angular dependence of the refractive index of the crystal may be used to match the phases of the waves by varying their incident angles with the aid of the PZT-mounted prism. Optics located in between the CR-699 and the Wavetrain are used in the active resonator stabilization of the system. The Pound-Drever Hall [33] method is utilized by passing the incoming beam through an electro-optic modulator (EOM) and monitoring the superposition of signals with a photodiode. The EOM, driven by an electrical radio frequency (rf) signal, adds sidebands to the incident beam. A portion of the incident beam reflects off the resonator input mirror and interferes with a transmitted portion of the beam in the cavity. The rf modulation on the resulting beam is then measured by the photodiode. A double balanced mixer is used in the phase sensitive detection of the photodiode signal to produce the error signal used for active stabilization. The linewidth of the cavity is small enough that the rf sidebands are not transmitted into the cavity.

An Intra-Action acousto-optic modulator (AOM) then chops the beam into 1 μs pulses approximately every 40 μs. To do this the first order diffracted beam from the AOM, driven at a constant frequency, is kept while all other order beams are blocked. While the maximum intensity in the first order is less than that available in the zeroth order, a full extinction ratio is possible with the former while this is not possible with the latter. Steering mirrors then direct the beam through a lens and

into the interaction region via a Brewster window.

2.3 The Interaction Region

Three pairs of planar copper plate electrodes, 10 cm × 10 cm, comprise the basic structure of the interaction region (IR) as illustrated in Fig. 2.1. The separation of these large plates from the center of the IR helps to reduce the effect of patch fields caused by nonuniformities in the plate electrode surfaces, while bias potentials applied to these plates reduce stray electric fields near the center of the IR to $\lesssim 50\,\mu$V/cm [25]. Vertical plate pairs are biased with a *push-pull* system where each plate is given an equal but opposite bias potential. The top and bottom plates, however, are held at a constant potential. This is due to the location of the channeltron electron multiplier below the IR, which is accessed via a 1" diameter aperture in the bottom plate electrode covered by a fine copper mesh. More on this arrangement and the channeltron will be discussed in Sec. 2.4. A set of 0.1 μF capacitors connects the side plates to ground, thereby eliminating pickup of nearby rf signals by providing an rf-shunt. Apertures are located in the center of the four side walls to allow for the entrance and exit of the laser and the alkali atom beams. These beams cross, perpendicularly, in the center of the IR exciting high-n Rydberg states.

Hanging from the top plate of the IR is a 2" diameter, $\frac{1}{4}$" thick disk electrode. This electrode provides the bias for the vertical direction while also receiving electric field pulses, and is held in place, 1" above the center of the IR, by a semi-rigid copper

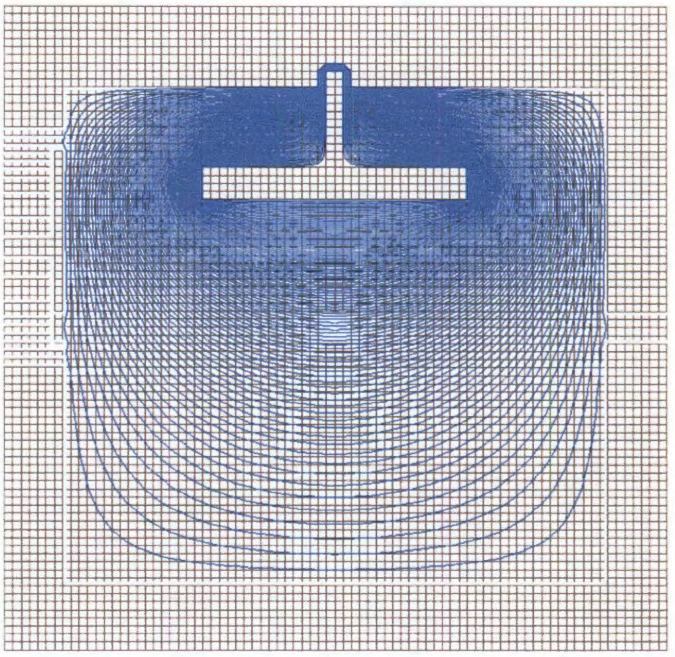

Figure 2.2 : A cross section of the IR with potential contours produced by applying an arbitrary potential to the top electrode while keeping all other surfaces grounded. Ninety contours are drawn equally spaced in potential from ground to the arbitrary potential applied on the top electrode.

coaxial cable. A 50 Ω resistor connects the electrode to the coax shield to minimize reflections while allowing pulse rise times as fast as 200 ps. Figure 2.2 shows the potential contours that result when a static potential is applied to the top electrode while keeping all other electrodes grounded. Of note are the spacing and relative flatness of the contours in the vicinity of the center of the IR.

The two dimensional kicking necessary for the measurement of circular states requires the presence of a side electrode in the IR. This electrode shares the bias of the surrounding side plate while independently receiving electric field pulses. As with

the top electrode, the uniformity and direction of the electric field produced by this electrode are important parameters. Other requirements are that the magnitude of the electric field produced be sufficient to probe the circular states and that the capacitance of the electrode, with respect to the large plate electrode it is near, be small enough to allow fast rise times for pulsed electric fields. The electric field produced by the side electrode should point horizontally so as to be perpendicular to the direction of fields produced by the top electrode. The placement and size of the top electrode, however, complicate the placement of the side electrode as its presence modifies the resulting potential contours. In order to direct the electric field horizontally at the center of the IR the side electrode must be offset upward. Numerical calculations were used to determine a reasonable compromise of field direction and strength resulting in a displacement of the side electrode upward by $\frac{5}{8}$", resulting in a field strength of 8% that of the top electrode and a field tipping of 3.6°. Figure 2.3 shows the potential contours that result when a static potential is applied to the side electrode while all other surfaces are held at ground.

The capacitance of the side electrode with respect to the surrounding plate electrode is roughly approximated using the parallel plate equation

$$C = \epsilon_o \frac{A}{d}, \tag{2.5}$$

where ϵ_o is the vacuum permittivity, A is the area of the edge of the side electrode, and d is the distance from the side electrode to the surrounding plate electrode. Here, $d = 3.18\,\text{mm}$, while the electrode radius is 19.1 mm, with an electrode thickness

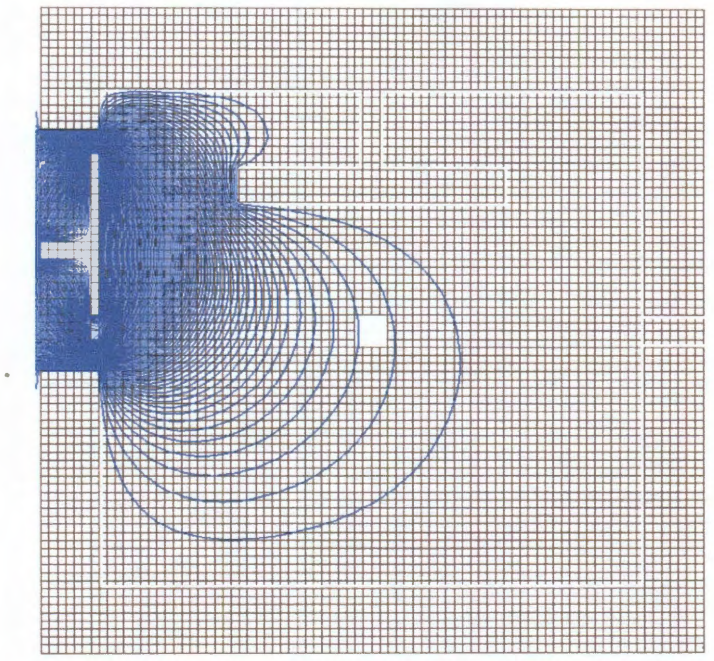

Figure 2.3 : A cross section of the IR with potential contours produced by applying an arbitrary potential to a side electrode, displaced upward from the center, while keeping all other surfaces grounded.

of 1.59 mm, yielding a side area of 190 mm^2, and a capacitance approximately $C =$ 0.5 pF. Just as with the top electrode, the side electrode has a 50 Ω resistor connecting it to the coax shield. This arrangement allows for pulse rise times around $\tau = RC =$ 25 ps.

2.4 Detection

A 1" aperture is located in the center of the bottom IR plate, covered by a series of fine mesh copper grids. Directly below these grids lies a Sjuts Optotechnik KBL

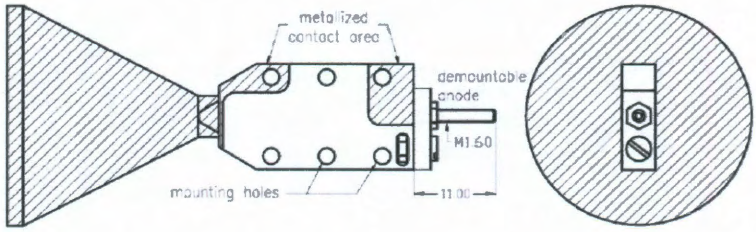

Figure 2.4 : Sjuts Optotechnik KBL 25RS channeltron electron multiplier schematic. The channeltron is used to detect electrons resulting from Rydberg atom ionization [34].

25RS channeltron channel electron multiplier (Fig. 2.4). To detect surviving Rydberg atoms a voltage ramp which rises from 0 to 5 V over a period of 5 μs is applied to the bottom plate, accelerating electrons into the funnel shaped aperture and curved channel of the channeltron. There, collisions with a hydrogen-reduced lead oxide glass lining produce an avalanche of secondary electron emissions. With a bias across the channeltron of 3 kV, up to 10^8 electrons can be produced from this process [34] which, upon collection by the anode, trigger an output pulse to an Amptek A101 amplifier/comparator. The A101 acts as a discriminator and amplifier reducing the number of spurious counts and improving the signal to noise ratio. The A101 outputs to an Ortec 566 time to amplitude converter (TAC) whose output ranges from 0 to 10 V based on the duration from the beginning of the ramp to the time of the A101 signal. An analog to digital converter then passes the result to the computer for processing.

Though Rydberg ionization is a complex process, whose details may be found elsewhere [35, 36, for example], Rydberg atom binding energies scale roughly as $-1/2n^2$, while classical ionization thresholds scale as $1/16n^4$. With a linear field ramp the above-mentioned technique allows for time sensitive, and therefore field sensitive, detection. This method forms the basis of selective field ionization (SFI), where the state of a Rydberg atom can be determined based on the field required for ionization.

Previous work on the apparatus [23] shows that the low energy electrons produced by photoionization during the UV Rydberg excitation pulse, and by the applied HCPs, might remain in the IR for up to $5\,\mu$s. Thus, in order to obtain accurate survival probabilities the field ramp is applied $6\,\mu$s after the UV Rydberg excitation pulse, and the TAC start pulse is slightly delayed from the start of the field ramp. This way any free electrons from the initial Rydberg excitation, or those produced during the course of the experiment, are not counted in the determination of the overall survival probabilities. As stated before, the experimental cycle is repeated approximately every $40\,\mu$s. Experimental runs, during which HCPs and field steps are applied to the atoms, alternate with calibration runs, during which no HCPs are applied, in order to determine survival probabilities. Due to the low Rydberg excitation probability of a given cycle, data from many cycles are accumulated to produce meaningful statistics.

2.5 Electric Field Pulses

Electric field steps, HCPs, pulse trains and sinusoidal signals are produced using a set of high speed pulse and wave generators. A Hewlett Packard 8131A pulse generator is used for field steps, including the pump pulse to be described in Ch. 4. This generator is capable of producing up to 5 V pulses with rise times < 200 ps. A Picosecond Pulse Labs 10,050A pulse generator is used for the production of HCPs and ionizing field steps. This generator is capable of 45 ps rise times and pulses up to 10 V over a duration of 100 ps to 10 ns. An Advantest D3173 Pulse Pattern Generator is used to produce trains of HCPs and synthesized noise, with rise-times around 90ps. Its internal clock frequency can be set from 50MHz to 3.2GHz, which defines the width of a bin. Bins are logical 1's or 0's with an amplitude (fixed during a sequence) adjustable between $\sim$ 0.5V and 2V in 10mV steps. Patterns ("words") can be programmed composed of from 1024 to 65536 bins, or the generator can be run in the pseudo-random binary sequence (PBRS) mode for the generation of noise. A Chase Scientific DA12000 Arbitrary Waveform Generator operates similarly, but allows for changes in amplitude for each time bin. The DA12000 provides signals for the sine wave driving experiments to be discussed in Ch. 5. These pulse generators are triggered by a Stanford Research Systems DG535 Digital Delay Generator with up to 5 ps resolution.

Pulse strengths are adjusted through the use of fixed and rotary attenuators. Potential to field conversion is determined experimentally by varying the signal strength

of short ($T_p \ll T_n$) HCPs while monitoring Rydberg atom survival probabilities. The potential required for 50% ionization has been shown [37] to correspond to a scaled momentum transfer of $\Delta p_0 = n^{-1}$ (see B.2) in this limit.

Chapter 3

Theory and Simulations

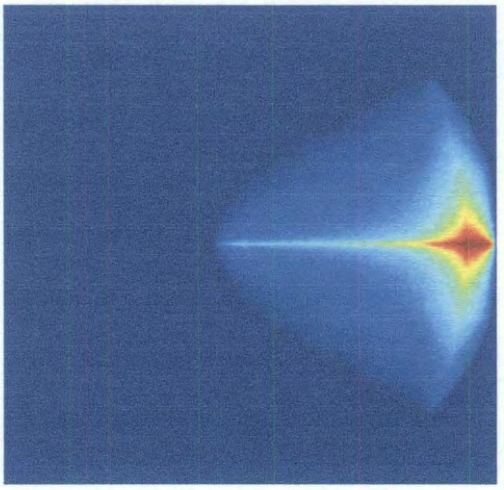

Figure 3.1 : Classical trajectory Monte Carlo simulation of a spatial electronic probability distribution for a quasi-one dimensional state. The nucleus is located in the center of the figure.

The spacing between the discrete energy levels of Rydberg atoms becomes very small with increasing n, scaling as n^{-3}. As this spacing decreases, electronic orbits more closely match their classical approximations and become amenable to semi-classical description. Rydberg electron dynamics are, therefore, described to high accuracy using a classical model of Kepler orbits, modified where appropriate with quantum corrections. The effects of electric fields both from the ionic core and from external sources dominate the behavior of the orbits and can be used to manipulate

distributions of trajectories into desired states. The accuracy of the semi-classical description makes possible simulation of the system by classical propagation of electron trajectories in the presence of a model core potential and classical fields. This is the basis of the classical trajectory Monte Carlo (CTMC) approach, wherein initial conditions for trajectories are randomly sampled from an ensemble weighted by a phase space distribution formulated to model the electronic wavefunction. Further refinement of the CTMC method is achieved through *ad hoc* discretization of energy levels at specific times during the evolution of a trajectory, making possible the prediction of quantum revival behavior. Quantized classical trajectory Monte Carlo (QCTMC) simulations are also developed, which accurately model the effects of inhomogeneous broadening and energy dispersion on classical trajectories with discretized energies.

3.1 Rydberg Basics

3.1.1 Orbital Characteristics

The single electron in a hydrogen atom experiences a potential $V = -1/r$, where r denotes the separation of the electron from the nucleus. The resulting Hamiltonian in atomic units is

$$H_{at} = \frac{\vec{p}^{\,2}}{2} - \frac{1}{r}, \tag{3.1}$$

where $\vec{p}$ denotes the momentum of the electron. For system energies $E < 0$, solutions of this Hamiltonian are closed elliptical or circular orbits in a plane, with conserved angular momentum, $\vec{L} = \vec{r} \times \vec{p}$. The eccentricity of the orbit is de-

fined as $\varepsilon = \sqrt{1 - 2|E|L^2}$, and is related to the scaled, unitless angular momentum $L_0 = L\sqrt{2|E|} = \sqrt{1 - \varepsilon^2}$. Orbits with $L_0 \sim 0$ are highly elliptical, while orbits with $L_0 \sim 1$ are near circular. The equation of an elliptical orbit in polar coordinates is given by [38]

$$r = \frac{L^2}{1 + \varepsilon \cos\theta}. \tag{3.2}$$

Another conserved quantity in the $1/r$ potential is the Runge-Lenz vector, $\vec{A}$, defined as

$$\vec{A} = \vec{p} \times \vec{L} - \hat{r}. \tag{3.3}$$

The magnitude of the Runge-Lenz vector in atomic units is the eccentricity, ε, of the orbit, while the direction is from the nucleus toward the point of closest approach (pericenter) of the orbit. Since $\vec{A} \cdot \vec{L} = 0$, the Runge-Lenz vector lies in the plane of the orbit, always perpendicular to $\vec{L}$.

For highly elliptical orbits electrons in non-hydrogenic atoms penetrate the ionic core formed by the nucleus and core electrons. The resulting polarization of the core, as well as the change in effective potential due to the unshielded core, result in increased binding, and therefore decreased energy, of the Rydberg electron. To account for this an empirically determined quantum defect, δ_ℓ, is introduced, modifying the electron energy levels

$$E = \frac{-1}{2(n - \delta_\ell)^2}. \tag{3.4}$$

The quantum defect varies greatly with angular momentum, but is relatively insensitive to n. Table 3.1 shows quantum defects for some alkali-metal atoms. At high-n,

Table 3.1 : Quantum defects of alkali atoms [36].

Atom	$\ell = 0$	$\ell = 1$	$\ell = 2$	$\ell = 3$
Li	0.40	0.04	0.00	0.00
Na	1.35	0.86	0.02	0.00
K	2.18	1.71	0.28	0.01
Rb	3.13	2.65	1.35	0.02
Cs	4.05	3.57	2.47	0.03

Eq. 3.4 can be approximated as

$$E \approx -\frac{1}{2n^2} - \frac{\delta_\ell}{n^3}. \tag{3.5}$$

The potential experienced by the electron as it penetrates the core remains central in character, meaning that the orbital angular momentum, $\vec{L}$, is still conserved. The Runge-Lenz vector, however, is no longer a conserved quantity [39]. As the angular momentum and energy determine the eccentricity, this leaves the direction of the Runge-Lenz vector as the quantity that varies. The resulting orbits retain their eccentricity, while the pericenter of the orbit precesses around the atom as shown in Fig. 3.2.

Averaged over a Kepler period the direction of the electric dipole moment of a Rydberg atom will point toward the pericenter of the orbit, $\hat{A}$. The magnitude of the electric dipole moment, averaged over the same period, is given by the magnitude of

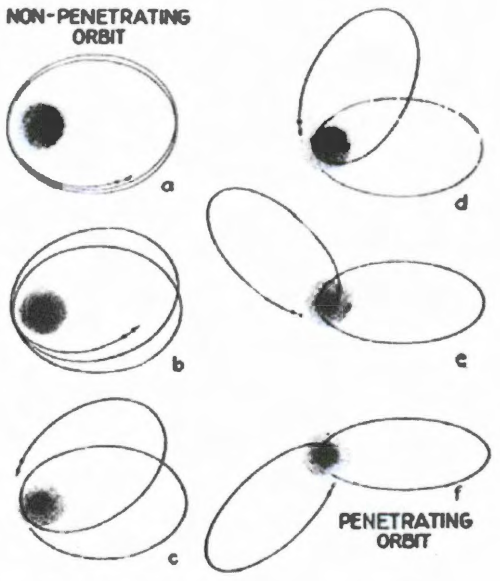

Figure 3.2 : Change of orbital precession with increasing core penetration for non-hydrogenic atoms [40].

the average position, $|\langle\vec{d}\rangle| = |\langle\vec{r}\rangle|$. In spherical coordinates

$$\begin{aligned} |\langle\vec{d}\rangle| &= \frac{1}{\tau}\int_0^\tau r\cos\theta\,\mathrm{d}t \\ &= \frac{1}{2\pi n^3}\int_{-\pi}^{\pi} r\cos\theta\,\frac{1}{\dot{\theta}}\,\mathrm{d}\theta \\ &= \frac{1}{2\pi n^3}\int_{-\pi}^{\pi} \frac{r^3}{r^2\dot{\theta}}\cos\theta\,\mathrm{d}\theta \\ &= \frac{L^5}{2\pi n^3}\int_{-\pi}^{\pi} \frac{\cos\theta}{(1+\varepsilon\cos\theta)^3}\,\mathrm{d}\theta \\ &= \frac{3}{2}n^2\varepsilon. \end{aligned} \tag{3.6}$$

Eq. 3.2 and $r^2\dot{\theta} = L$ are used in the fourth line, and the definition of the eccentricity, $\varepsilon = \sqrt{1 - L^2/n^2}$, is used in the last line. Since $|\vec{A}| = \varepsilon$ the time averaged vector

electric dipole moment is

$$\langle \vec{d} \rangle = \frac{3}{2} n^2 \langle \vec{A} \rangle. \tag{3.7}$$

Low-ℓ Rydberg atoms, where $|\vec{A}| \approx 1$, have large electric dipole moments, while circular states will have $\langle |\vec{d}| \rangle = 0$.

The case is reversed for the magnetic dipole moment. Here, the moment is given by

$$\vec{\mu} = I\vec{S}, \tag{3.8}$$

where $I = 1/2\pi n^3$ is the current of the loop produced by the electron orbit, and $\vec{S}$ is the area swept out by that orbit. The area of an ellipse is given by $\pi a^2\sqrt{1-\varepsilon^2}$, or with Eq. 1.1, $\pi a^2 \ell/n$, where a is the semimajor axis of the ellipse, which scales as n^2. Low-ℓ states, where $\varepsilon \approx 1$, sweep out almost no area and have exceedingly small magnetic dipole moments. The moment of a non-zero angular momentum state is given in atomic units by

$$|\vec{\mu}| = \frac{1}{2\pi n^3} \frac{\pi (n^2)^2 \ell}{n} = \frac{\ell}{2}, \tag{3.9}$$

directed perpendicular to the plane of the orbit. High-ℓ states ($\varepsilon \approx 0$, $\ell \sim n$), then, have magnetic dipole moments $\sim n/2$. Due to the linear n scaling, studies requiring large magnetic dipole moments require very-high-n circular states, such as those presented in this work.

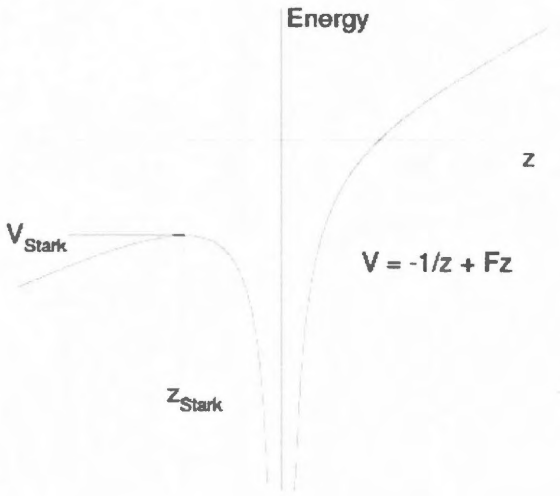

Figure 3.3 : Potential energy for an electron in a uniform, static electric field applied in the z direction.

3.1.2 Static Electric Fields

When a uniform, static electric field, F, is applied in the z direction, the $1/r$ Coulomb potential is tilted, resulting in a modified potential for the orbit, given by

$$V = -\frac{1}{r} + Fz, \tag{3.10}$$

as shown in Fig. 3.3. A saddle point is located on the z axis at $z_s = -1/\sqrt{F}$, with potential $V = -2\sqrt{F}$. Classical ionization occurs above this barrier, at a threshold field of

$$F_{thresh} = \frac{E^2}{4} = \frac{1}{4}\frac{1}{(2n^2)^2} = \frac{1}{16n^4}, \tag{3.11}$$

as stated in Table 1.1. The Stark Hamiltonian is then,

$$H_{Stark} = H_{at} + Fz, \tag{3.12}$$

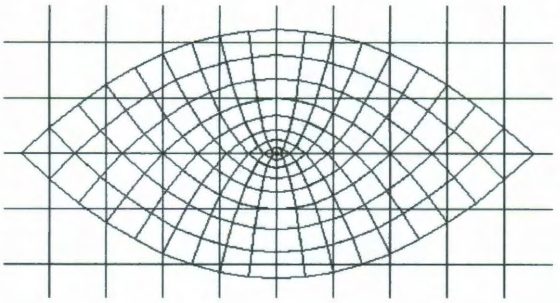

Figure 3.4 : A sample of the parabolic coordinate system. ξ represents downward facing parabolas, while η represents upward facing parabolas [41].

where H_{at} is the free-atom Hamiltonian. The energy shift for an atom with electric dipole moment, $\vec{d}$, is

$$\Delta E = -\vec{d} \cdot \vec{F}. \tag{3.13}$$

When dealing with electric fields, it is useful to transform to parabolic coordinates, (η, ξ, ϕ). Setting

$$\begin{aligned} x &= \sqrt{\xi\eta}\cos\phi, \\ y &= \sqrt{\xi\eta}\sin\phi, \\ z &= \frac{\xi - \eta}{2}, \\ r &= \frac{\xi + \eta}{2}. \end{aligned} \tag{3.14}$$

The coordinates ξ and η define confocal parabolas that are rotated about the z axis. $\xi = 0$ corresponds to the $-z$ axis, while $\eta = 0$ corresponds to the $+z$ axis. Figure 3.4 illustrates a 2D example of the parabolic coordinate system.

Casting the above potential in parabolic coordinates,

$$V(\xi,\eta,\phi) = -\frac{2}{\xi+\eta} + \frac{F(\xi-\eta)}{2}, \tag{3.15}$$

it is possible to obtain a separable solution to the Schrödinger equation, even with the electric field, while this cannot be done in spherical coordinates. The Schrödinger equation becomes

$$\left(-\frac{\nabla^2}{2} - \frac{2}{\xi+\eta} + \frac{F(\xi-\eta)}{2}\right)\Psi = E\Psi, \tag{3.16}$$

with

$$\nabla^2 = \frac{4}{\xi+\eta}\frac{\partial}{\partial\xi}\left(\xi\frac{\partial}{\partial\xi}\right) + \frac{4}{\xi+\eta}\frac{\partial}{\partial\eta}\left(\eta\frac{\partial}{\partial\eta}\right) + \frac{1}{\xi\eta}\frac{\partial^2}{\partial\phi^2}. \tag{3.17}$$

Assuming a separable solution, $\Psi(\xi,\eta,\phi) = u_1(\xi)u_2(\eta)e^{\pm m\phi}$, yields

$$\begin{aligned}
&\frac{d}{d\xi}\left(\xi\frac{du_1}{d\xi}\right) + \left(\frac{E\xi}{2} + Z_1 - \frac{m^2}{4\xi} - \frac{F\xi^2}{4}\right)u_1 = 0 \\
&\frac{d}{d\eta}\left(\eta\frac{du_2}{d\eta}\right) + \left(\frac{E\eta}{2} + Z_2 - \frac{m^2}{4\eta} + \frac{F\eta^2}{4}\right)u_2 = 0,
\end{aligned} \tag{3.18}$$

where the separation constants Z_1 and Z_2 are related by $Z_1 + Z_2 = 1$. These constants are known as the effective charges binding the electrons in the ξ and η coordinates [36]. It is convention to solve this system in the zero field limit and use perturbation theory to determine the effects of the field on the solution. Quantum numbers n_1 and n_2 are introduced to describe the zero field hydrogenic parabolic states. These quantum numbers are not fully independent, following the relation

$$n = n_1 + n_2 + |m| + 1, \tag{3.19}$$

and determine the effective charges

$$Z_1 = \frac{1}{n}\Big(n_1 + \frac{|m|+1}{2}\Big),$$
$$Z_2 = \frac{1}{n}\Big(n_2 + \frac{|m|+1}{2}\Big). \tag{3.20}$$

The quantum numbers n_1 and n_2 also relate to the expectation value of the component of the Runge-Lenz vector along the field [39],

$$\langle A_z \rangle = -\frac{n_1 - n_2}{n} \equiv -\frac{k}{n}, \tag{3.21}$$

where the electric quantum number, $k = n_1 - n_2$, has been introduced.

Using the approximate form of the Laguerre polynomials an approximate, unnormalized wavefunction may be written [35]

$$\psi_{nn_1n_2m} \sim e^{im\phi}\xi^{n_1+|m|/2}\eta^{n_2+|m|/2}e^{-(\xi+\eta)/2n}. \tag{3.22}$$

Squaring the absolute value and reverting back to polar coordinates yields the electronic probability distribution [35]

$$|\psi_{nn_1n_2m}|^2 = r^{2n-2}(1+\cos\theta)^{2n_1+|m|}(1-\cos\theta)^{2n_2+|m|}e^{-2r/n}. \tag{3.23}$$

A distribution similar to this is illustrated in Fig. 3.5 for $n = 8$, $m = 0$, and $n_1 - n_2 = -7, \ldots, 7$. Notice that for the extreme Stark states a permanent dipole moment exists.

The energy levels in the field are given to second order by [42]

$$E = -\frac{1}{2n^2} + \frac{3}{2}n(n_1 - n_2)F - \frac{1}{16}n^4F^2[17n^2 - 3(n_1 - n_2)^2 - 9m^2 + 19]. \tag{3.24}$$

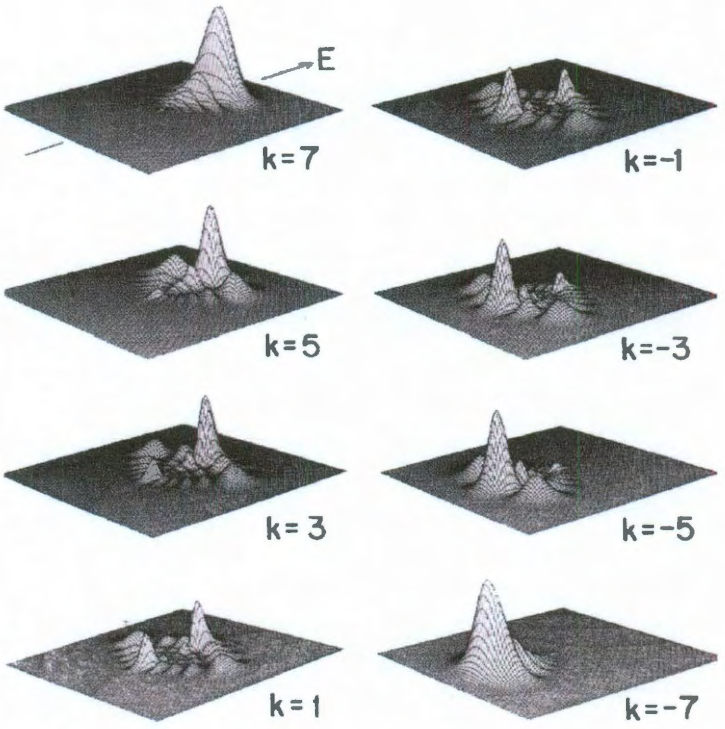

Figure 3.5 : Charge distribution for the parabolic eigenstates of H : $n = 8, m = 0, k = n_1 - n_2 = -7$ to $+7$. The asymmetry of the charge distribution for the extreme Stark states leads to a permanent dipole moment. E represents the electric field. [36] (modified).

The first term is recognized as the field-free hydrogen energy, while the second and third terms are the first and second order effects of the electric field. The second order term lifts the m degeneracy, while for circular states, $|m| = n - 1$, $n_1 = n_2 = 0$, the first order term vanishes. Figure 3.6 shows an example of the Stark energy level structure for the $|m| = 1$ states of hydrogen, where the effects of the electric field on the degenerate zero field energy states can be observed. Focusing on the first order Stark correction in Eq. 3.24, we see a level splitting of $\Delta E = 3n(n_1 - n_2)F/2$.

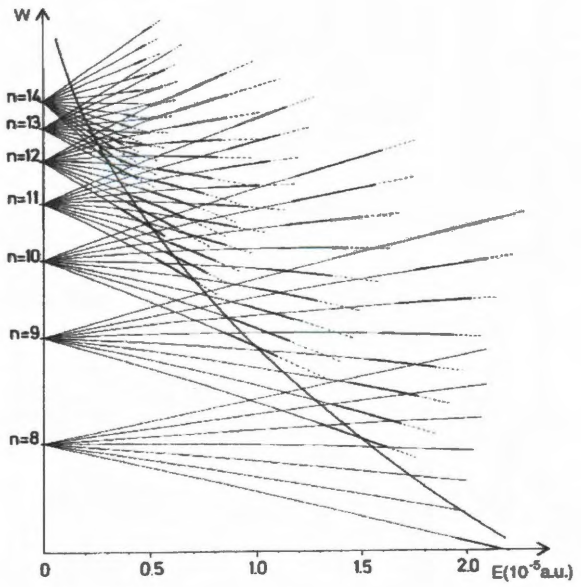

Figure 3.6 : Stark structure and field ionization properties of the $|m| = 1$ states of the H atom. Here the label W represents the energy E, while the label E represents the field F. The saddle point limit $E_c = -2\sqrt{F}$ is shown by a heavy curve. Field broadened Stark states appear approximately only for $E > E_c$. Dashed lines represent field ionized states [35].

Notice that this energy shift is equivalent to that obtained considering the effect of an electric field on a dipole, Eqs. 3.13 and 3.7, and inserting Eq. 3.21. The first order separation between Stark energy levels (the smallest Δk is 2 for fixed n and m) is called the Stark frequency, and is given by

$$\omega_s = 3nF. \tag{3.25}$$

An alternate separation of variables [35], with $u_1(\xi) = \chi_1(\xi)/\sqrt{\xi}$ and $u_2(\eta) =$

$\chi_2(\eta)/\sqrt{\eta}$, can be performed yielding effective potentials

$$V(\xi) = 2\Big(-\frac{Z_1}{\xi} + \frac{m^2-1}{4\xi^2} + \frac{F\xi}{4}\Big),$$
$$V(\eta) = 2\Big(-\frac{Z_2}{\eta} + \frac{m^2-1}{4\eta^2} - \frac{F\eta}{4}\Big). \tag{3.26}$$

Neglecting the short range $1/\eta^2$ term, a saddlepoint in η will occur for $\eta = \sqrt{4Z_2/F}$. Setting the energy, E, equal to $V(\eta)$ at the saddlepoint determines an ionization threshold, $F = E^2/4Z_2$. Red-shifted states, oriented against the field (in the direction of the saddlepoint), have $n_1 - n_2 \sim -n$, resulting in $Z_2 \sim 1$, whereas blue shifted Stark states are oriented with the field (away from the saddlepoint). The energy for $m = 0$ with a linear Stark effect for red-shifted states is, then,

$$E = -\frac{1}{2n^2} - \frac{3n^2F}{2}. \tag{3.27}$$

Substituting the above ionization threshold, with $Z_2 = 1$ into Eq. 3.27, solving for the energy, and substituting that result back into the threshold equation yields

$$F = \frac{1}{9n^4}. \tag{3.28}$$

This threshold takes into account the Stark shift of the levels, whereas Eq. 3.11 does not. It is not straightforward to estimate the ionization threshold for the blue-shifted Stark states, but blue and red states of the same n and m have threshold fields differing by approximately a factor of 2 [35]. The dashed lines in Fig. 3.6 represent ionization thresholds for Stark shifted states.

Red-shifted Stark states form the low energy (tighter binding) portion of each manifold ($n_1 - n_2 \sim -n$), while blue-shifted Stark states form the high energy portions

of the manifolds ($n_1 - n_2 \sim n$). The field at which the highest energy levels of an n state cross the lowest energy levels of the neighboring $n+1$ state can be approximated with the first two terms of Eq. 3.24,

$$\begin{aligned} -\frac{1}{2(n+1)^2} + \frac{3}{2}(n+1)[-(n+1)]F = -\frac{1}{2n^2} + \frac{3}{2}n^2F, \quad &\Rightarrow \\ -\frac{1}{2(n+1)^2} + \frac{1}{2n^2} = \frac{3}{2}\left((n+1)^2 + n^2\right)F, \quad &\Rightarrow \\ \frac{1}{n^3} \approx 3n^2F, \quad &\Rightarrow \\ F \approx \frac{1}{3n^5}. \quad &(3.29) \end{aligned}$$

In zero field, the ionic core reduces the energy levels, as in Eq. 3.4, but it does not effect the spherical symmetry of the problem. In the presence of an external electric field, however, that symmetry is lost and neighboring states may couple through overlap near the core. This coupling leads to avoided crossings as illustrated in Fig. 3.7. Calculation of the off-diagonal matrix elements used to determine the size of the avoided crossings is non-trivial, but it can be shown that for high n, low m states the avoided crossings exhibit an n^{-4} scaling [35]. States of the same n couple most strongly, as demonstrated in Fig. 3.7 by the large deflection of the 15d state as it nears the $n = 15$ manifold. States of adjacent n levels also couple, though not as strongly. Fig. 3.7 shows the 16d state, after having been deflected by the $n = 16$ manifold, avoiding the extreme blue shifted states of the $n = 15$ manifold. Coupling between n levels that are not nearest-neighbors is increasingly weak. The 17p state shows little deflection due to the $n = 15$ manifold, but appears to avoid the $n = 16$

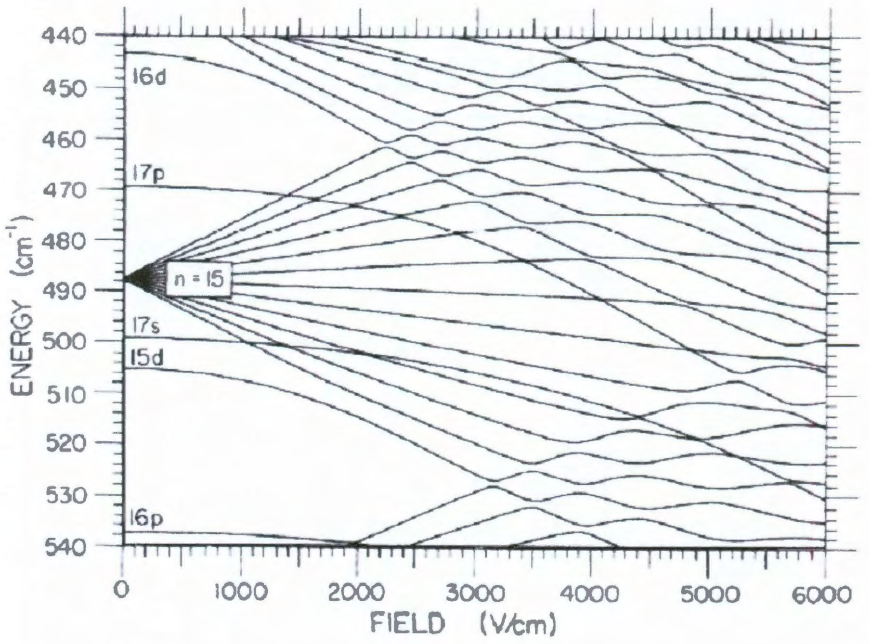

Figure 3.7 : Stark map of K, $|m = 0|$ states, showing avoided crossings in the vicinity of $n = 15$. [43]

manifold. Production of the quasi-1D states discussed in Sec. 3.1.5 takes advantage of the coupling between levels with sufficiently large excitation probability and those with large permanent electric dipole moments.

3.1.3 Stark Precession

The presence of the electric field acts both to set a preferred quantization axis and to eliminate the spherical symmetry of the potential. The angular momentum is no longer conserved, and Hamilton's equations

$$\begin{aligned} \dot{\vec{p}} &= -\nabla H, \\ \dot{\vec{r}} &= \nabla_p H, \end{aligned} \tag{3.30}$$

where ∇_p denotes the derivatives with respect to momentum, describe the resulting dynamics well [39]. Writing the Hamiltonian as $H = H_{Coulomb} - V_F(\vec{r})$, where $H_{Coulomb}$ and $V_F(\vec{r})$ are the pure Coulomb Hamiltonian and electric field potential, respectively, the change in angular momentum becomes

$$\begin{aligned}
\dot{\vec{L}} &= \dot{\vec{r}} \times \vec{p} + \vec{r} \times \dot{\vec{p}} \\
&= -\vec{r} \times [\nabla H_{Coulomb} - \nabla V_F(\vec{r})] \\
&= \dot{\vec{L}}_{Coulomb} + \vec{r} \times \nabla V_F(\vec{r}) \\
&= \vec{r} \times \nabla V_F(\vec{r}) \\
&= -\vec{r} \times \vec{F}, \qquad (3.31)
\end{aligned}$$

where $L_{Coulomb}$ is the conserved angular momentum of the pure Coulomb potential, and the relation $\vec{F} = -\nabla V_F(\vec{r})$ has been used in the last step. Time averaging over the Kepler orbit yields

$$\begin{aligned}
\langle \dot{\vec{L}} \rangle &= -\langle \vec{r} \times \vec{F} \rangle \\
&= -\langle \vec{r} \rangle \times \vec{F} = \langle \vec{d} \rangle \times \vec{F} \\
&= \frac{3}{2} n^2 \langle \vec{A} \rangle \times \vec{F}. \qquad (3.32)
\end{aligned}$$

The Runge-Lenz vector evolves as

$$\begin{aligned}
\dot{\vec{A}} &= \dot{\vec{p}} \times \vec{L} + \vec{p} \times \dot{\vec{L}} - \dot{\hat{r}} \\
&= [-\nabla H_{Coulomb} + \nabla V_F(\vec{r})] \times \vec{L} + \vec{p} \times \dot{\vec{L}} - \dot{\hat{r}} \\
&= (-\nabla H_{Coulomb} \times \vec{L} - \dot{\hat{r}}) - \vec{F} \times \vec{L} + \vec{p} \times \dot{\vec{L}} \\
&= \dot{\vec{A}}_{Coulomb} - \vec{F} \times \vec{L} + \vec{p} \times \dot{\vec{L}} \\
&= -\vec{F} \times \vec{L} + \vec{p} \times \dot{\vec{L}}, \qquad (3.33)
\end{aligned}$$

where $\vec{A}_{Coulomb}$ is the conserved Coulombic Runge-Lenz vector. It is instructive to time average Eq. 3.33 by term. Expanding the second term

$$\begin{aligned}
\vec{p} \times \dot{\vec{L}} &= \vec{p} \times (-\vec{r} \times \vec{F}) \\
&= -\vec{r}(\vec{p} \cdot \vec{F}) + \vec{F}(\vec{p} \cdot \vec{r}), \qquad (3.34)
\end{aligned}$$

we see that $\vec{p} \cdot \vec{r} = \frac{1}{2}\frac{\mathrm{d}}{\mathrm{d}t} r^2$ will average to zero over an orbit as it is an exact differential of an even function. Another quantity that will average to zero over an orbit is the exact differential [39]

$$\frac{\mathrm{d}}{\mathrm{d}t}[\vec{r}(\vec{r} \cdot \vec{F})] = \vec{r}(\vec{p} \cdot \vec{F}) + \vec{p}(\vec{r} \cdot \vec{F}), \qquad (3.35)$$

which implies that $\langle \vec{r}(\vec{p} \cdot \vec{F}) \rangle = -\langle \vec{p}(\vec{r} \cdot \vec{F}) \rangle$. The triple product expansion of the first term in the last line of Eq. 3.33 is

$$\begin{aligned}
\vec{F} \times \vec{L} &= \vec{F} \times (\vec{r} \times \vec{p}) \\
&= \vec{r}(\vec{p} \cdot \vec{F}) - \vec{p}(\vec{r} \cdot \vec{F}) \\
&= 2\vec{r}(\vec{p} \cdot \vec{F}). \qquad (3.36)
\end{aligned}$$

Leaving $\vec{F} \times \vec{L}$ as it is in Eq. 3.33 and combining Eqs. 3.34 and 3.36 yields a time averaged value for the change in the Runge-Lenz vector of

$$\langle \dot{\vec{A}} \rangle = -\frac{3}{2}\vec{F} \times \langle \vec{L} \rangle. \tag{3.37}$$

Taking another derivative of Eq. 3.37 and substituting Eq. 3.32 yields

$$\begin{aligned} \langle \ddot{\vec{A}} \rangle &= -\left(\frac{3}{2}n\right)^2 [\vec{F} \times (\langle \vec{A} \rangle \times \vec{F})] \\ &= -\left(\frac{3}{2}n\right)^2 [\langle \vec{A} \rangle (\vec{F} \cdot \vec{F}) - \vec{F}(\vec{F} \cdot \langle \vec{A} \rangle)]. \end{aligned} \tag{3.38}$$

For the case where the electric field is applied in the plane of the orbit, perpendicular to $\vec{A}$ (*i.e.,* along the semi-minor axis of an elliptical orbit) F defines the z direction and $A_z = 0$ initially, yielding $\langle \ddot{A}_z \rangle = 0$. The remaining components will then follow the equation

$$\langle \ddot{\vec{A}} \rangle = -\left(\frac{3}{2}nF\right)^2 \langle \vec{A} \rangle. \tag{3.39}$$

Similarly, as $\vec{F}$ is perpendicular to $\vec{L}$,

$$\langle \ddot{\vec{L}} \rangle = -\left(\frac{3}{2}nF\right)^2 \langle \vec{L} \rangle, \tag{3.40}$$

which shows that for this case the sum of the Runge-Lenz vector and the angular momentum will rotate about the z axis at half the Stark frequency, $\omega_s = 3nF$, following the Bloch equations

$$\frac{d}{dt}(\vec{L} \pm n\vec{A}) \simeq \frac{\pm\omega_s}{2}(\vec{L} \pm n\vec{A}) \times \hat{z}. \tag{3.41}$$

The physical picture is that of an orbit whose ellipticity varies at $\omega_s/2$ [39]. This statement, that the ellipticity of the orbit can be controllably varied with a uniform,

static electric field of precise duration, is one of the fundamental concepts in the production of the high-ℓ wave packets discussed in this text.

3.1.4 Pulsed Electric Fields

The behavior of atoms in time varying electric fields depends on the characteristic time scales (*e.g.,* rise/fall times and duration) of the fields [44]. Short HCPs, whose duration $T_p \ll T_n$, where T_n is the classical period of an electron orbit, provide an impulsive momentum transfer

$$\Delta p = -\int_{-\infty}^{\infty} F(t)\,\mathrm{d}t, \tag{3.42}$$

resulting in energy transfer, for initial momentum $\vec{p_i}$,

$$\Delta E = \frac{\Delta\vec{p}^{\,2}}{2} + \vec{p_i}\cdot\Delta\vec{p}. \tag{3.43}$$

Depending on whether p_i is oriented with or against the applied impulse, the state will gain or lose energy. Ionization thresholds in the short pulse regime scale as $F_{thresh} \sim n^{-1}$ [44]. Application of HCPs whose amplitude is near the ionization threshold provide a probe of the state's initial momentum. Electrons traveling parallel to the applied field (anti-parallel to the applied impulse) are less likely to ionize than states perpendicular to the field, while electrons traveling anti-parallel to the field are more likely to be ionized.

For longer pulses the ionization threshold approaches the asymptotic limit given in Eq. 3.28, $F_{thresh} \approx 1/9n^4$ [44]. Sudden application of a field step $\vec{F} = F_{step}\,\hat{z}$ at

time t_{step} yields energy transfer

$$\Delta E = z(t_{step})F_{step}. \tag{3.44}$$

Once again, application of fields whose amplitude is set near the ionization threshold act as a probe, this time of an electron's initial spatial coordinate along the field. Electrons located upstream of the nucleus with respect to the field, $z(t_{step}) < 0$, ionize less readily than those located alongside the nucleus, $z = 0$, while electrons located at $z(t_{step}) > 0$ are more likely to ionize [45].

Application of pulsed fields whose rise times are slow with respect to the orbital period are combined with time-of-arrival measurements in the selective field ionization (SFI) technique. As the field is ramped up, F_{thresh} is reached first for the highest n atoms that, upon ionization, produce electrons that are detected by, *e.g.*, a channeltron. Lower n Rydberg states ionize later, when the ramp reaches their (higher) threshold fields. Time-of-arrival measurements distinguish between the fields necessary to ionize each state. Care must be taken in interpretation of the results, however, as the level crossings detailed in Sec. 3.1.2 may be crossed diabatically or adiabatically depending on the slew rate of the SFI field.

3.1.5 Quasi-One Dimensional States

The production of strongly polarized, quasi-1D Rydberg atoms forms the first step in the process of creating most of the high-ℓ wave packets studied in this work (others are created from parent p states). The extreme members of the high-n Stark

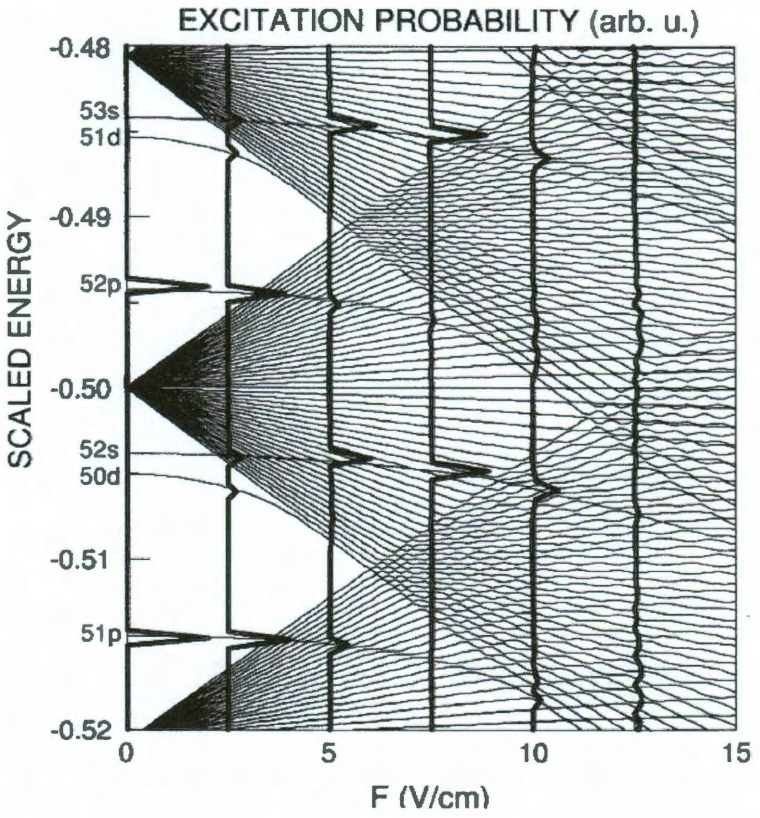

Figure 3.8 : Calculated Stark energy level structure for K($m = 0$) states in the vicinity of $n = 50$ (thin lines). Also included is the probability for photoexcitation from the ground state (thick lines) by a laser with a linewidth $\Delta\omega_L = 10^{-3}/n^2$ for different values of applied DC field. Energies are displayed in scaled units $E_0 = n^2E$ [46].

manifolds have large permanent electric dipole moments and approximate quasi-1D states [46]. These states, however, have low excitation probabilities. In order to create the desired quasi-1D states, the coupling of Stark states is utilized. These $L_0 \sim 0$ states are produced by photoexciting atoms in a weak dc electric field. The calculated Stark energy level structure for $n \sim 50$, is shown in Fig. 3.8. The quantum defects that determine the structure are relatively independent of n, allowing a qualitative

comparison of the Stark energy level structure for $n \sim 300$.

Photoexcitation probabilities calculated for vertically polarized incident radiation exciting potassium from the 4s ground state for several values of applied dc field are superimposed on the figure. Dipole coupling dictates that transitions obey the selection rule $\langle n'\ell'|z|n\ell\rangle \sim \delta_{\ell,\ell\pm1}$, where primed quantum numbers represent final states, the unprimed quantum numbers represent the initial 4s ground state, and $\delta_{i,j}$ is the Kronecker delta. In zero field, then, only the p state is excited. As the electric field is increased, however, Stark states that adiabatically correlate to non-p states (such as the levels that trace to the 50d and 51d states in the figure), take on p state character, in that the Stark state expansion in terms of the zero field states

$$|\alpha\rangle = \sum_{n,\ell} a_{n,\ell}|n,\ell\rangle, \tag{3.45}$$

contains non-zero contributions from the zero field p states, *i.e.*, there exists an $a_{n,\ell=1} \neq 0$. In Eq. 3.45 $|\alpha\rangle$ denotes the Stark state, expanded in terms of the $|n,\ell\rangle$ zero field basis states, with proportionality coefficients $a_{n,\ell}$.

As detailed in Table 3.1, while the s and p states have large quantum defects, the d state quantum defect of potassium is ≈ 0.28. As the electric field is increased the levels that begin as s and p states first encounter states in manifolds of different n. The d levels, due to their small quantum defect, first encounter states in the manifold of the same n. This is seen in Fig. 3.8 as the 50d state approaches the manifold originating at $E_0 = -0.50$ in the zero field limit, while the $n = 50$ manifold encounters the 52s and 52p states first. Coupling is strongest between levels of the

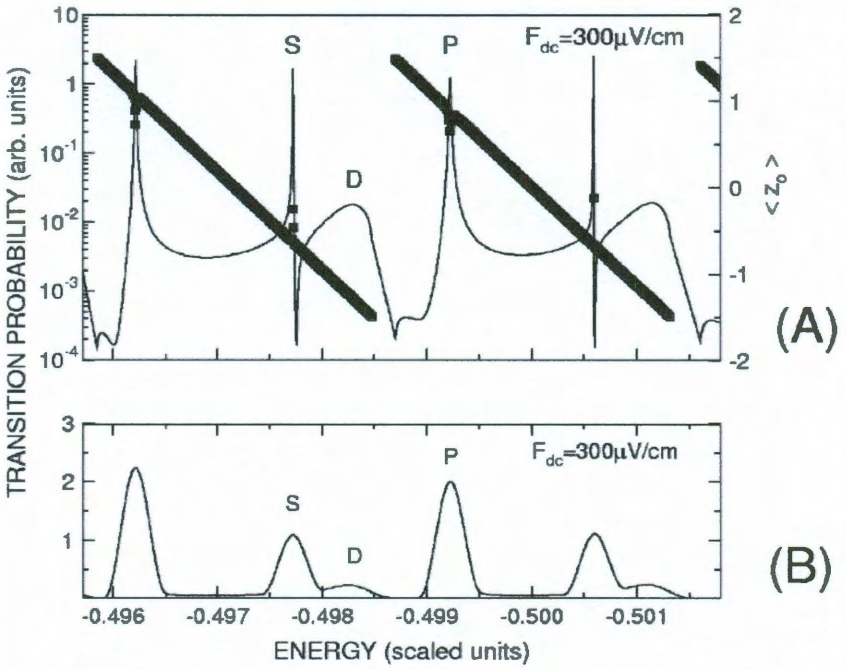

Figure 3.9 : (A) Calculated excitation probability for ultra-narrow linewidth and average scaled position ($\langle z_0 \rangle = -\langle d_0 \rangle$) for $n = 350$, $m = 0$. (B) Calculated excitation probabilities assuming a 10 MHz linewidth. [46].

same n [46], leading to strong mixing of the d state with the extreme red-shifted states of the neighboring manifold as the field is increased to ~ 2.5 V/cm.

Calculations of excitation probability and average scaled electric dipole moment ($d_0 \equiv d/n^2 \in [-1.5, 1.5]$) are shown in Fig. 3.9 and Fig. 3.10 for $n = 350$, $m = 0$ and $n = 306$, $m = 1$ states, respectively. For the $m = 0$ states scaled dipoles are indicated as $d_0^{\mathrm{s}} = 0.25$, $d_0^{\mathrm{p}} = -0.7$, and $d_0^{\mathrm{d}} = 1.25$, showing that Stark shifted d states have large permanent electric dipole moments. Fig. 3.10 shows the same calculation for $m = 1$ states. Here, the Stark shifted d states have scaled moments $d_0^{\mathrm{d}} = 1.3$, slightly larger than those for $m = 0$. For both $m = 0$ and $m = 1$, the Stark shifted d states

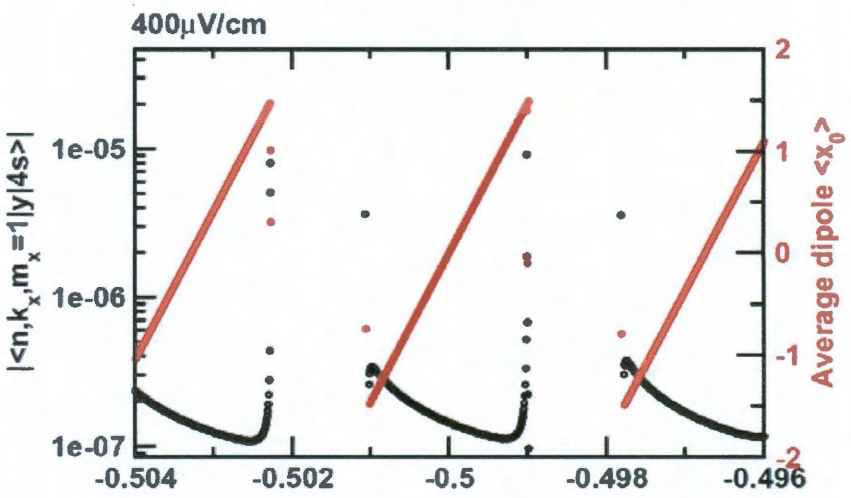

Figure 3.10 : Calculated excitation probability for ultra-narrow linewidth and average dipole moment for $n = 306$, $m = 1$ [47].

excited in an electric field sufficient to cause overlap with the extreme red-shifted Stark states of the neighboring manifold act as quasi-1D states, with high permanent electric dipole moment and sufficiently large excitation probability for the conditions of the present experiment.

Production of quasi-1D states can be verified using HCPs. Recalling Eq. 3.43 it is evident that the application of HCPs of duration $T_p \ll T_n$ parallel to the initial momentum will increase the electron energy, while HCPs applied anti-parallel will tend to decrease the energy, leading to ionization only for kicks $|\Delta p| > 2p_z$. A slow decrease in survival probability is then expected as the magnitude of HCPs directed parallel to the axis of a quasi-1D atom is increased. HCPs directed transverse to the axis of a quasi-1D atom, however, should lead to a narrow distribution of energy

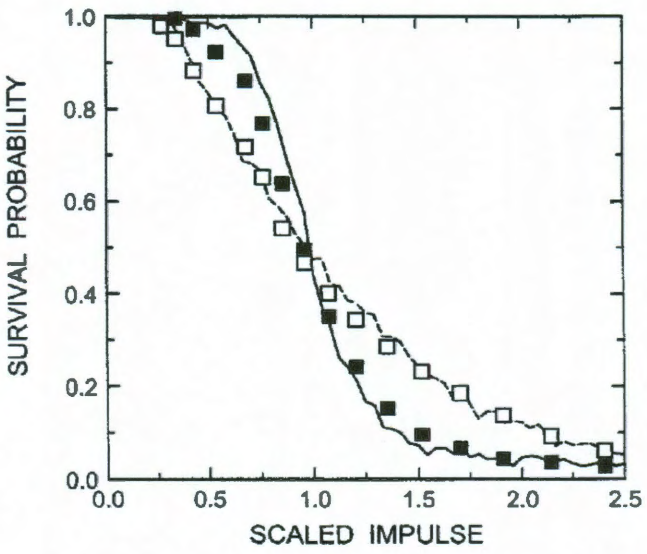

Figure 3.11 : Survival probabilities for quasi-1D atoms in low lying states in the $n = 350$ manifold as a function of scaled momentum. Closed squares represent experimental data for HCPs applied transverse to the axis of the atom, while open squares represent data for HCPs applied along the axis. Lines represent CTMC simulations [48].

transfers, $\Delta E \sim \Delta p^2/2$, resulting in a sharp drop in survival probability beyond a threshold impulse, $|\Delta\vec{p}| = \sqrt{2|E|}$, or in scaled quantities $\Delta\vec{p}_0 = 1$. This behavior has been demonstrated experimentally [48] for states near $n = 350$, and is illustrated in Fig. 3.11. In the present work, at $n = 306$, quasi-1D atoms are photoexcited in a weak ~ 400 μV/cm dc field. Field steps of -5 mV/cm are then applied transverse to the quasi-1D axis for $T_F = T_s/2 = \pi/\omega_s$ to produce localized circular states.

3.1.6 Lifetimes

Although Rydberg electrons are loosely bound, the radiative lifetimes of high-n states are quite large. The two main contributors to a given state's lifetime come from the amount of overlap between the wavefunctions of the initial and final states, D_{ij}, and the energy difference, $\omega_{ij} = E_j - E_i$, between the states. The rate of spontaneous decay of an excited state is given by the Einstein A coefficient [49], which scales as

$$A_{ij} \sim D_{ij}^2 \omega_{ij}^3. \tag{3.46}$$

The radiative lifetime of a state is given by the inverse of the sums of all possible transitions out of that state

$$\tau_i^{rad} = \left[\sum_j A_{ij}\right]^{-1}. \tag{3.47}$$

The ω^3 scaling suggests that transitions with the highest energy difference (such as from the initial high-n state to the lowest state with $\Delta\ell = 1$) dominate the lifetimes. The overlap of wavefunctions between these states, however, is quite small. For a high-n, low-ℓ state the overlap with very low-n states leads to radiative lifetimes that scale as n^3 [35]. For high-ℓ states, however, the highest transition rates are to neighboring high-n states, again with $\Delta\ell = 1$. For the extreme circular states these are transitions to adjacent circular states, $|n, \ell = n-1\rangle \rightarrow |n-1, \ell = n-2\rangle$. The frequency of this transition contributes an n^{-9} scaling to A, while the wavefunction overlap is relatively large, scaling as n^2. Together these result in radiative lifetimes for high-n, high-ℓ states

$$\tau_{\text{high } \ell} \sim n^5, \tag{3.48}$$

which at $n \sim 300$ is approximately a 90,000 times increase in lifetime.

Effectively, however, the lifetimes of high-n states are reduced by interaction with background blackbody radiation. Estimates of blackbody corrected lifetimes for moderately high-n suggest

$$\tau = \tau_0 n^{\alpha}, \tag{3.49}$$

where τ_0 is the zero Kelvin lifetime reference and α is a calculated decay rate scaling [50,51]. For K(np) states, $\tau_0 = 6.78$ ns and $\alpha = 2.78$ [51], leading to an estimated blackbody corrected lifetime for $n = 305$ of $\tau = 55$ ms. The apparatus used in the current experiment is not capable of measuring lifetimes of this magnitude. Further, blackbody corrected lifetimes for high-n states are ℓ dependent and are expected to lead to shorter lifetimes for high-ℓ states than the estimate in Eq. 3.49, while suppression of blackbody absorption and inhibited spontaneous emission are expected in between parallel plates such as those that make up the interaction region [52–54]. The magnitudes estimated here suggest lifetime effects will not contribute appreciably during the microsecond time scales of the present study. The blackbody energy density of resonant 4s→300p radiation is also quite low. Using Planck's law at room temperature, the blackbody spectral energy density at 285 nm is $\sim 10^{-64}$ J/m^3/m, while for 770 nm, resonant with the 4s→4p transition, the density is $\sim 10^{-20}$ J/m^3/m. The production of both low and high ℓ states presented here, however, could form the basis for future studies of these effects.

3.1.7 Collisions

Collisions of Rydberg atoms with neutral perturbers are often described by considering the interaction between the neutral perturber, B, and either the Rydberg core ion, A^+, or electron, e^-, to be short ranged with respect to the A^+– e^- separation. The collision is then modeled as that between the perturber and electron in the presence of the Coulomb field. The A^+– B collision is treated similarly, though it is often neglected due to the large mass difference between e^- and A^+ [55, 56]. This constitutes the binary encounter theory, where A^+– B and e^-– B collisions are treated independently [57].

In the free electron model, the e^-– B interaction is treated as the scattering of a free electron during the collision. The initial e^- velocity distribution is determined by the electron's initial state, before the collision, and the final electron state is considered once again in the presence of A^+. In effect, the A^+– e^- interaction is "turned off" during the collision. Treating the free e^-– B collision as a brief semi-classical momentum transfer constitutes the impulse approximation [36, 58].

The validity of these approximations is based on the A^+– e^- separation, the e^-– B scattering length, and the relative velocities. For $n = 306$, the orbital radius, as given in Tab. 1.1, is roughly 5 μm. The low energy e^-– CO_2 scattering length, meanwhile, is ~ 4 Å [59]. Collisions for which $v_{e^-} \ll v_B$ and $v_{e^-} \gg v_B$ can be treated impulsively [36]. This can be understood by considering the duration of the collision process with respect to the orbital period of the electron. When $v_{e^-} \simeq v_B$, however,

the A^+– B interaction has more of an effect on the overall collision process, and the impulse approximation becomes less accurate.

Calculation of the relative Rydberg–perturber speed follows Ref. [60]. Though the parent K atoms are in a beam with velocity distribution (see Eq. 2.2) $\sim v^3$, as discussed in Sec. 2.1 the Rydberg atoms follow a Maxwell-Boltzmann speed distribution $\sim v^2$. An ambient background gas of perturbers would also follow a similar Maxwellian distribution. The speed distribution of species i is then given by

$$f_i(v_i) = 4\pi\left(\frac{m_i}{2\pi k_B T_i}\right)^{\frac{3}{2}} v_i^2 e^{-\frac{m_i v_i^2}{2k_B T_i}}, \tag{3.50}$$

where m_i, T_i, and v_i are the mass, temperature, and velocity of the species, and k_B is Boltzmann's constant. Assuming for a moment that each species has only one speed, but that they are in arbitrary directions with respect to each other, the relative speed is

$$v_r = \sqrt{v_A^2 + v_B^2 - 2v_A v_B \cos\theta}, \tag{3.51}$$

where A and B denote the Rydberg atom and perturber, respectively. Averaging over relative angles yields

$$\begin{aligned}\langle v_r \rangle &= \frac{\int_0^{2\pi}\int_0^{\pi} v_r \sin\theta \mathrm{d}\theta\mathrm{d}\phi}{\int_0^{2\pi}\int_0^{\pi} \sin\theta \mathrm{d}\theta\mathrm{d}\phi} = \frac{1}{2}\int_0^{\pi} \sqrt{v_A^2 + v_B^2 - 2v_A v_B \cos\theta}\sin\theta \mathrm{d}\theta \\ &= \frac{1}{6v_A v_B}\left[(v_A + v_B)^3 - |v_A - v_B|^3\right] = \begin{cases} v_A + \frac{v_B^2}{3v_A} & \text{for} \quad v_A > v_B, \\ v_B + \frac{v_A^2}{3v_B} & \text{for} \quad v_B > v_A. \end{cases}\end{aligned} \tag{3.52}$$

Easing the approximation that the species have single speeds, an average is taken

over the distributions

$$\begin{aligned}\langle v_r \rangle &= \int_0^\infty \int_0^\infty v_r f_B(v_B) f_A(v_A)\, \mathrm{d}v_B\, \mathrm{d}v_A \\ &= \int_0^\infty \left[\int_0^{v_A} \left(v_A + \frac{v_B^2}{3v_A}\right) f_B(v_B)\, \mathrm{d}v_B \right. \\ &\qquad \left. + \int_{v_A}^\infty \left(v_B + \frac{v_A^2}{3v_B}\right) f_B(v_B)\, \mathrm{d}v_B \right] f_A(v_A)\, \mathrm{d}v_A. \end{aligned} \tag{3.53}$$

Solving numerically for room temperature background CO_2 and K(n) Rydberg atoms originating from a $T = 600$ K oven, as used in the current studies, yields an average relative velocity $\langle v_r \rangle = 685$ m/s. Recall that the average Rydberg atom velocity, given by Eq. 2.4, is $\overline{v}_{\mathrm{Ryd}} = 570$ m/s

Average Rydberg electron velocities are given by (see Sec. B.2)

$$v_{e^-} = \frac{1}{n} \text{ a.u.} = \frac{2.19 \times 10^6}{306} \text{ m/s} = 7150 \text{ m/s}. \tag{3.54}$$

This velocity is valid throughout a classical circular orbit. The classical speed during an elliptical orbit, however, depends on the location around the orbit, θ [38]

$$\begin{aligned} v_\theta(\theta) = r\dot{\theta} &= \frac{L}{r} = \frac{1 + \varepsilon \cos\theta}{nL_0} \\ &= \frac{1 + \varepsilon \cos\theta}{n\sqrt{1-\varepsilon^2}} = \begin{cases} \dfrac{1+\varepsilon}{n\sqrt{1-\varepsilon^2}} & \text{for} \quad \theta = 0, \\ \dfrac{1-\varepsilon}{n\sqrt{1-\varepsilon^2}} & \text{for} \quad \theta = \pi, \end{cases} \end{aligned} \tag{3.55}$$

where Eq. 3.2 and the definitions of scaled angular momentum and ellipticity have been used. For a state such as $|n = 300, \ell = 20\rangle$, $\varepsilon = 0.9978$, leading to a spread in velocity between $\sim 30/n = 214500$ m/s at the pericenter to $\sim 0.03/n = 214$ m/s at the apocenter (three orders of magnitude difference). Though $v_{e^-}/v_B \simeq 10$ here, for

which the impulsive approximation is still good, studies of the $v_{e^-} \simeq v_B$ regime would benefit from the narrow velocity range provided by the high-n, high-ℓ wave packets studied here.

3.2 Simulations

3.2.1 Classical Trajectory Monte Carlo Simulations

To follow the time evolution of a wave packet in quantum mechanics requires evaluation of time dependent complex wavefunctions or probability flows, $|\langle\vec{r}|\psi(t)\rangle|^2$. For even moderately high n values, the probability flow can be approximated by a classical probability density in phase space, $f(\vec{r},\vec{p},t)$. Evolution of $f(\vec{r},\vec{p},t)$ is determined by the classical Liouville equation [24]

$$\frac{\partial f(\vec{r},\vec{p},t)}{\partial t} = \{H(t), f(\vec{r},\vec{p},t)\}, \tag{3.56}$$

where $H(t)$ is the state Hamiltonian and $\{,\}$ denotes the Poisson bracket. Replacing $f(\vec{r},\vec{p},t)$ by an ensemble of trajectories whose initial conditions are weighted by $f(\vec{r},\vec{p},t)$ allows evaluation of the approximate time evolution of the system by propagation of the trajectories using Hamilton's equations. Following these classical trajectories, which originate from an initial ensemble sampled by a Monte Carlo technique, comprises the classical trajectory Monte Carlo (CTMC) method [61]. The details of the models used to approximate the quantum wave packet using an ensemble of classical trajectories can be found elsewhere [24, 62, 63].

The CTMC method has been shown, particularly by previous experiments in this laboratory, to very accurately model the free evolution of high-n Rydberg wave packets for times less than the quantum revival time, T_{rev}, and the evolution of wave packets under the influence of external driving for extended periods.

3.2.2 CTMCs with Energy Discretization

Modeling the free evolution of wave packets beyond T_{rev} requires modification of the CTMC simulations. As stated in Ch. 1, one of the major differences in the classical and quantum descriptions of electron orbits is the nature of the allowable energy distributions. Continuous energy levels are allowed by the classical probability density distribution used to approximate the wave packet. Forcing discretization of these levels produces a semi-classical approximation method which is able to predict the quantum revival behavior expected for high n wave packets.

The discretization method employed here is chosen to match classical frequencies to quantum energy differences. The dominant contributions to the dynamic quantities, quantum mechanically, come from the differences between neighboring energy levels. The second order Taylor expansion of this energy difference yields

$$\Omega_{n,n'=n+1} = \frac{1}{2n^2} - \frac{1}{2(n+1)^2} \approx \frac{1}{n^3} - \frac{3}{2n^4}. \tag{3.57}$$

Classical frequencies, $\Omega_{cl} = 1/n_{cl}^3$, derive from the principal classical action, $n_{cl} = 1/\sqrt{-2E}$, for energy E. Forcing $n_{cl} \to n$, for integer n, yields frequencies which only

agree to first order. Choosing a half integer classical action, however, yields

$$\Omega_c = \frac{1}{(n+1/2)^3} \approx \frac{1}{n^3} - \frac{3}{2n^4}, \tag{3.58}$$

which matches Eq. 3.57 to second order (the order of the revivals, *i.e.*, to terms including n^{-4}). Experimental observations match simulations with half-integer classical action more closely than those with integer n_{cl}.

Upon discretization the phase space coordinates of each simulated trajectory are renormalized (see Sec. B.2 for scaling equations)

$$\begin{aligned} x_i' &= \left(\frac{\lfloor n_{cl} \rfloor + 1/2}{n_{cl}}\right)^2 x_i, \\ p_i' &= \left(\frac{n_{cl}}{\lfloor n_{cl} \rfloor + 1/2}\right) p_i, \end{aligned} \tag{3.59}$$

where unprimed/primed x_i and p_i represent the spatial and momentum coordinates, respectively, before/after discretization. Each trajectory is then allowed to evolve freely. This method is restricted to the case of free evolution, since in the presence of time dependent external fields the levels do not remain quantized, and therefore fail to approximate the quantum evolution. Forcing the same discretization presented in this section even in the presence of external fields also fails to approximate the evolution, as it fails to allow for quasi-discrete, line-broadened levels, which will be discussed in the next section. Discretized CTMC simulations, however, provide a valuable approximation when considering the effects of different high-ℓ wave packet initialization schemes. Cases of strong external driving, where the discrete nature of the energy levels is expected to be smeared out, and cases of small numbers of

impulsive momentum transfers with little random energy diffusion, to be discussed in Ch. 5, are also described well by discretized CTMC simulations.

3.2.3 Quantized CTMCs

The Stark shifts experienced by Rydberg atoms in the presence of external electric fields lead to a broadening of levels

$$E_{nk} = -\frac{1}{2(n+1/2)^2} + \frac{3}{2}nkF_{ext}, \tag{3.60}$$

due to the k distribution of the state. High angular momentum states originating from parent p states, to be discussed in Ch. 4, have a near uniform spread in $k \in [-n, n]$, while states originating from parent quasi-1D states also have a finite spread in k, leading to non-negligible, amplitude dependent line-broadening. The sudden switching of an external electric field, as experienced in the presence of high frequency noise, leads to jumps between n levels. This effect can be incorporated into the simulations by assuming a random walk between neighboring, quasi-discrete n levels, whose jump rate is determined by measuring the diffusion of energy levels in a discretized CTMC simulation which includes the switching field. Details can be found in Ref. [64].

The effect of external electrical noise on the wave packet is then simulated by *free evolution* of line-broadened states subject to a random walk of energy diffusion. This method is termed the *quantized* classical trajectory Monte Carlo (QCTMC) method, and, as shown in Ch. 6, the results of this method agree extremely well with both fully quantum calculations and experimental observations, while the results of

discretized CTMC simulations in the presence of the noise field do not. The separate contributions of line-broadening and energy diffusion are studied in Ch. 6 by varying, independently, the amplitude and characteristic frequency of various noise signals.

Chapter 4

Production and Characterization of High-ℓ Electron Wave Packets

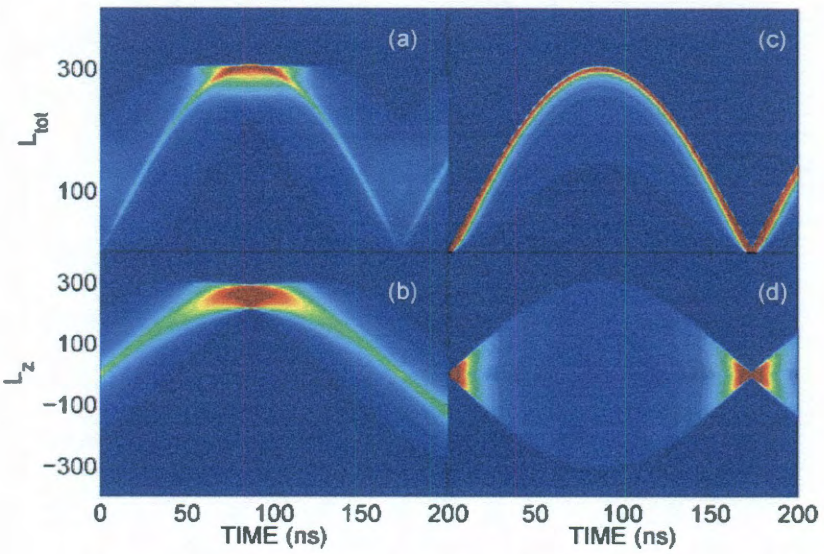

Figure 4.1 : Classical trajectory Monte Carlo simulations of the distributions of the total and z component of angular momentum for (a), (b) parent quasi-1D states oriented in the x direction and (c), (d) parent p states in the presence of a 5 mV/cm pump field applied in the $-y$ direction.

Whether starting with parent quasi-1D states or p states, the Stark precession described in Sec. 3.1.3 causes evolution of the total angular momentum of Rydberg electron wave packets as demonstrated in Fig. 4.1. The precise nature of the resulting energy and angular momentum distributions, however, depends on not just the total

area under the pump pulse curve, but also on the amplitude and rise/fall times of the pump pulse. Sec. 4.1 details the dependence of the resulting wave packet on the details of its production. Experimental characterization of wave packets is accomplished through Fourier analysis, as described in Sec. 4.2. Both population and phase information is obtained, with single n resolution.

4.1 Production

Experimental realization of high-ℓ Rydberg wave packets is accomplished starting with both parent quasi-1D states and parent p states. For both cases a laser, linearly polarized along the y direction, traveling in the $-z$ direction,[1] intersects an atomic beam traveling in the $-x$ direction. Due to the ground state hyperfine splitting of K, Rydberg excitation spectra constitute two interleaved series originating from the thermally populated $F = 1$ and $F = 2$ ground states, separated by ~ 460 MHz. As shown in Fig. 4.2, in the vicinity of $n \sim 305$ the energy difference of the hyperfine ground states matches the energy difference between next-nearest-neighbor Rydberg levels, *i.e.*, $E(n = 4, F = 1 \rightarrow n = 305) \approx E(n = 4, F = 2 \rightarrow n = 307)$, leading to simultaneous excitation of these two states. The majority of the experiments presented here occur at these "accidental resonances" due to the increased count rate their simultaneous excitation provides. Excitation from single hyperfine ground states

[1]Ch. 3 used the electric field direction to determine the z axis. In this chapter the apparatus determines the coordinate system.

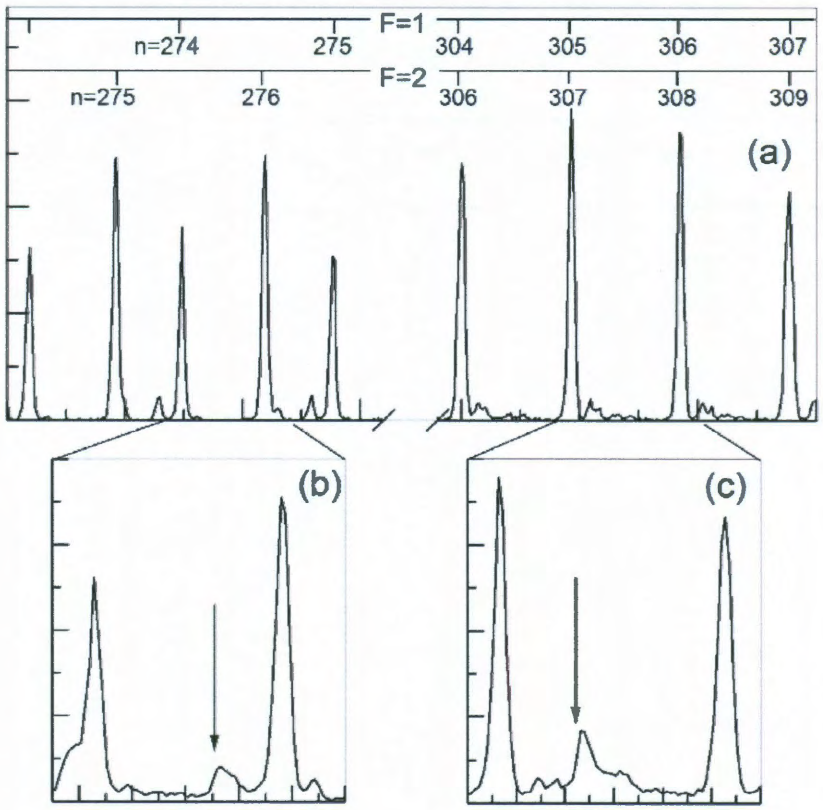

Figure 4.2 : (a) Interleaved Rydberg spectra excited in zero electric field. Large amplitude peaks originate from the $F = 1$ and $F = 2$ hyperfine ground states of the majority ^{39}K isotope, while small background peaks originate from the minority ^{41}K isotope. (b),(c) Excitation spectra in the presence of an offset field. Quasi-1D states are obtained by exciting at the frequencies indicated by the arrows.

is also accomplished in portions of the present work by tuning the laser to resonance with $n \sim 275$ and $n \sim 315$, where the individual states can be resolved.

Quasi-1D excitation to $n \sim 305$ occurs in the presence of a 400 μV/cm (620 μV/cm for $n \sim 275$) offset electric field in the $-x$ direction, resulting in quasi-1D states oriented in the x direction. The Doppler width of the excitation beam with respect to the atomic beam ($\sim$ 10 MHz) leads to the production of $\sim$ 35 low lying, red-shifted

Stark states centered around $\bar{k} \approx 260$, resulting in a scaled electric dipole moment $d_0 = -1.25$. The offset field is then turned off slowly to prevent inhomogeneous Stark line broadening. Parent p states are excited in zero field. The excitation laser is polarized along the y axis, yielding a well defined initial m_y, however, the magnetic substates are mixed after excitation due to small stray fields in the interaction region. At the start of the pump pulse the p states are described by an ensemble of fully mixed magnetic substates, whose orientations are uniformly distributed on the unit sphere, with L_y and A_y uniformly distributed in $[-L, L]$ and $[-1, 1]$, respectively.

Approximately 500 ns after excitation, a pump field, $\vec{F} = -F_{pump}\,\hat{y}$, is applied from the top electrode providing the Stark precession necessary for the production of high-ℓ states. The total angular momentum of both initial states reaches a maximum at time $t = \pi/\omega_s$, at which time the pump field is terminated. L_z for the quasi-1D state remains narrowly peaked with $L_x \approx L_z \approx 0$, resulting in well defined circular motion in the xy plane. For the p state L_z and L_x are uniformly distributed, leading to the production of states with components orbiting in many different planes sharing the y axis. A simulated spatial distribution for a quasi-1D parent state just prior to termination of the pump pulse is shown in Fig. 4.3, demonstrating that the wave packet is nearly uniformly distributed in azimuth, ϕ.

Termination of the pump pulse leads to an energy shift, derived from the Stark Hamiltonian (Eq. 3.12),

$$\frac{dH_{Stark}}{dt} = y(t)\frac{dF_{pump}(t)}{dt}. \tag{4.1}$$

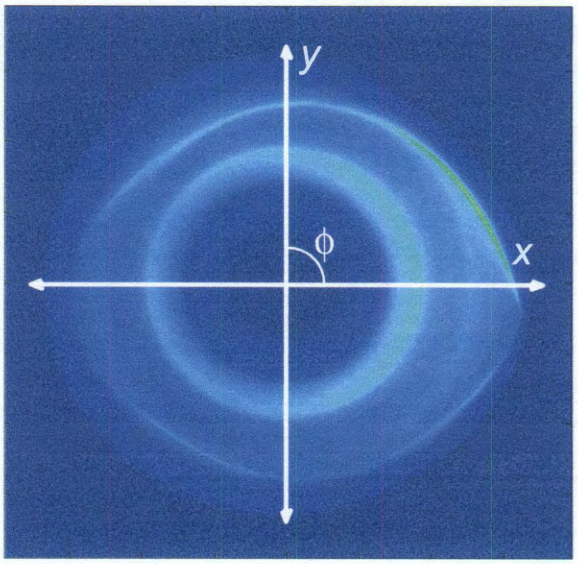

Figure 4.3 : Circular wave packet prior to pump termination.

For sudden termination of the pump pulse, $t_{fall} \ll T_n$, the final energy change for each component depends on azimuth,

$$\Delta E = y(t_{off}) F_{pump} = n_i^2 \sin\phi F_{pump}, \tag{4.2}$$

for initial n_i. Note that there is no energy exchange at the start of the pump pulse, as the initial quasi-1D state is oriented in the x direction, implying $y(t_{rise}) \approx 0$. Components at $\phi = \pm\pi/2$ receive the largest energy transfer, leading to a total spread in energy $\Delta E = 2n_i^2 F_{pump}$. Fig. 4.4 shows a simulated azimuthal distribution of n levels immediately following termination of a 5 mV/cm pump pulse with $t_{fall} = 0.3$ ns. Strong correlation exists between n and ϕ. Fig. 4.5 shows the effect of using a smaller

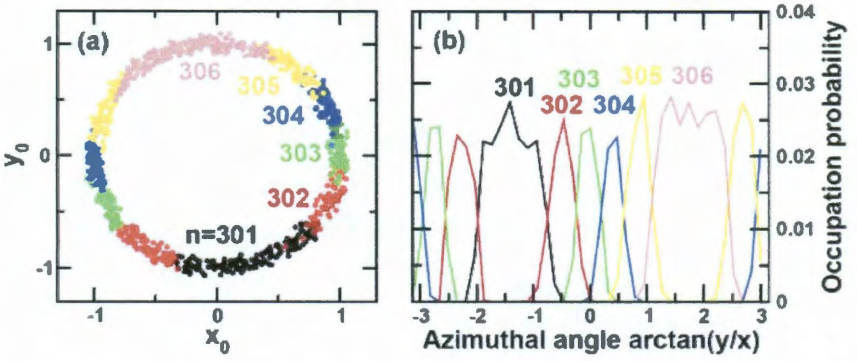

Figure 4.4 : Simulated azimuthal n distribution generated from an extreme parabolic state ($n_i = 304, k = 303$) after sudden termination of a 5 mV/cm pump pulse [47].

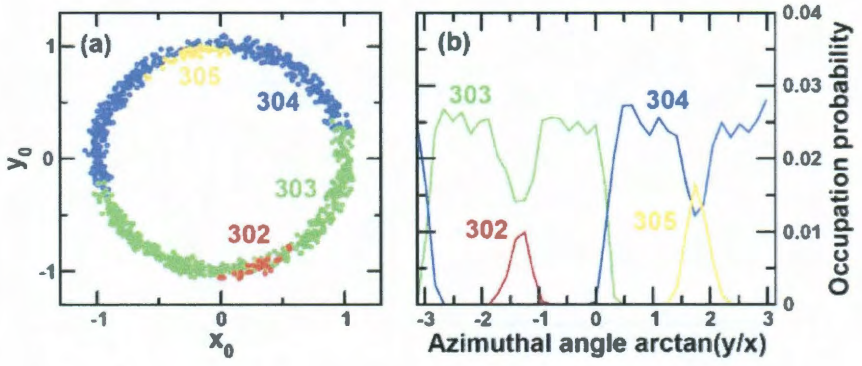

Figure 4.5 : Simulated azimuthal n distribution generated from an extreme parabolic state ($n_i = 304, k = 303$) after sudden termination of a 2 mV/cm pump pulse [47].

pump pulse. By selecting an appropriate value for F_{pump}, the total energy spread can be controlled. After pump termination, each wave packet component will orbit the nucleus at its own characteristic rate, $\omega_n = n^{-3}$, coming into and going out of phase with the other components as they freely evolve.

Application of a probe field step, as described in Sec. 3.1.4, provides a measure of the average spatial components along the probe direction. Fig. 4.6 shows experimental

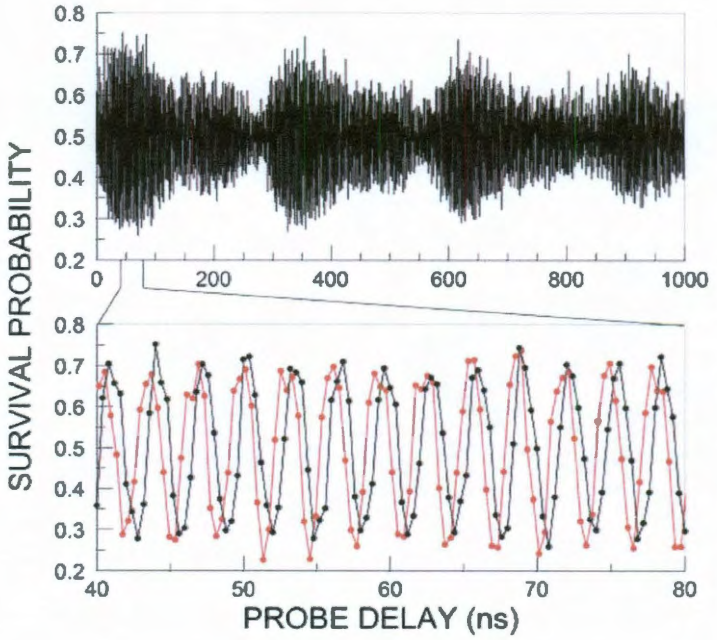

Figure 4.6 : Survival probability vs probe delay for a 6 ns duration probe pulse applied at 0.5 ns intervals along the y (black) and x (red) directions to circular states produced from parent $n = 274$ (excited from the $F = 1$ ground state), quasi-1D states subject to a 5 mV/cm, 95 ns duration pump pulse with 0.3 ns rise/fall times.

survival probabilities measured while probing a circular wave packet produced from a parent $n = 274$, quasi-1D state. An initial buildup can be seen, where the wave packet components all initially come into phase with each other. They then continue their free evolution and dephase, as demonstrated by the reduction in survival probability amplitude, only to subsequently rephase at the quantum revival times. Probing in both the x and y directions shows oscillatory behavior, 90° out of phase, as expected for circular motion. Accumulation of the data presented in Fig. 4.6 required 18 hours of data collection. Rather than repeating all full length measurements probing in both the x and y directions, the data sets that follow were probed in full along

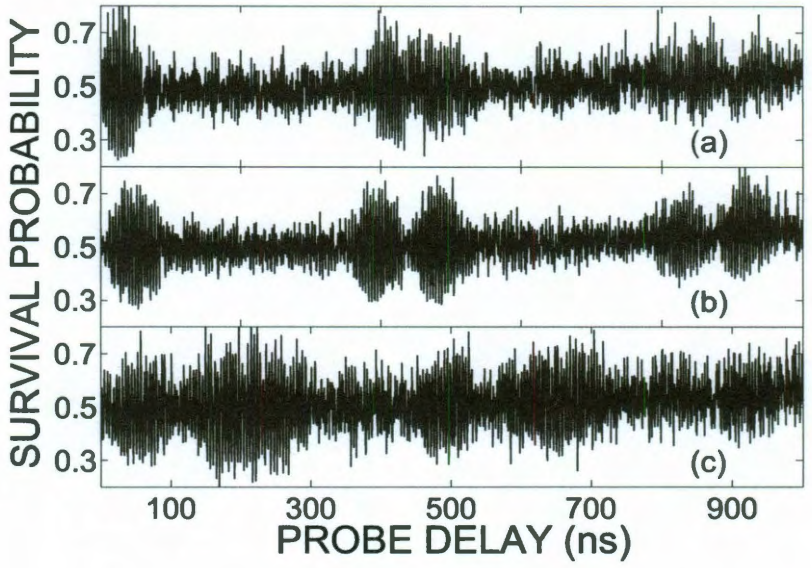

Figure 4.7 : Survival probability vs probe delay for a 6 ns duration, 120 mV/cm probe pulse applied at 0.5 ns intervals to circular states produced from parent quasi-1D states subject to (a) 10 mV/cm, 43 ns duration, (b) 5 mV/cm, 85 ns duration, and (c) 2 mV/cm, 170 ns duration pump pulses with 0.3 ns rise/fall times.

the y direction, with short windows of data probed in the x direction (not shown) periodically taken to ensure circular motion. Probing along the z direction shows no oscillatory behavior. The same is true probing in both the x and z directions for states created from parent p states.

The dependence of the waveform shape on the pump amplitude is demonstrated in Fig. 4.7. Wave packets with larger numbers of contributing frequency components will show shorter durations of localization. The survival probability signals for 10, 5, and 2 mV/cm pump amplitudes show increased localization durations in the survival probability signals with decreasing pump amplitude. Time-domain analysis,

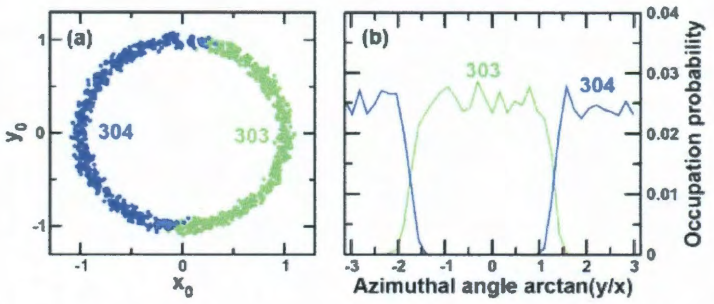

Figure 4.8 : Simulated azimuthal n distribution generated from an extreme parabolic state ($n_i = 304, k = 303$) after slow termination of a 5 mV/cm pump pulse [47].

discussed in the next section, confirms this relationship between energy spread and pump amplitude.

The energy spread produced by the pump pulse can also be calculated for finite fall times. Assuming the ellipticity and orientation of the orbits change little during the course of pump termination (an approximation good for $t_{fall} \lesssim T_n$) Eq. 4.1 can be integrated over a fixed circular orbit, $y(t) = n_i^2 \sin(n_i^{-3} t)$. Linear falls, $F \propto 1 - (t - t_{off})/t_{fall}$, produce energy spreads [65]

$$\Delta E_{\text{linear}} = 2n_i^2 F_{pump} \left| \frac{\sin(\pi t_{fall}/T_{n_i})}{\pi t_{fall}/T_{n_i}} \right|, \tag{4.3}$$

while sine-like falls, $F \propto 1 - \sin[\pi(t - t_{off})/t_{fall})]$, produce energy spreads

$$\Delta E_{\text{sine}} = 2n_i^2 F_{pump} \left| \frac{\cos(\pi t_{fall}/T_{n_i})}{1 - (t_{fall}/T_{n_i})^2} \right|. \tag{4.4}$$

Fig. 4.8 shows the distribution produced for the same conditions as Fig. 4.4, but with a sine-like fall time of 6.6 ns. Fig. 4.9 shows experimental results under similar conditions. Again, the width of the localization envelope in survival probability signals

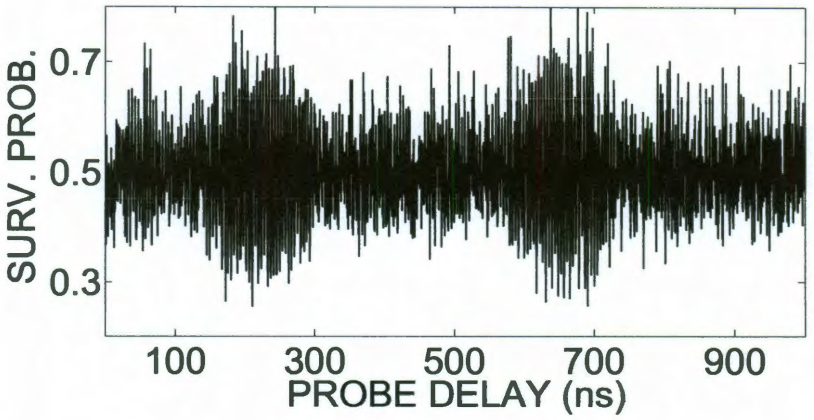

Figure 4.9 : Survival probability vs probe delay after slow termination of a 5 mV/cm pump pulse, with fall time $t_{fall} = 6$ ns applied to a parent $n \sim 305$ quasi-1D state.

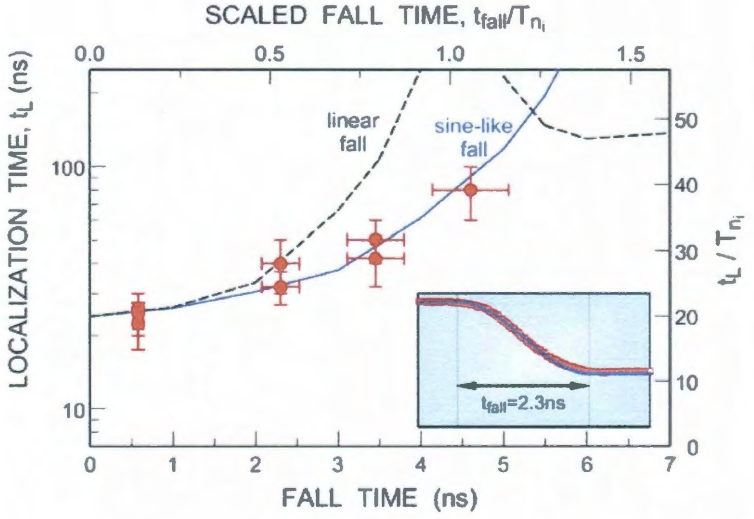

Figure 4.10 : Classical localization times as a function of fall time for linear (dashed) and sine-like (solid) fall profiles. Dots represent experimental results. An experimental pulse profile is shown in the inset. Localization times are scaled to 10 mV/cm pump conditions [65].

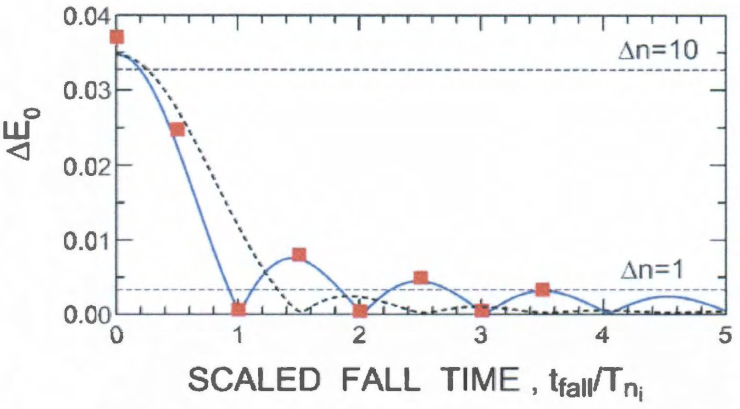

Figure 4.11 : Calculated energy spread as a function of fall time for linear (dashed) and sine-like (solid) profiles for pumps applied to pure 1D states. Dots represent calculations for sine-like profiles applied to a quasi-1D state [65].

is indicative of a smaller number of contributing frequency components as compared to the sudden pump termination signal. Fig. 4.10 compares experimentally inferred maximum localization times with those predicted for linear and sine-like pump fall off. Calculated energy spreads are illustrated in Fig. 4.11 as a function of fall time for linear and sine-like profiles.

4.2 Fourier Analysis

Fourier analysis is performed on the time-varying survival probability signals in order to more quantitatively characterize the effects of the pump pulse shape on the resultant wave packets. Parent quasi-1D states will be discussed unless otherwise noted. After termination of the pump pulse, the wave packet is composed of a superposition

of high angular momentum states ($n \sim \ell \sim m$)

$$|\Psi(t)\rangle = \sum_{n}{}' \sum_{\ell,m}{}' |a_{n,\ell,m}| e^{-i\Phi_{n,\ell,m}(t)} |\psi_{n,\ell,m}\rangle, \tag{4.5}$$

where $|a_{n,\ell,m}|$ is the modulus and $\Phi_{n,\ell,m}$ is the phase of the expansion coefficients, and primed notation indicates that the sum over n, ℓ, and m is restricted to a narrow range of n (determined by F_{pump}). Switch off of the pump is taken as $t = 0$ for the subsequent field free evolution. The wave packet is initially fairly uniformly distributed in ϕ. Localization in azimuth requires the coherent superposition of several m states with properly aligned phases, $\Phi_{n,\ell,m}$. If for example, $\Phi_{n,\ell,m} \simeq m\phi_0$, the wave packet is localized at ϕ_0 with a width determined by the range of m included in the superposition [66]. After switching off the pump field, $\Phi_{n,\ell,m}(t)$ evolves as $\Phi_{n,\ell,m}(0) - t/(2n^2)$.

The rotating wave packet can be monitored by observing the expectation value of the spatial coordinates [67],

$$\begin{aligned}\langle y(t)\rangle &= \sum_{n,\ell,m}{}' \sum_{n',\ell',m'}{}' |a_{n,\ell,m} a_{n',\ell',m'}| e^{-i(\Phi_{n,\ell,m}(t) - \Phi_{n',\ell',m'}(t))} \langle \psi_{n',\ell',m'}|y|\psi_{n,\ell,m}\rangle \\ &\simeq \sum_{n,\ell,m}{}' 2D_{n,\ell,m} \sin\left(\Delta\Phi_{n,\ell,m}(t)\right) \equiv \sum_{n,\ell,m}{}' \langle y(t)\rangle_{n,\ell,m}\,,\end{aligned} \tag{4.6}$$

where $D_{n,\ell,m} = |\langle \psi_{n,\ell,m}|\rho y|\psi_{n,\ell,m}\rangle|$ is the modulus of the dipole expectation value for a density matrix with element $\langle \psi_{n',\ell',m'}|\rho|\psi_{n,\ell,m}\rangle = a_{n,\ell,m} a^*_{n',\ell',m'}$ and $\Delta\Phi_{n,\ell,m}(t) = \Phi_{n+1,\ell+1,m+1}(t) - \Phi_{n,\ell,m}(t)$. Here, $D_{n,\ell,m}$ can be approximated as

$$D_{n,\ell,m} \simeq |a_{n,\ell,m} a_{n+1,\ell+1,m+1} \langle \psi_{n+1,\ell+1,m+1}|y|\psi_{n,\ell,m}\rangle|\,, \tag{4.7}$$

because, for circular states the dipole matrix elements effectively couple only states satisfying the condition $n' = n \pm 1$, $\ell' = \ell \pm 1$, $m' = m \pm 1$. Each component $\langle y(t) \rangle_{n,\ell,m}$ oscillates harmonically with amplitude $2D_{n,\ell,m}$, and a time-dependent phase

$$\Delta\Phi_{n,\ell,m}(t) = \Delta\Phi_{n,\ell,m}(0) + \Omega_n t\,, \tag{4.8}$$

where $\Omega_n = 1/(2n^2) - 1/(2(n+1)^2)$ closely matches the classical frequency ($\Omega_n \simeq n^{-3} = \omega_n$) for large n. The entire wave packet behaves as an ensemble of "classical" electrons in different n, ℓ, m states. The localization condition $\Phi_{n,\ell,m} = m\phi_0$ is equivalent to the condition $\Delta\Phi_{n,\ell,m} = \phi_0$ and corresponds to the situation where all the components in Eq. (4.6) within a single n shell remain in phase at all times. If this condition is satisfied, $\langle y(t) \rangle$ displays strong harmonic oscillations that can be probed experimentally. However, each n-component evolves with a different angular frequency leading to dephasing.

Given Eq. (4.6), information on both the phase and modulus can be extracted from a Fourier transform of $\langle y(t) \rangle$

$$c_n = \frac{1}{T}\int_0^T \langle y(t) \rangle e^{-i\Omega_n t} dt \simeq {\sum_{\ell,m}}' D_{n,\ell,m} e^{-i\Delta\Phi_{n,\ell,m}(0) + i\pi/2}\,, \tag{4.9}$$

provided that T is sufficient to resolve individual n levels, i.e., $\gg 2\pi/(\Omega_n - \Omega_{n+1})$. When (as here) the components exhibit angular localization, *i.e.*, the $\Delta\Phi_{n,\ell,m}(0)$ are nearly independent of ℓ and m, the complex expansion coefficients can be factorized as

$$c_n \simeq e^{-i\Delta\Phi_{n,\ell,m}(0) + i\pi/2} {\sum_{\ell,m}}' D_{n,\ell,m}\,. \tag{4.10}$$

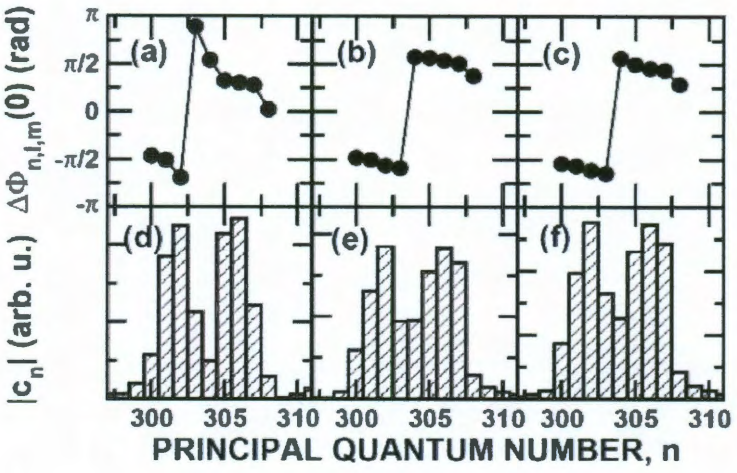

Figure 4.12 : Comparison of Fourier transforms for (a),(d) experimental survival probabilities, (b),(e) simulated survival probabilities, and (c),(f) simulated spatial averages produced by a 5 mV/cm pump pulse [67].

Since the dipole matrix elements for circular states are nearly independent of ℓ and m, $|\langle\psi_{n+1,\ell+1,m+1}|y|\psi_{n,\ell,m}\rangle| \simeq n^2/2$, and the sum of off-diagonal elements of the density matrix can be determined as

$$\left|\sum_{\ell,m}{}'\langle\psi_{n+1,\ell+1,m+1}|\rho|\psi_{n,\ell,m}\rangle\right| = \frac{2}{n^2}\sum_{\ell,m}{}' D_{n,\ell,m}\,. \tag{4.11}$$

This quantity approximates, for a fully coherent ensemble, the geometric mean of the occupation probabilities for the n and $n+1$ levels. Alternately, it can be interpreted as the probability for a "classical" electron to evolve with angular frequency $\omega_n = n^{-3}$. Note that use of Fourier analysis to extract azimuthal angles $\phi_0 = \Delta\Phi_{n,\ell,m}$ and values of $|c_n|$ works only for n components localized in ϕ. Those n components not localized in ϕ produce no time dependence in the observable $\langle y(t)\rangle$.

The spatial information encoded in the modulus $|c_n|$ and phase $\Delta\Phi_{n,\ell,m}(0) \simeq$

$\phi_0(n)$ can be extracted through Fourier analysis of experimental data. Fig. 4.12 shows the Fourier transform of the experimental data from Fig. 4.7(b), along with those of simulated survival probabilities and spatial averages. The frequency axis is labeled by the n levels characteristic of each frequency. $|c_n|$ features two peaks near $n = 306$ and $n = 302$. The corresponding phases $\Delta\Phi_{n,\ell,m}$ are $\phi_0(n \simeq 306) \simeq \pi/2$ and $\phi_0(n \simeq 302) \simeq -\pi/2$ as expected for a two-component wave packet whose components are initially localized on opposite sides of the nucleus. Figure 4.12 also includes the results of simulations undertaken using the classical trajectory Monte Carlo method with discretized energy described in Sec. 3.2.2. Calculations of $\langle y(t) \rangle$ were also undertaken and Fourier analyzed. The Fourier spectra are similar to those obtained from the calculated survival probabilities confirming that the behavior of the survival probability mimics that of $\langle y(t) \rangle$. The data demonstrate that measurements of survival probabilities can provide both the magnitude of the $\Delta n = 1$ coherences as well as their phase angle, which coincides with the geometric azimuthal angle.

Figure 4.13 shows the Fourier transform of survival probabilities measured using a mix of $n_i = 304$ and 306 states following application of a smaller pump field $F_{pump} =$ 2 mV/cm for $T_{pump} \sim 170$ ns shown in Fig. 4.7(c). The small size of F_{pump} limits the maximum energy transfer that accompanies its turn on/turn off such that it becomes comparable to the splitting of the $n_i = 304$ and 306 levels. Fourier analysis of the data yields two peaks in $|c_n|$ but the width of the overall n distribution is substantially smaller than seen in Fig. 4.12, consistent with the use of a smaller pump

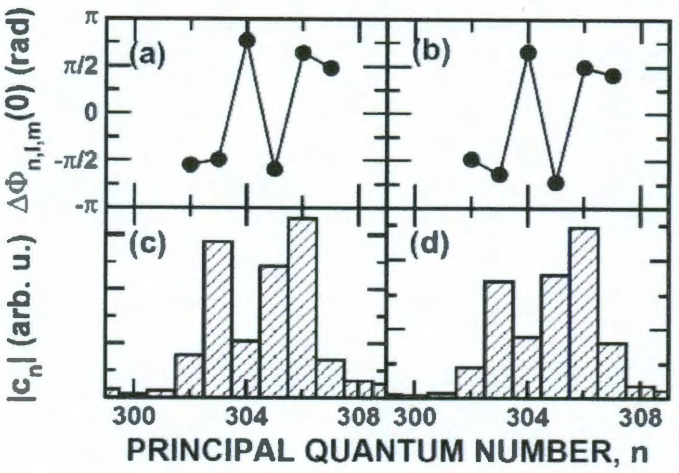

Figure 4.13 : Comparison of Fourier transforms for (a),(c) experimental survival probabilities and (b),(d) simulated survival probabilities for a pump amplitude of 2 mV/cm [67].

field. However, while in Fig. 4.12 the phase varies only weakly across each peak and increases by π from one to the other, in Fig. 4.13 a phase jump of π occurs within each peak. This indicates that each peak derives from just one of the initial parent states. The relative weight of the two peaks as determined by the integral over $|c_n|$, $\sim 40\%$ for $n \sim 303$ and $\sim 60\%$ for $n \sim 306$, is consistent with the weights expected for a statistically populated incoherent ensemble of ground hyperfine levels. This interpretation is supported by the discretized CTMC simulations. The agreement is remarkable given the susceptibility of very-high-n Rydberg states to even modest perturbations.

Fourier analysis of high-ℓ states produced from parent p states is also valuable. Fig. 4.14 shows survival probability and Fourier transform data for $n = 315$ and

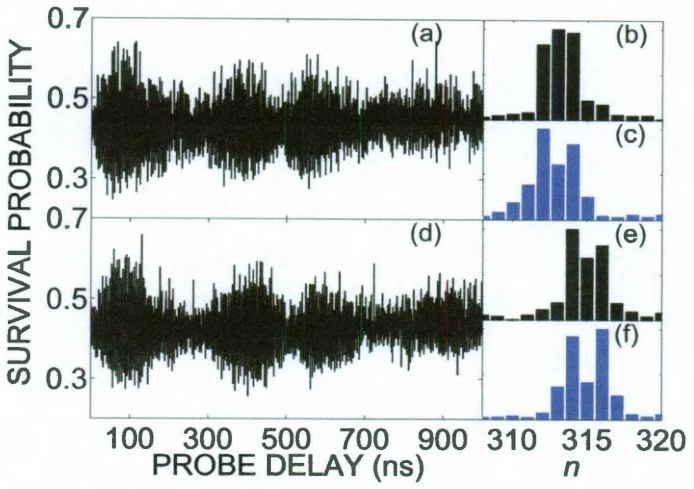

Figure 4.14 : (a),(d) Survival probabilities, (b),(e) Fourier transforms of simulated survival probabilities, and (c),(f) Fourier transforms of experimental data for $n = 315$ and $n = 317$ parent p, high-ℓ states excited from individual hyperfine levels.

$n = 317$ p states excited from individual hyperfine ground states. Note that the large quantum defect of the parent p states shifts the center of the n distributions to frequencies corresponding to lower n ($\omega_n = n^{-3}$).

As stated above, those n components not localized in ϕ produce no time dependence. Wave packet components localized at $\phi = 0$ and π during termination of the pump pulse experience no change in energy and continue to orbit at ω_{n_i}. Their contributions to $\langle y(t) \rangle$ cancel as they orbit at the same rate out of phase by π, leading to a dip in the center of the n distributions calculated by Fourier analysis. Fig. 4.15 compares Fourier transform data with calculated energy distributions. The calculations show larger populations in the center of the n distributions than observed in the Fourier transforms.

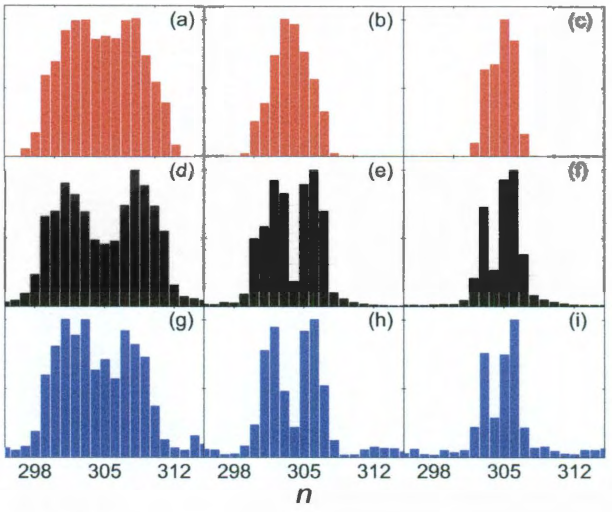

Figure 4.15 : Calculated energy distributions (red), Fourier transforms of simulated data (black), and Fourier transforms of experimental data (blue), for 10 mV/cm (left), 5 mV/cm (middle), and 2 mV/cm (right) pump fields.

Analysis of high-ℓ states, however, can be extended by adjusting the average ionization away from 0.5. The survival probability exhibits higher harmonics, each of which mirrors a higher moment $\langle y^{\lambda}(t)\rangle$ of the coordinate. Probing those higher moments provides information on the n components which cannot be detected by measuring the first moment, $\langle y(t)\rangle$. Reducing the probe strength, for instance, moves the threshold for ionization away from the x axis, as shown in Fig. 4.16. Components that originate π out of phase, along the x axis upon pump termination will now enter and exit the survival region at different times, allowing their presence to be observed on the second harmonic of the survival probability signal. Fig. 4.17 shows simulated survival probabilities for identical systems, prepared by a 10 mV/cm pump pulse, subject to probes of various amplitudes. The spectral density of the first

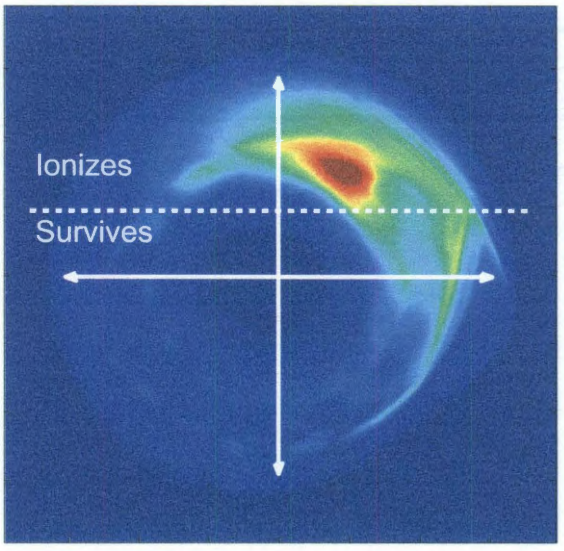

Figure 4.16 : Spatial distribution demonstrating the ionization and survival regions for a reduced strength probe.

harmonic shows a dip near the center for all amplitudes. The second harmonic, however, shows non-zero population at the center frequencies, especially when probing with very large or very small amplitudes. Fig. 4.18 displays experimental survival probability signals starting with a parent quasi-1D state, exposed to a 43 ns duration, 10 mV/cm pump pulse with fast rise/fall times, subject to 6 ns duration, 80 mV/cm, 120 mV/cm, and 160 mV/cm probe pulses. Fig. 4.19 shows the Fourier analysis of these signals. Note that the high and low n peaks in the first harmonic signal originate from approximately $\phi = 3\pi/2$ and $\pi/2$, while the center frequencies in the second harmonic originate near $\phi = 0$ and π.

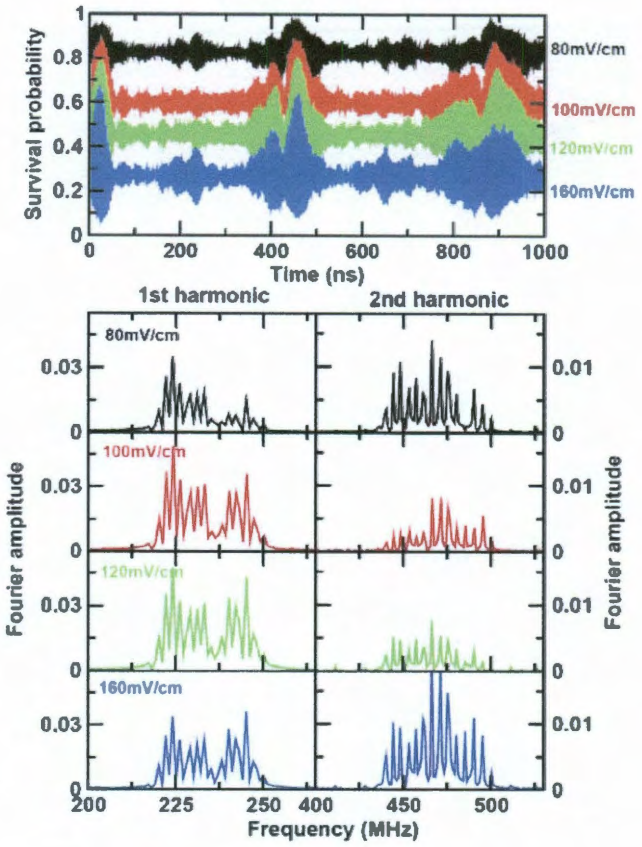

Figure 4.17 : Upper: Simulated survival probability signals for identical circular states subject to varying probe strengths. Lower: The fundamental and harmonic frequency components of each signal [47].

Fourier analysis provides a powerful tool in the analysis of wave packet characteristics. The amplitudes calculated approximate occupation probabilities, while the phases correlate to initial azimuthal angles. Harmonic analysis utilizing probe pulses that yield either ~25% or ~75% mean survival probabilities completes the picture by revealing the dynamics of symmetric components that would otherwise not be observed.

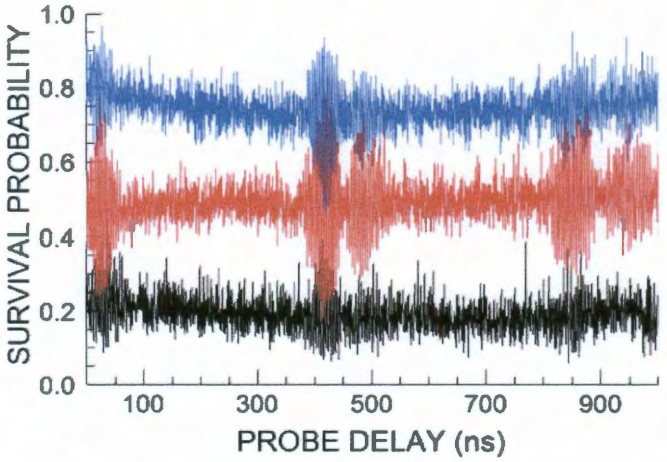

Figure 4.18 : Survival probability vs probe delay for circular states created from quasi-1D states with a 10 mV/cm, 43 ns duration pump with sudden rise/fall times subject to (blue) 80 mV/cm, (red) 120 mV/cm, and (black) 160 mV/cm probe pulses.

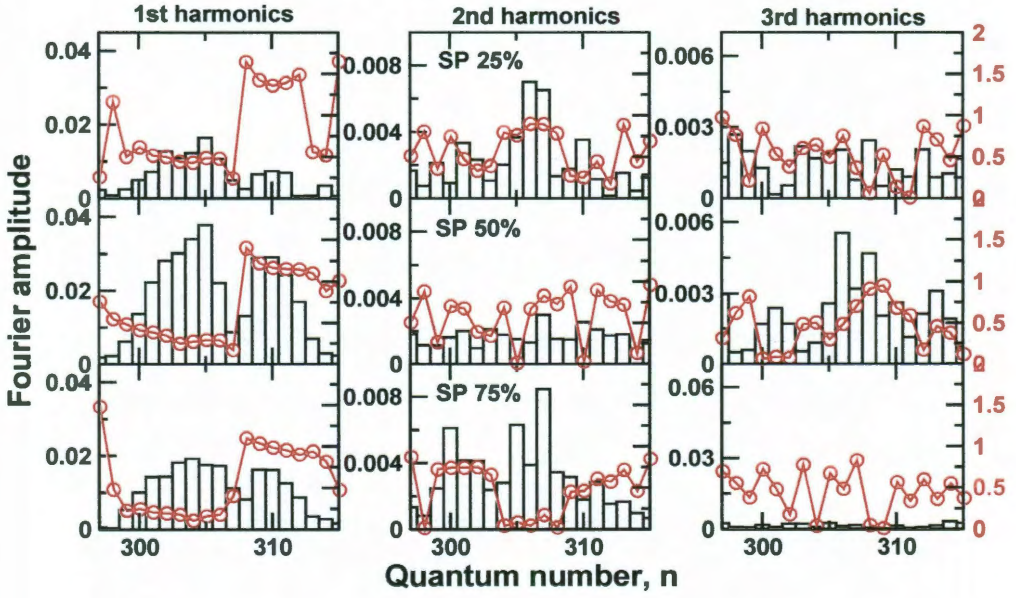

Figure 4.19 : Fourier transforms of the data in Fig. 4.18 including second and third harmonics. Modulus (bars) and phase (points) information is displayed. Data is sorted by mean survival probability, SP [47].

Chapter 5

Manipulation of Electron Wave Packets

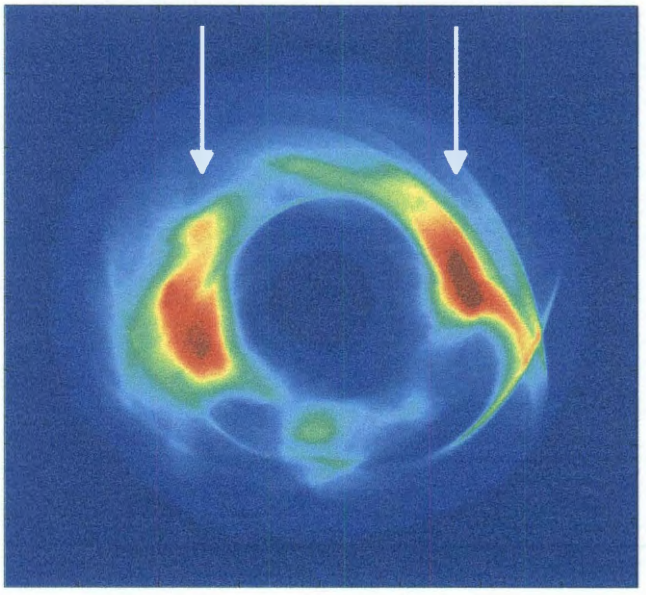

Figure 5.1 : Out of phase spatially localized components subject to an HCP.

Manipulation of high-ℓ Rydberg wave packets is accomplished through the application of individual HCPs, trains of HCPs, and sinusoidal driving. The population and phase information furnished by Fourier analysis provides precise initial conditions for analysis of manipulation schemes. Taking advantage of the strong correlation between initial phase and n allows precise manipulation of wave packets to a wide array of possible final states.

5.1 The Kicked Wave Packet

5.1.1 Individual Kicks

Recall from Sec. 3.1.4 that application of an electric field pulse whose duration is short compared to an orbital period, $T_p \ll T_n$, provides an impulsive momentum transfer

$$\Delta\vec{p} = -\int_{-\infty}^{\infty} \vec{F}(t)\, dt\,. \tag{5.1}$$

The resulting energy transfer, for initial momentum $\vec{p}_i$, is

$$\begin{aligned}\Delta E = E_f - E_i &= \left[\frac{(\vec{p}_i + \Delta\vec{p})^2}{2} - \frac{1}{r}\right] - \left[\frac{\vec{p}_i^{\,2}}{2} - \frac{1}{r}\right] \\ &= \frac{(\Delta\vec{p}\,)^2}{2} + \vec{p}_i \cdot \Delta\vec{p}.\end{aligned} \tag{5.2}$$

Wave packet manipulation utilizes kicks which are small compared to the magnitude of Rydberg electron initial momenta, $|\Delta\vec{p}| \ll |\vec{p}_i|$. As such, kicks directed parallel to orbiting electrons will receive $\Delta E > 0$, while kicks directed anti-parallel will receive $\Delta E < 0$. As $E_i < 0$ for bound orbits, parallel kicks decrease binding, effectively increasing the n level of the orbit (and, counterintuitive to the addition of momentum, reducing the speed of the orbit). Anti-parallel kicks have the opposite effect, increasing binding, which leads to a reduction in n. Fig. 5.1 illustrates a time at which two components of a wave packet moving counterclockwise are simultaneously localized on opposite sides of the nucleus (10 μm apart). Application of an HCP in the $-y$ direction (resulting in an impulse, Δp, directed in the $+y$ direction) at such time acts to lower the n levels (increase binding) of the components at $\phi = \pi$, which move in

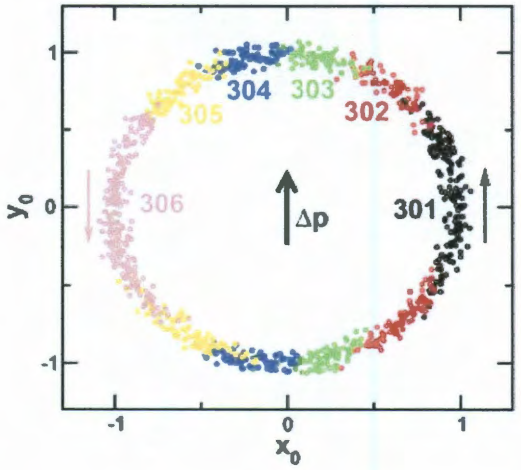

Figure 5.2 : Azimuthal distribution of n levels one quarter period after termination of the pump pulse. The relative phases between n levels is little changed [47].

the $-y$ direction, and to raise the n levels (decrease binding) of the components at $\phi = 0$, moving in the $+y$ direction. Application of this principle at times when high and low n components are well separated provides a means of adjusting the energy spread of a wave packet.

Fig. 5.2 shows the distribution of n states in azimuth one quarter period after termination of a pump pulse. The short time elapsed since production of the wave packet is insufficient to cause appreciable change in the relative phases, $\Delta\Phi_i - \Delta\Phi_j$, between components. The impulse indicated, then, acts to narrow the overall n distribution, while an impulse directed in the opposite direction would broaden the state. Fig. 5.3 displays Fourier transforms of experimental data where such pulses have been applied. For comparison Fig. 5.3(a) shows results when no extra pulse has been applied, while (b) and (c) show n distributions resulting from application

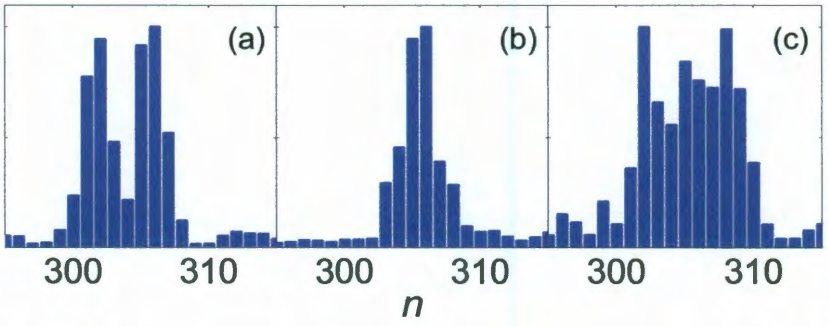

Figure 5.3 : Fourier transforms of experimental data taken after application of a 5 mV/cm, 85 ns duration pump pulse, followed one quarter period ($\sim$ 1.1 ns) later by (a) no pulse, (b) a $\Delta p_0 = n\Delta p = +0.007$ narrowing pulse, and (c) a $\Delta p_0 = n\Delta p = -0.007$ broadening pulse.

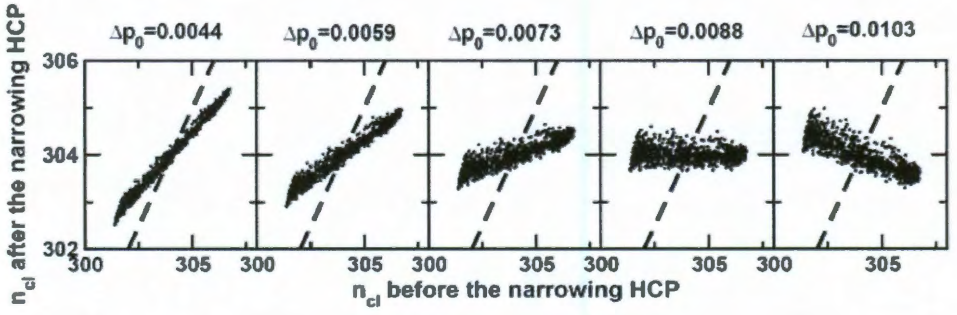

Figure 5.4 : Classical action before and after application of narrowing HCPs with the indicated strengths. The dashed line represents equal levels before and after the kicks. [47]

of $\Delta p_0 = n\Delta p = +0.007$ and -0.007 pulses, respectively, one quarter period after termination of an identical pump pulse. The value of the narrowing kick amplitude was chosen by calculating the impulse necessary to shepherd the high and low n values present in the initial state to a common value. Analysis can also be performed by simulating the final n distributions. Fig. 5.4 compares initial and final classical action, n_{cl}, for various kick strengths. The optimum kick strength produces a horizontal distribution, where all final n_{cl} levels are equal.

5.1.2 Trains of Kicks

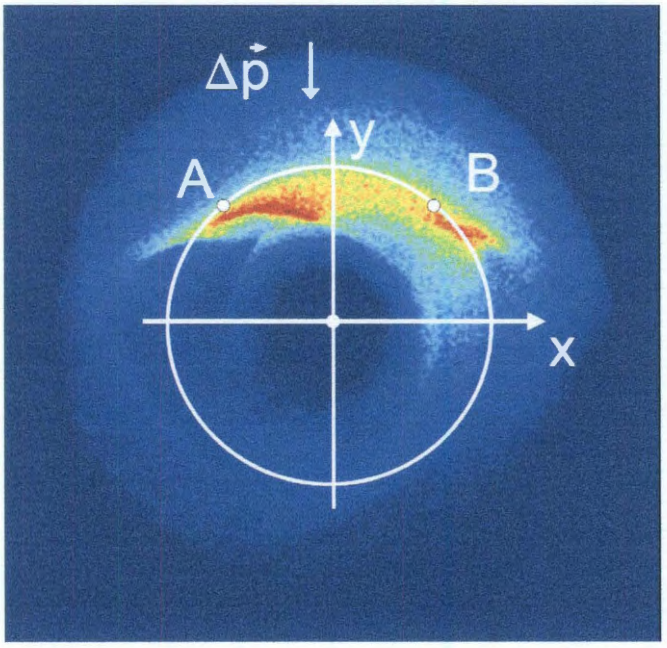

Figure 5.5 : Illustration of stabilization kick timing. Component A, in a lower n state, orbits more quickly, while component B, in a higher n state, orbits more slowly. An orbital period after localization the components have accumulated a non-zero relative phase. Application of a stabilization HCP relocalizes the distribution.

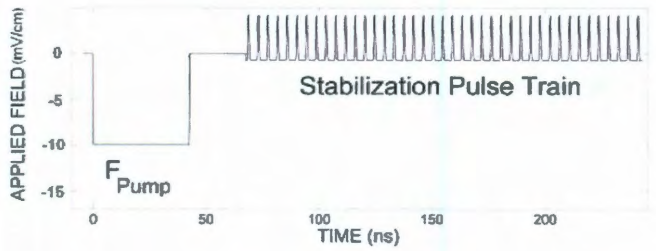

Figure 5.6 : Stabilization train profile. The train begins at the time of maximum localization. After each orbital period the components have accumulated a non-zero relative phase, and a stabilization HCP is applied to relocalize the distribution. The average dc field of the stabilization train is balanced by a dc offset field.

Consider again the case of free evolution following termination of the pump pulse. The wave packet components, initially distributed uniformly in ϕ, orbit at rates characteristic of their energy. After a number of orbits, all components come into phase simultaneously, resulting in a maximum amplitude of oscillation observed in the survival probability signal. As the wave packet continues to evolve, however, low n components, orbiting more quickly, will have accumulated a phase difference with respect to the slowly moving high n components. This effect is illustrated in Fig. 5.5, where A represents a component with lower n, while B represents a component with higher n. Application of an impulse directed in the $-y$ direction acts to relocalize the distribution. In this case, unlike that for the narrowing kicks in the previous section, the wave packet components are not located on the x axis, rather, they are close to the y axis. Though the wave packet components are relatively localized, the minimum angular width is non-zero and after another orbital period the wave packet components will again obtain a non-zero relative phase. Periodic application

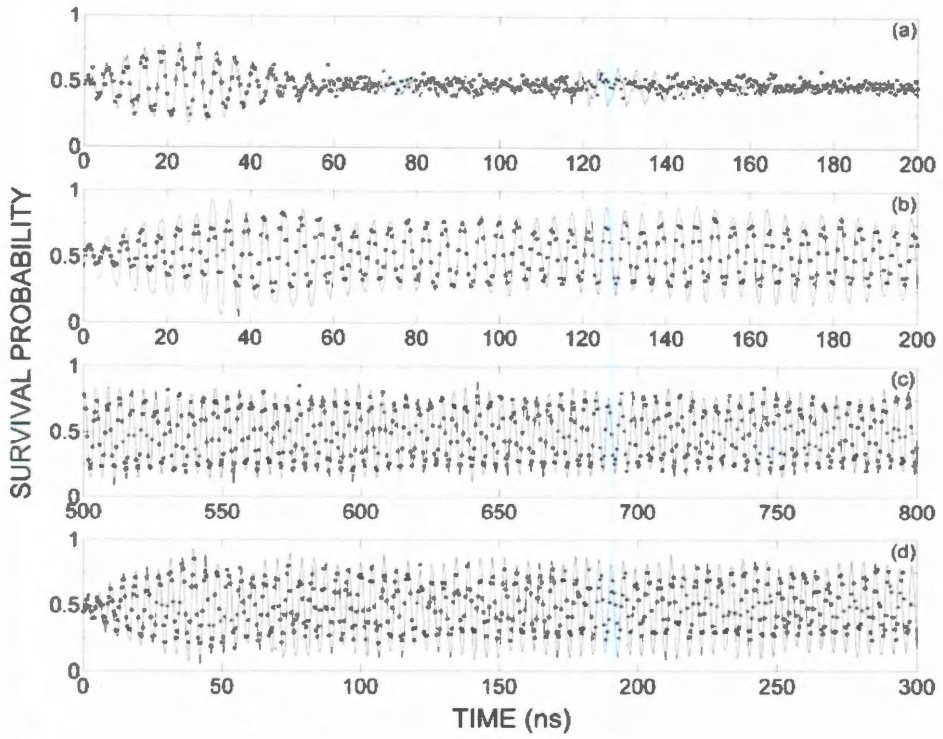

Figure 5.7 : Experimental observation of nondispersive wave packets. (a) Survival probability vs probe delay when no stabilization train is applied. (b) Survival probability signal during application of a train of 5 mV/cm, 600 ps duration HCPs with 4.3 ns period. (c) The same as (b), but at late times. (d) The same as (b), but with a train period of 8.6 ns. Points are experimental data, while the curves are CTMC simulations. [68].

of stabilization HCPs, then, is required in order to maintain localization for extended periods.

Fig. 5.6 illustrates a sample pulse profile including a periodic stabilization train. After termination of a 10 mV/cm pump field the wave packet is allowed to freely evolve until maximum localization is reached. At that time a periodic train of HCPs is applied to stabilize the wave packet. To prevent further Stark precession due to

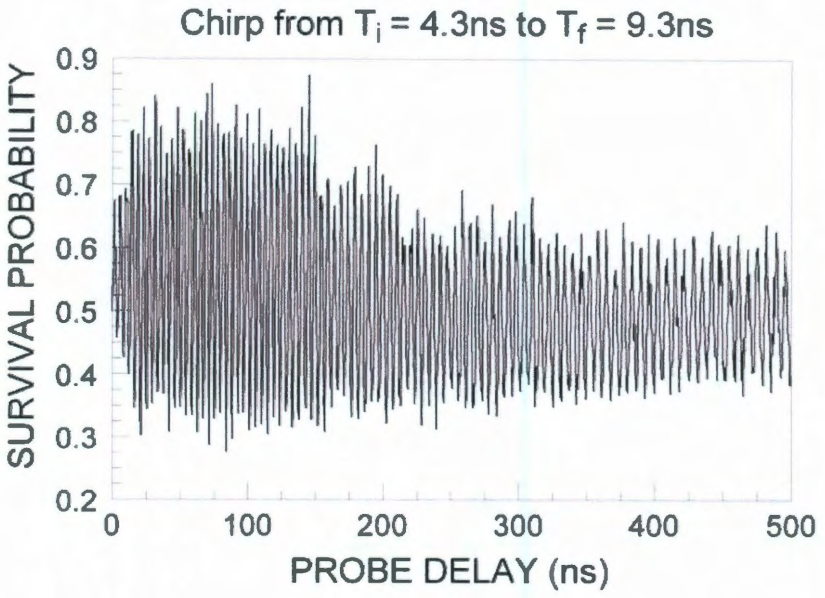

Figure 5.8 : Experimental observation of wave packets chirped to higher n. Survival probability vs probe delay during application of a train of 5 mV/cm, 600 ps FWHM HCPs with initial period 4.3 ns, chirped in steps of 0.358 ns every tenth kick to 9.3 ns after 1020 ns. The first 500 ns is shown.

the average dc field of the pulse train, an offset field is applied. Experimental results are shown in Fig. 5.7. Without a stabilization train the components will dephase, resulting in decreased amplitude of oscillation. With the train, however, wave packet evolution becomes locked into the driving field and localization can be maintained for hundreds of orbital periods. Sub-harmonic kicking, where stabilization HCPs are applied every other orbital period, also acts to maintain localization.

Once locked onto the external driving, the wave packet is able to follow small changes in drive frequency allowing it to be transported to states of higher (or lower) n. Fig. 5.8 shows the first 500 ns of survival probability vs probe delay measurements

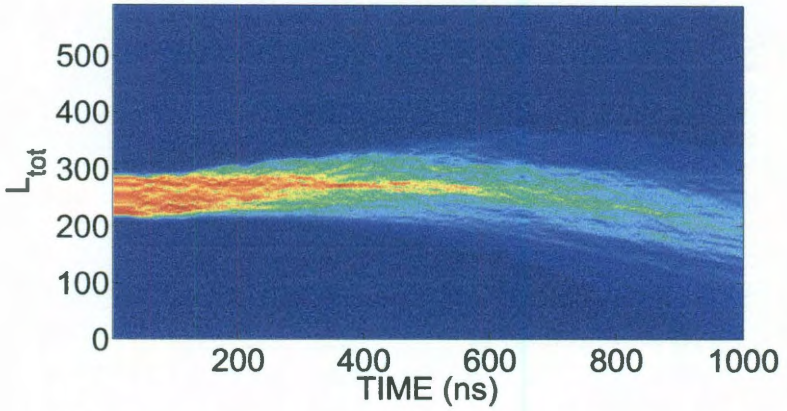

Figure 5.9 : Angular momentum distribution during the kicked chirping sequence.

for circular states exposed to a chirped kick sequence. Quasi-1D states are initially exposed to a -10 mV/cm, 43 ns duration pump pulse with rise/fall times $\sim$ 0.3 ns. Approximately 27 ns after pump termination a sequence of 5 mV/cm, 600 ps FWHM HCPs with 4.296 ns period, resonant with the initial n levels present, is applied. Every tenth pulse the period of driving is increased by 0.358 ns out to 9.308 ns, resonant with $n = 396$. Clearly, the period of the oscillations in survival probability increases as the drive frequency is chirped, however, the amplitude of the oscillations decreases. The probe used during the experiment had a fixed 120 mV/cm amplitude, sufficient to ionize 50% of the parent $n \sim 305$ states. As n increases with driving the scaled strength of the 120 mV/cm probe pulse also increases, leading to a reduced amplitude of oscillation. Alone, however, this is insufficient to explain the magnitude of the decrease in oscillation amplitude. CTMC calculations of the evolution of the angular momentum distribution during the kicked chirping sequence are displayed in

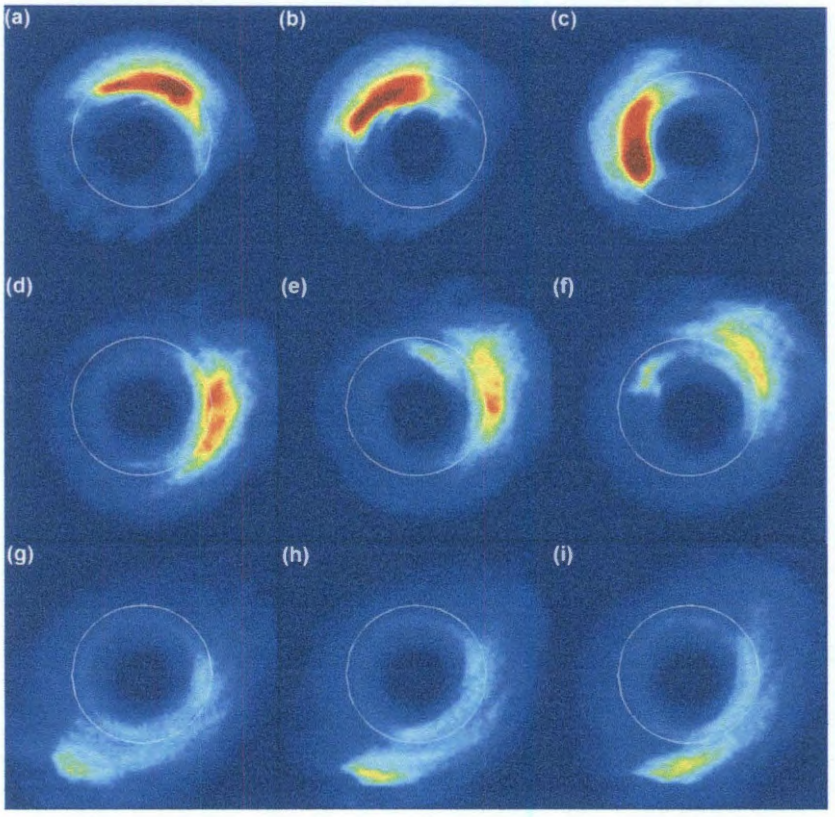

Figure 5.10 : Simulated spatial distributions during a chirped sequence of kicks. The white circle is the same in all frames to provide a radius reference. (a), (b), and (c) Spatial distributions near 27 ns after pump termination, while localization is near maximum. (d), (e), and (f) Spatial distributions near 340 ns after pump termination. The driving period is 6.09 ns, corresponding to $n = 344$. (g), (h), and (i) Spatial distributions near 905 ns after pump termination. The driving period is 8.59 ns, corresponding to $n = 385$.

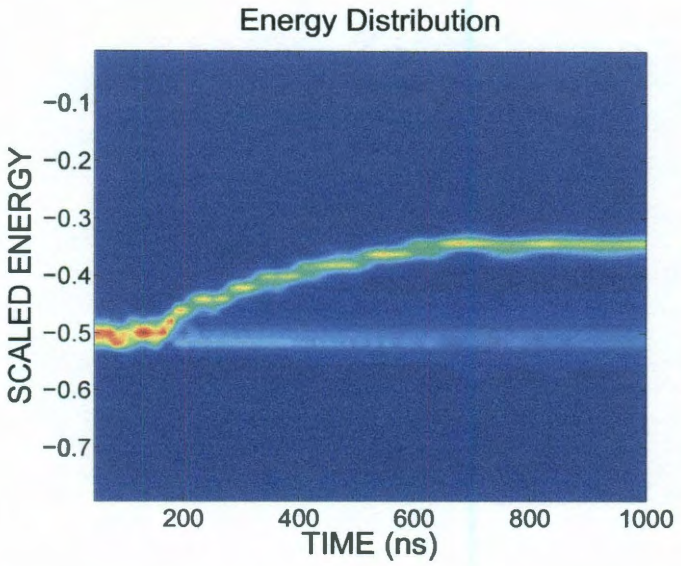

Figure 5.11 : CTMC simulations of energy distribution evolution during the chirped sequence of kicks.

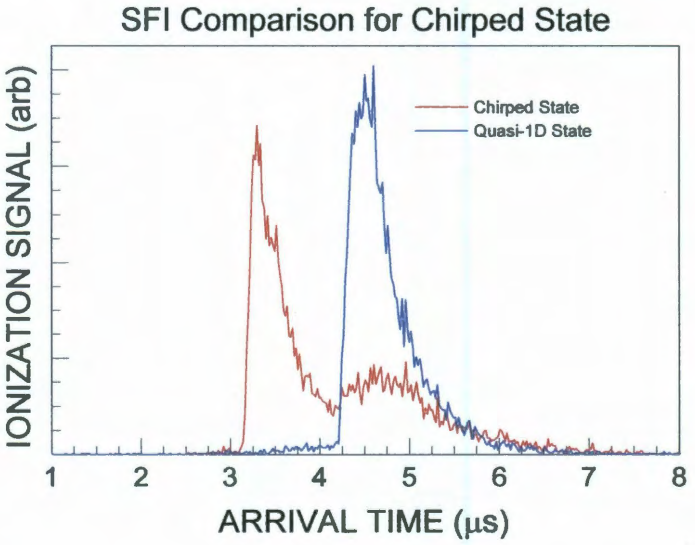

Figure 5.12 : Selective field ionization measurements for an initial quasi-1D state (blue) and the final state after the chirped sequence of kicks (red). Data are collected using a linear ionization ramp.

Fig. 5.9. The kicking sequence acts to broaden the angular momentum distribution, resulting in wave packet delocalization. This effect is also shown in Fig. 5.10, where it can be observed that the eccentricity of the orbits increases at late times. The simulated energy distribution during the sequence is shown in Fig. 5.11. Note that a sizable portion of the wave packet does not lock into the drive field. This is also demonstrated in the experimental selective field ionization (SFI) measurements shown in Fig. 5.12. Recall that higher energy electrons will ionize earlier in the application of the SFI ramp.

Trains of equi-spaced HCPs are efficient in stabilizing wave packet localization, leading to the creation of nondispersive Bohr-like wave packets. A chirped sequence of HCPs is capable of transporting electron wave packets to higher n, but the efficiency of the process, as well as its inability to maintain circular orbits, limits its usefulness in atomic engineering.

5.2 Sinusoidal Driving

The quality of stabilization provided by trains of HCPs can be analyzed through the use of Poincaré surfaces of section. Detailed discussion of Poincaré sections can be found elsewhere (*e.g.*, Ref. [69]). Briefly, however, Poincaré sections contain points obtained each time a trajectory passes through a specified section of phase space, typically sampled periodically corresponding to some external driving frequency, providing an illustration of stable parameters represented by clusters of points (islands).

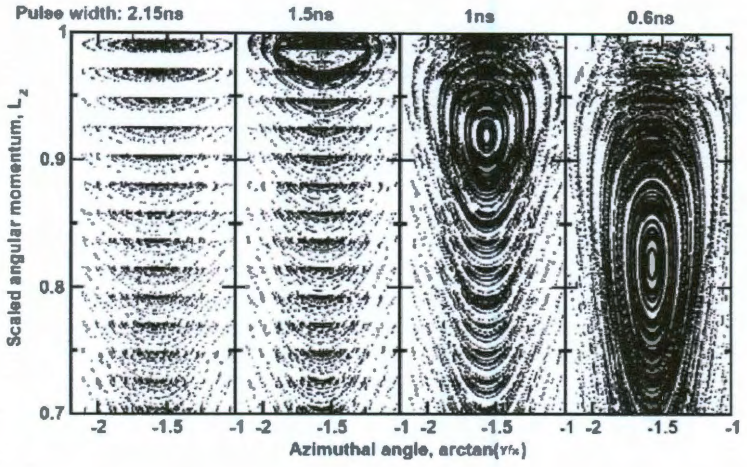

Figure 5.13 : Poincaré surface of section for a periodically kicked atom in the presence of an offset field with $\Delta p_0 = -0.01$, $\nu_0 = 1$, cut at $z = p_z = 0$, $xp_x + yp_y = 0$, and $E_0 = -0.5$ [47].

Poincaré sections calculated for orbits subject to a train of pulses, with indicated widths, are presented in Fig. 5.13. Trains of short pulses provide a large island of stability, centered around $L_z \approx 0.8$. The broad distribution of parameters stabilized by such a train precludes maintenance of tightly localized circular orbits. As the pulse width is increased the islands of stability become more tightly focused near $L_z \approx 1$. In the limit of linearly polarized microwave fields (sinusoidal driving) near perfect stability can be achieved.

To produce the necessary sinusoidal driving a Chase Scientific DA12000 arbitrary waveform generator, discussed in Sec. 2.5, was obtained. Fig. 5.14 shows the pulse profile during sine driving. Experimental results for quasi-1D states, subjected to a 5 mV/cm, 85 ns pump pulse, and later driven by a 5 mV/cm pk-pk sinusoidal electric field with constant 4.3 ns period are presented in Fig. 5.15. Just as with the train of

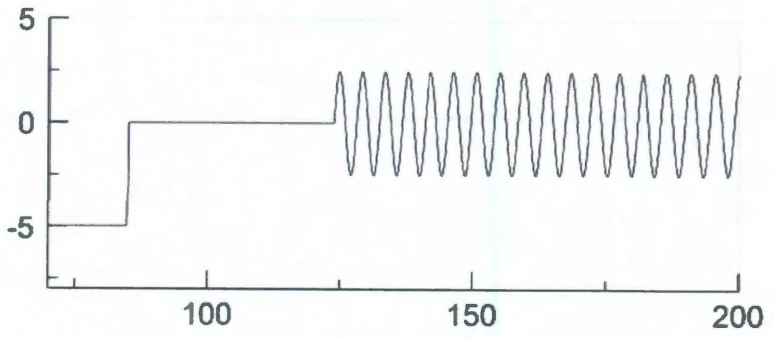

Figure 5.14 : Pulse profile including a 5 mV/cm pump pulse, followed $\sim$ 38.8 ns later by a 5 mV/cm pk-pk sine wave.

kicks, maintenance of a nondispersive Bohr-like wave packet is achieved.

Chirping the frequency of the drive is also found to be effective. Fig. 5.16 shows experimental results obtained when the sine driving period is chirped from $T_i = 4.3$ ns to $T_f = 32.7$ ns, resonant with $n = 600$, over 1 μs. Given that the ionization threshold of $n = 600$ Rydberg atoms (which scales as n^{-4}) is $\sim$ 4.5 mV/cm, the amplitude of the sine driving was linearly reduced from 10 mV/cm to 2.5 mV/cm during the duration of the drive. The probe strength was also adjusted between the two frames shown in Fig. 5.16: $F_{probe} = 120$ mV/cm for the upper frame, $F_{probe} = 60$ mV/cm for the lower frame.

The simulations in Fig. 5.17 show a much tighter angular momentum distribution during the course of the driving, though not all orbits are locked to the drive field due to the narrower islands of stability. As displayed in Fig. 5.18 the average angular momentum does increase during the experiment, as opposed to the case during a chirped sequence of kicks. The eccentricity of the orbits can also be inferred by

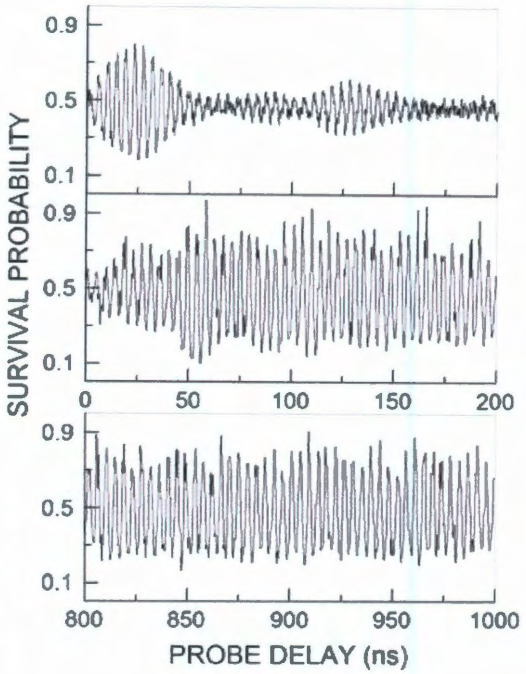

Figure 5.15 : Survival probability vs probe delay following sudden termination of a 5 mV/cm, 85 ns pump pulse (top) without driving, (center) followed $\sim$ 38.8 ns later by a 5 mV/cm pk-pk sine wave with constant period 4.3 ns, and (bottom) same as center at late times.

calculation of the evolution of the average wave packet spatial coordinates. The amplitude of the oscillations in both the x and y directions in Fig. 5.19 remain almost equal, as required for circular motion.

The calculations in Fig. 5.18 suggest more efficient energy transport than achieved with HCP driving. This is verified in Fig. 5.20, where experimental SFI spectra are presented for circular states exposed to sine driving for the cases of no chirping, chirping to $n \sim 400$, and chirping to $n \sim 600$. The number of counts in the vicinity of 4 μs arrival times, characteristic of ionization of parent $n \sim 300$ states, is extremely

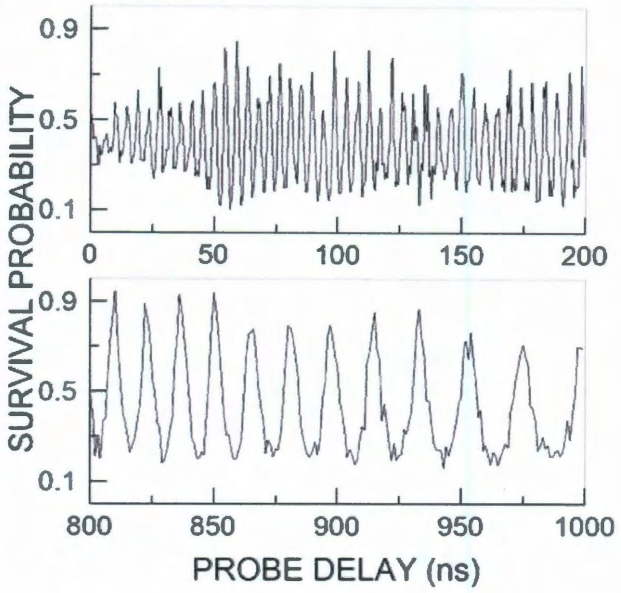

Figure 5.16 : Survival probability vs probe delay following sudden termination of a 5 mV/cm, 85 ns pump pulse followed $\sim$ 38.8 ns later by a 5 mV/cm pk-pk sine wave whose period is chirped from 4.3 ns (resonant with $n = 305$) to 32.7 ns (resonant with $n = 600$), over 1 μs. The final period is instantaneous; the effective final period over the final oscillation is closer to 24 ns, resonant with $n = 540$.

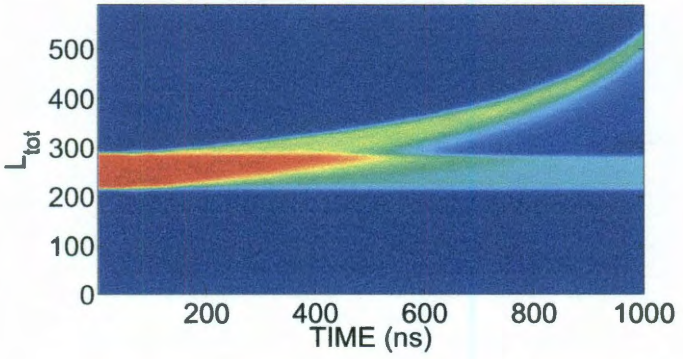

Figure 5.17 : Angular momentum distribution during chirped sine driving

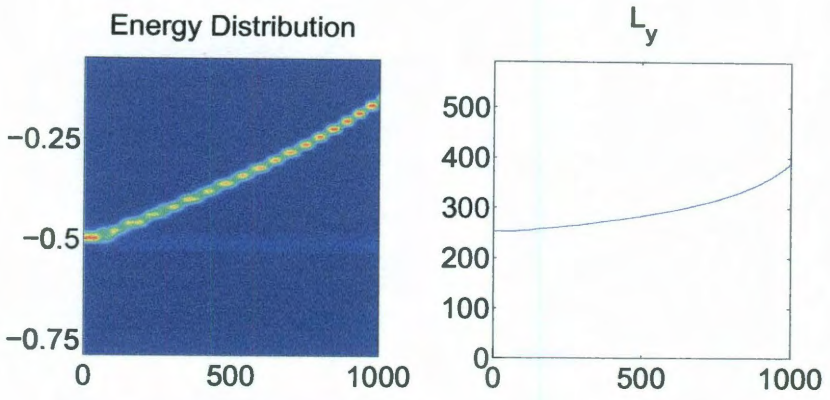

Figure 5.18 : Left: Energy distribution during chirped sine driving. Right: Average angular momentum during chirped sine driving.

low following application of the chirped sine wave. This is indicative of efficient energy transfer. Integrating the area under the high and low n peaks separately yields transport efficiencies in excess of 70%.

High-ℓ Rydberg atoms, then, are a good laboratory in which to study the dynamics of driven systems. Careful control of stray fields and drive characteristics makes possible the engineering of a wide array of atomic states. Impulses provided by short HCPs nudge wave packet components into desired final states. Trains of such pulses are capable of transferring energy into the system, transporting wave packets to higher n, however, they also act to broaden the angular momentum distributions and are not very efficient. Sinusoidal electric fields are capable of accomplishing many of the same tasks, but are able to do so with greater efficiency and without significantly broadening the angular momentum distribution.

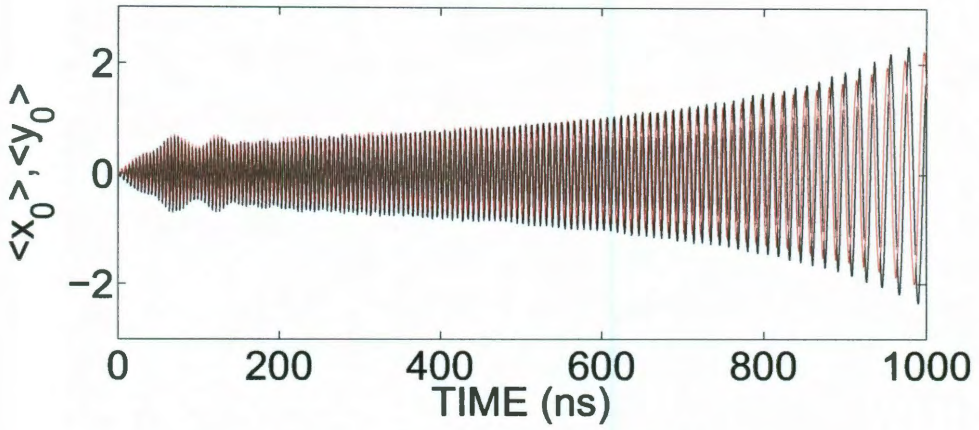

Figure 5.19 : Evolution of the average spatial coordinates, scaled to the initial n, during chirped sine driving

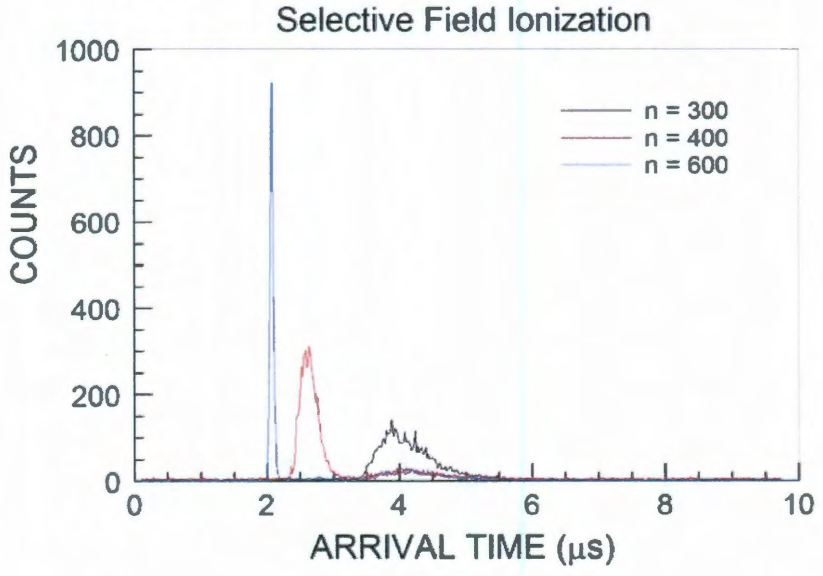

Figure 5.20 : Selective field ionization measurements after 1 μs of (black) constant period sine driving near $n \sim 300$, (red) sine driving from $T_i = 4.3$ ns to $T_f = 9.6$ ns, resonant with $n \sim 400$, and (blue) sine driving from $T_i = 4.3$ ns to $T_f = 32.7$ ns, resonant with $n \sim 600$.

Chapter 6

Decoherence by Collisions and Electrical Noise

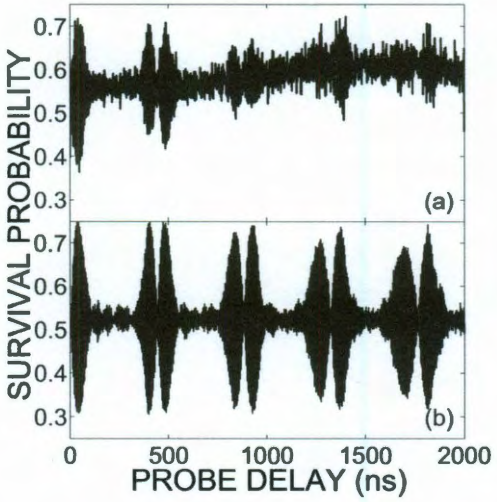

Figure 6.1 : Comparison of (a) experimental and (b) simulated survival probability signals for high-ℓ states derived from p parent states. Stray fields in the interaction region cause intrinsic dephasing.

The high-ℓ wave packets studied in the present work maintain coherence for hundreds of orbital periods. Stray electric fields in the experimental apparatus, however, cause observable dephasing. Fig. 6.1 compares experimentally measured and simulated survival probabilities over 2 μs. Noticeable in the experimental data is a reduction in revival amplitude with time and a drift in mean survival probability. The latter can be understood by considering the method of canceling stray fields and

Figure 6.2 : Model noise profile. After termination of the pump pulse noise fields randomly switch between $+F$ and $-F$ at characteristic frequencies.

the Rydberg atom velocities in the interaction region. As described in Sec. 2.3, stray fields are canceled by application of offset fields to the plate electrodes which make up the apparatus. These fields balance in a small volume near the center of the interaction region. The Rydberg atoms, meanwhile, travel at $\bar{v}_{Ryd} \approx 570$ m/s (about half a millimeter per microsecond). During the course of the experiment the Rydberg atoms travel out of the zero field region, causing a drift in mean survival probability. Understanding the effects of stray noise on revival amplitude, even for short times when the Rydberg atoms are still near the zero field region, is the emphasis of the current chapter. Possible decoherence caused by collisions with background gases is also considered. In addition to reductions in quantum revival amplitude, the application of noise and background gases produce an overall reduction in count rates. In order to obtain a sufficient number of experimental counts within a reasonable time the work that follows utilized high-ℓ wave packets derived from parent p states due to the larger transition probabilities excitation to those states provides.

6.1 Electrical Noise

Given the baseline decoherence observed in the survival probability signal when no external noise is applied, the study of the effects of external noise will focus on the first quantum revival. A cartoon representation of a typical noise signal is illustrated in Fig. 6.2. The noise is gated to begin immediately following termination of the pump pulse. The noise generator separates time into bins whose width, Δt, is user adjustable, but is fixed during each experimental run. In each time bin the generator will output $+F$ or $-F$ with 50% probability. The noise is represented by

$$F_{noise}(t) = \sum_{j \geq 1} F_j \chi_j^{\Delta t}(t), \tag{6.1}$$

where $\chi_j^{\Delta t}(t)$ is the characteristic function of the interval $[(j-1)\Delta t, j\Delta t]$ and $F_j = \pm F$. The spectral characteristics, *i.e.*, Fourier transform, of the noise can be controlled by varying Δt. Since an alternating sequence of fields $+F$ and $-F$ results in a periodic waveform, the characteristic frequency of the noise is defined as $\nu_{noise} = 1/(2\Delta t)$.

Decohering quantum dynamics can be treated using the Monte Carlo wave function method. The initial ensemble is a statistical mix of states, $|\psi_{n,m}\rangle$, which are the wave packets prepared deterministically (without noise) by the pump pulse, *i.e.*, $|\psi_{n,m}(0)\rangle = U(0, t_{pump})|n, 1, m\rangle$ where $U(0, -t_{pump})$ is the time evolution operator during the pump. The relevant quantum numbers correspond to those before the pump pulse ($n = 304, 306; m = -1, 0, 1; \ell = 1$). Accordingly, the initial density

matrix

$$\rho(0) = \sum_{n,m} P_{n,m} |\psi_{n,m}(0)\rangle\langle\psi_{n,m}(0)|, \tag{6.2}$$

evolves under the influence of a stochastic Hamiltonian

$$H(t) = H_{at} + yF_{noise}(t), \tag{6.3}$$

through the evolution of each wave packet with populations $\{P_{n,m}(0)\}$,

$$|\psi_{n,m}^{(\mu)}\rangle = U^{(\mu)}(t,0)|\psi_{n,m}(0)\rangle, \tag{6.4}$$

where $U^{(\mu)}(t,0)$ is the evolution operator. The average over an ensemble of different stochastic realizations ($\mu = 1, 2, 3, \ldots$) of $U^{(\mu)}(t,0)$

$$\rho(t) = \sum_{\mu} \sum_{n,m} P_{n,m} |\psi_{n,m}^{(\mu)}(t)\rangle\langle\psi_{n,m}^{(\mu)}(t)|, \tag{6.5}$$

provides an approximate solution of the Liouville-von Neumann equation which becomes exact in the limit of infinite random realizations [64]. In the present case of a piecewise constant noise field (Eq. 6.1), the evolution operator is given by

$$U^{(\mu)}(t,0) = \prod_{j} U_j^{(\mu)} = \prod_{j} e^{\left[-i\Delta t(H_{at} + yF_j\chi_j^{(\mu)})\right]}. \tag{6.6}$$

Eq. 6.6 highlights the two mechanisms responsible for decoherence. First, the complex phase of each quantum state evolves at a different rate which represents a Stark shift. This can be viewed as an inhomogeneous broadening of the energy levels. Secondly, at each transition of the noise field the evolution operator undergoes a sudden jump. Such jumps drive inelastic transitions to nearby states and result in a

random walk in state space. The transition probabilities at the random jumps can be resonantly enhanced by tuning the characteristic noise frequency ν_{noise} close to the Kepler frequency $\nu_{Kepler} \sim 1/(2\pi n^3)$.

Developing a quasi-classical approximation to the stochastic quantum evolution (Eq. 6.6) is not straightforward, even for very high n Rydberg states. While the behavior of a classical wave packet whose principal action is discretized immediately following the pump pulse successfully describes the quantum revivals seen in the absence of noise (see Fig. 6.1), classical evolution in the presence of noise, as will be shown, fails to approximate the quantum evolution. This happens because the initially-quantized trajectories do not remain quantized. QCTMC simulations are presented here in which the frequency spectrum of the wave packet is kept quantized but is modified to account for the decoherence mechanisms identified, *i.e.*, inhomogeneous broadening and broadening induced by the random transitions in the noise field.

Inhomogeneous broadening is the result of the Stark shift in the Kepler frequency induced by the noise field [70]. Accordingly, the new quantized energy levels to which the classical phase space variables are rescaled become

$$E_{n,k} = -\frac{1}{2(n+1/2)^2} + \frac{3}{2}nkF, \tag{6.7}$$

with frequencies

$$\Omega_{n,k} = \frac{\partial E_{n,k}}{\partial n} = \frac{1}{(n+1/2)^3} + \frac{3}{2}kF. \tag{6.8}$$

Because for high-ℓ wave packets derived from parent p states, the y component of

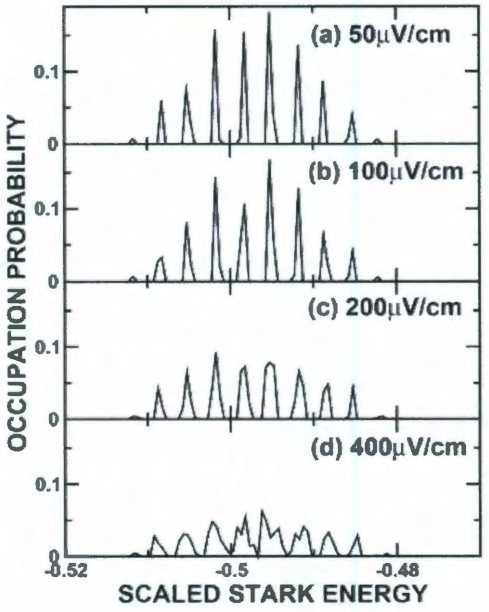

Figure 6.3 : Line broadening of wave packet components caused by external fields. The initially discrete states approach a quasi-continuum with increased field amplitude. Line broadening is independent of noise frequency [64].

the Runge-Lenz vector, A_y, is uniformly distributed in $[-1, 1]$, the electric quantum number $k \sim nA_y$ is also uniformly distributed in $[-n, n]$ leading to non-negligible line broadening. The resulting line broadening is shown in Fig. 6.3 as a function of noise amplitude. As the noise amplitude increases the system evolves towards a quasi-continuum, *i.e.*, towards the spectrum typical of an open quantum system. The effects of line broadening are then modeled by considering the free evolution of the broadened distribution of initial discrete states.

The effects of the jumps between n levels induced by sudden switching of the noise field can be incorporated by assuming a random walk in n with jumps of unit step

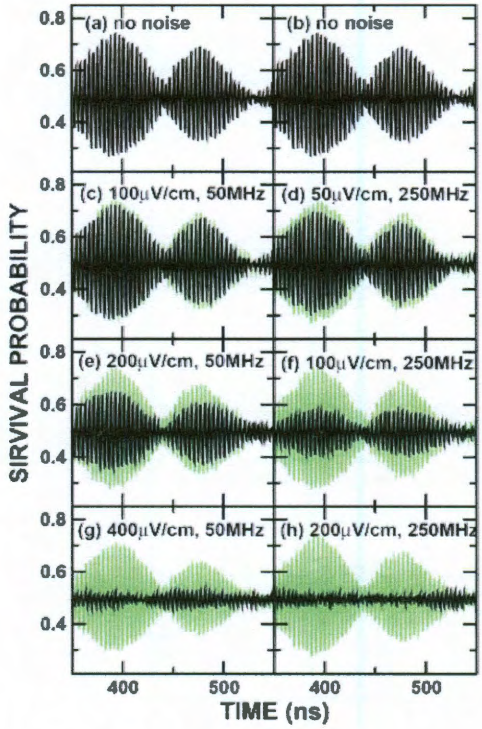

Figure 6.4 : Quantum revival damping due to (green) line broadening alone and (black) both line broadening and energy diffusion caused by external noise fields [64].

size between neighboring (broadened) n levels. This process can be characterized by a diffusion constant $D = \langle(\Delta n)^2\rangle/(2t)$. The diffusion coefficient is estimated by running CTMC simulations of the energy broadening in which the initial quantized trajectories are propagated in the presence of the noise field. The resulting diffusion rate is then used as an input parameter for simulations of the (free) evolution of the system that include a discrete random walk in n, *i.e.*, energy, with a jump rate D. This approach maintains a quasi-discrete frequency spectrum.

The relative importance of these two decohering mechanisms can be judged from

Fig. 6.4 which shows the calculated damping of the first revival as a function of both the noise amplitude, F, and its characteristic frequency, ν_{noise}, when including only line broadening and when including both line broadening and energy diffusion. Overall, energy diffusion is seen to be much more efficient in suppressing revivals. Moreover, it is sensitive to the frequency spectrum of the noise because resonant coupling when $\nu_{noise} \sim \nu_{Kepler}$ significantly enhances the diffusion rate.

The accuracy of the QCTMC simulations can be gauged by comparing them to fully quantum simulations (Eqs. 6.5 and 6.6). Fig. 6.5 shows calculated expectation values $\langle y(t) \rangle$ for $n = 150$, a value of n for which an adequate number of random realizations can be treated within a reasonable computing time. The quantum predictions are compared to those obtained using CTMC calculations in which the initially-quantized trajectories are propagated in the presence of noise and using QCTMC calculations in which a broader distribution of quantized trajectories are freely propagated, this distribution being governed by line broadening and energy diffusion induced by the noise. QCTMC simulations undertaken using a broadened distribution of discrete states remain in good agreement with the quantum results, which is remarkable considering the approximations inherent in this model. However, as noted earlier, CTMC simulations that simply follow the initial quantized trajectories in the noise field fail to correctly reproduce the revivals.

The effects of electrical noise were studied experimentally by application, immediately following turn-off of the pump field, of synthesized noise. The time averaged

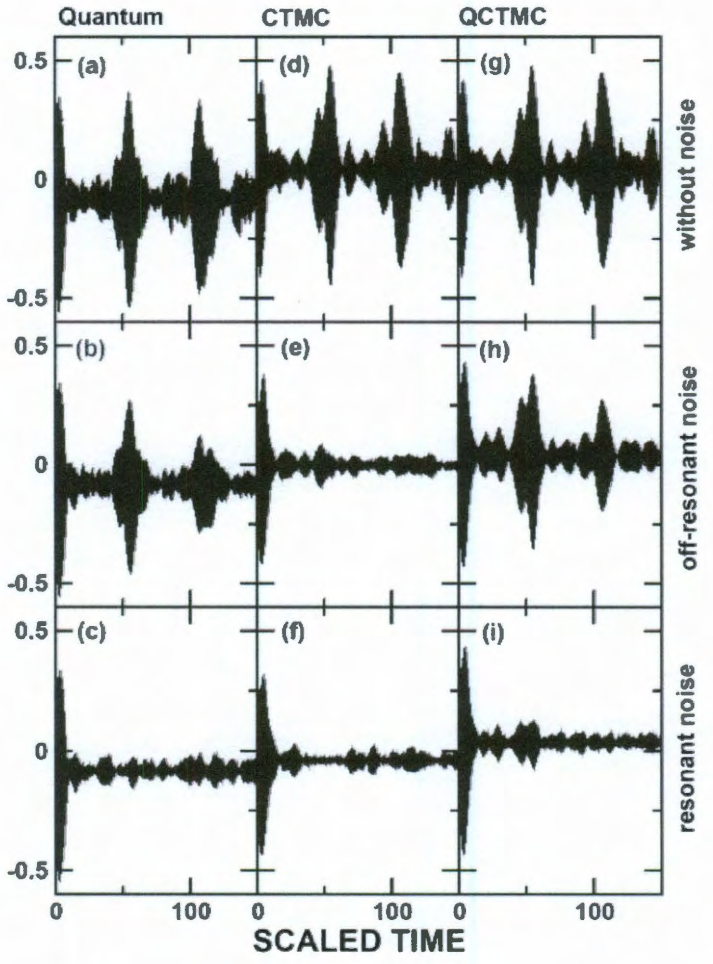

Figure 6.5 : Scaled position calculations for high-ℓ wave packets derived from parent 150p states. Results are shown for (left) fully quantum calculations, (center) CTMC simulations with energy discretization in the presence of noise fields, and (right) QCTMC simulations where modified trajectories are freely propagated. Noise is simulated with characteristic scaled frequencies of 0.4 (off-resonance) and 1.1 (near-resonance) for scaled noise amplitudes of $F_{noise} = 0.03F_{pump}$ [64].

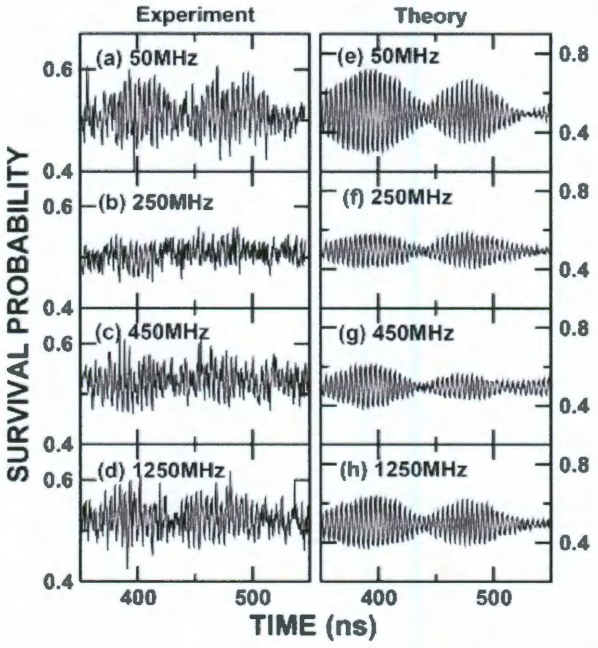

Figure 6.6 : Measured survival probabilities near the first quantum revival in the presence of noise with characteristic frequencies indicated [64].

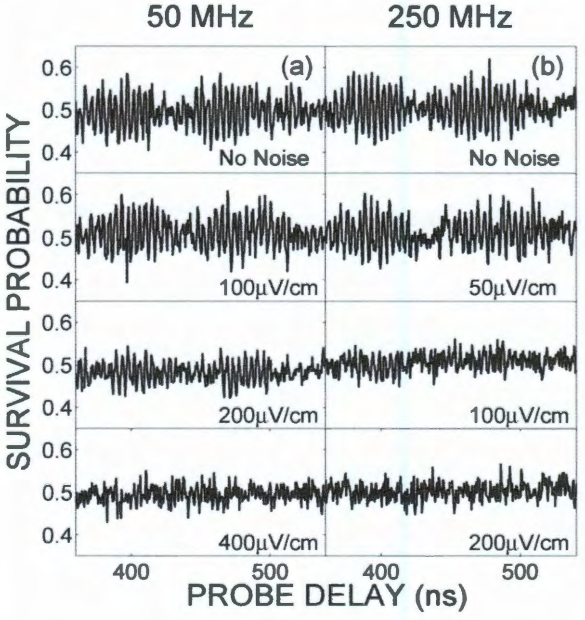

Figure 6.7 : Measured survival probabilities near the first quantum revival in the presence of noise [64].

field experienced by the atoms during application of the noise is zero, thereby limiting spurious precession of the electron orbits. The probability that a single Rydberg atom is excited during any laser pulse is small, < 0.1, and data must therefore be accumulated over many experimental cycles, each of which corresponds to a different random noise sequence. As demonstrated in Fig. 6.6, the dephasing of the first revival depends markedly on the noise frequency ν_{noise} and the data point to strong resonant enhancement of stochastic diffusion when $\nu_{noise} \sim \nu_{Kepler}$. The experimental data are in good qualitative agreement with the predictions of the free evolution model and confirm that stochastic energy, *i.e.*, state, diffusion is the primary mechanism responsible for decoherence. As illustrated in Fig. 6.7, the size of the first revival decreases monotonically with increasing noise amplitude for all noise frequencies. The larger the noise amplitude, the more efficiently the first revival is suppressed.

6.2 Collisions

Collisions of Rydberg atoms with ambient gas atoms provide another potential source of decoherence. The rate for this depends on the nature of the ambient target gas and its density, ρ. Experiments, however, revealed that the revivals are relatively insensitive to collisions. Measurements shown in Fig. 6.8 of the first revival with and without CO_2 target gas present at a pressure of $\sim 1 \times 10^{-5}$ Torr, *i.e.*, a density $\sim 3 \times 10^{11}\text{cm}^{-3}$ (the highest density that could be used in the present apparatus), provide no evidence of a significant reduction in the amplitude of the revival. This

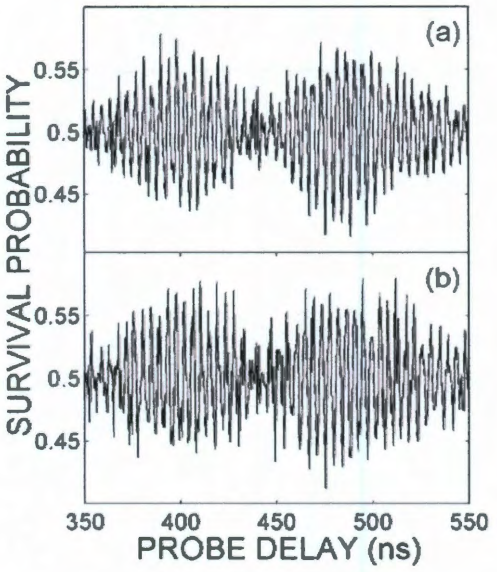

Figure 6.8 : Comparison of quantum revival amplitudes (a) without gas present (a base pressure of $\sim 10^{-8}$ Torr) and (b) with $\sim 10^{-5}$ Torr background CO_2 present.

lack of collisional decoherence can be explained within the framework outlined above by analyzing the system-environment interaction using the essentially-free electron model of Rydberg atom collisions [55, 56, 71]. Accordingly, the electron is treated as an independent particle, except that its velocity distribution is determined by its Compton profile. The electron undergoes a sequence of sudden collisions with CO_2 molecules after random time intervals Δt_j that result in random momentum transfers Δp_j such that the evolution operator becomes

$$U^{(\mu)}(t,0) = \sum_j e^{-i\Delta t_j H_{at}} e^{i\vec{r}\cdot\Delta\vec{p}_j}. \tag{6.9}$$

The main differences between collisional decoherence and that for noise is that the time intervals are random and the electron evolves without collisions between jumps.

Consider the mean collision time, $\tau_c \sim \langle \Delta t_j \rangle$. Since the mean electron velocity $\langle v_e \rangle \sim 1/n \sim 10^4$ m/s is much greater than that of either the K^+ core ion or the CO_2 target molecule, the time between Rydberg electron-CO_2 collisions can be written approximately as $\tau_c \approx \left(\langle v_e \rangle \rho \sigma_e\right)^{-1}$ where σ_e is the cross section for elastic scattering of the electron. At $n \sim 300$ the electron energy is small, ~ 150 μeV, and it is reasonable to assume that σ_e is given by the s-wave scattering zero-energy limit $\sigma_e \sim 4\pi a^2$, where $a \approx 7$ a.u. is the scattering length [59]. This yields $\sigma_e \approx 1.5 \times 10^{14}$ cm^2 and a collision time $\tau_c \approx 87$ μs. Thus, the vast majority of trajectories do not undergo any jump during the (sub)microsecond scales investigated in the present work and both stochastic diffusion and broadening are completely suppressed. The likely contribution of inhomogeneous line broadening to dephasing is given by the "Fermi shift" [35] and can be estimated from the energy shift produced by a short-ranged s-wave scattering potential (in a.u.), $V = 2\pi a \delta(\vec{r})$, as

$$\langle V \rangle \approx \langle N_{CO_2} \rangle 2\pi a \langle |\psi|^2 \rangle \approx 2\pi a \rho, \tag{6.10}$$

where $\langle |\psi|^2 \rangle$ is the average probability density of the Rydberg electron (occupying a volume $\sim 1/\langle |\psi|^2 \rangle$) and $\langle N_{CO_2} \rangle \approx \rho / \langle |\psi|^2 \rangle$ is the number of CO_2 molecules within the volume of a Rydberg atom. For the present target densities such shifts are extremely small, ~ 100 Hz, indicating that the effects of line broadening are negligible. The present findings are consistent with earlier theoretical studies of the damping of Stark beats through collisions with xenon which has an electron s-wave scattering length similar to that of CO_2 [71].

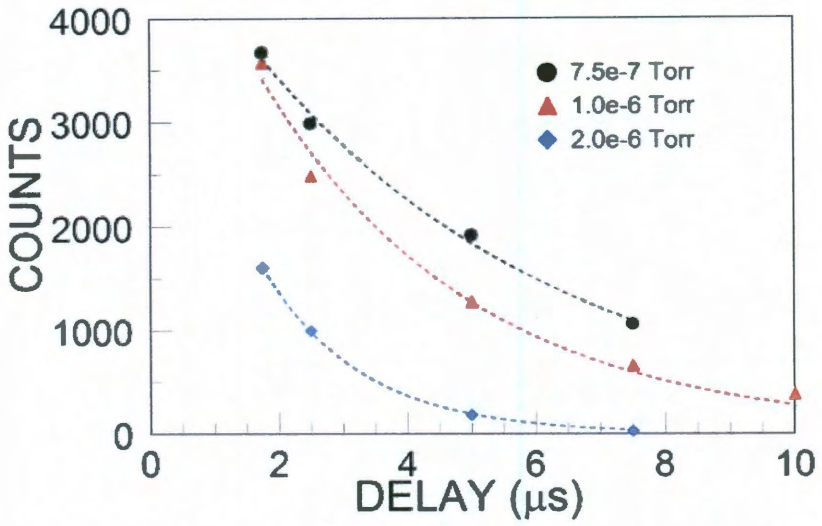

Figure 6.9 : Rydberg count rate vs H_2O background gas density. Dashed lines are exponential fits to determine decay rates. Comparison of decay rates to gas density yields $k_d \sim 10^{-5}$ cm^{3}s^{-1}.

Because polar targets have larger electron scattering cross sections, measurements were also undertaken using H_2O target gas. However, collisions between Rydberg atoms and polar targets lead to rapid collisional ionization, demonstrated in Fig. 6.9, through transfer of rotational energy to the excited electron, typically in dipole-allowed $J \rightarrow J-1$ transitions [72]. The rate constant, k_d, for such collisional destruction by H_2O at $n \sim 300$ was estimated from the decays in Fig. 6.9 to be large, $k_d \sim 10^{-5}$ cm^3/s, leading to destruction rates of $\sim 10^6$ s^{-1} at target gas densities $\rho \sim 10^{11}$ cm^{-3}. Within the framework of open quantum systems, this corresponds to a dissipative, non-unitary system which is not only open to energy exchange but also to particle number exchange, *i.e.*, the ensemble size of the system is reduced. Suppressing particle number loss by ionization requires measurements at relatively

low target densities, $< 10^{10}$ cm^{-3}. Data recorded under these conditions showed that the relative amplitude of the revivals associated with the surviving atoms was little changed. Thus, even for polar targets, decoherence associated with elastic ($\Delta J = 0$) electron scattering is slow.

Chapter 7

Conclusions and Outlook

7.1 Conclusions

This work has presented a description of the production, characterization, and manipulation of high-n, high-ℓ Rydberg wave packets. These wave packets are produced in a two step process. First, ground state alkali atoms undergo single photon excitation to very high-n Rydberg states. These states have low-ℓ due to the limited amount of angular momentum provided by photoexcitation. An external electric pump field then induces Stark precession, whereby the presence of the field breaks the symmetry of the Coulomb potential causing the angular momentum of the system to precess. Termination of the pump field at times of maximum angular momentum restores the symmetry of the Coulomb potential, in which the angular momentum is conserved, locking the Rydberg atoms into high-ℓ states. Termination of the field also causes a broadening of the initial n distribution allowing for the observation of coherent quantum dynamics as the wave packet components come into and go out of phase with each other.

A degree of control over the shape of the initial wave packet can be obtained by carefully tailoring the size and shape of the pump field. Narrow, transient spatial

localization can be achieved through application of pump fields with fast fall times and/or large amplitudes. Such states, however, have broad n distributions. Narrower n distributions can be obtained through the use of pump fields with slow fall times and/or small amplitudes.

Free evolution of these wave packets after termination of the pump field yields time-varying survival probability signals in the presence of position dependent probing. Periods of localization and delocalization are observed which reveal the existence of quantum revivals as the wave packet components periodically rephase. This large spatio-temporal coherence is unprecedented for electronic degrees of freedom involving such a large ensemble of quantum states (here $\sim$ 100 states, in contrast to spin systems which involve at most a few states). Time-domain spectroscopy of survival probability signals yields quasi-population and initial phase information for the wave packet components, giving access to a subset of off-diagonal density matrix elements that contain information on the relative phases between quantum state amplitudes. This analysis can be extended for symmetric, out of phase wave packet components, whose evolution would cancel on average, by application of probe fields whose spatial ionization threshold is located up- or down-stream of the nucleus.

Precise information on initial conditions provided by Fourier analysis acts as the starting point for manipulation of high-ℓ wave packets into carefully engineered final states. Electric field kicks provide impulsive momentum transfers that narrow or broaden energy distributions. Trains of such kicks act as driving, which stabilizes

the wave packet leading to the formation of nondispersive Bohr-like states. Slow variation of the driving period allows for the transport of wave packets in n, however, strong ℓ broadening occurs in the presence of the train, limiting the usefulness of such a technique for wavefunction engineering. Sinusoidal driving is also utilized for the production of nondispersive wave packets. The narrower phase space localization provided allows for better engineering of states, with higher transport efficiency and much less ℓ broadening.

Given the sensitivity of such high-n states to external fields and the large number of contributing quantum states, maintaining coherence over microsecond time scales for a system that extends $\sim$ 10 μm is impressive. The extent of that robustness is studied by application of external electrical noise with characteristic frequencies. Amplitude dependent line broadening and frequency dependent energy diffusion is observed, informing development of more highly refined simulation techniques. These QCTMC simulations, in turn, demonstrate that energy diffusion is the dominant source of delocalization, being particularly pronounced when the characteristic frequency of the noise is resonant with the Rydberg states. Collisions with background gases are also studied, showing little decoherence even at densities $\sim 10^{11}$ cm^{-3}.

7.2 Outlook

With the detailed characterization provided by the present work, a wide array of future studies is possible. The ℓ dependence of blackbody corrected radiative lifetimes

can be studied by premature termination of the pump field, resulting in production of elliptical wave packets with user selectable ℓ. High-n, high-ℓ wave packets also provide good laboratories in which to study atomic orbital magnetic dipole moments. Rydberg atoms can act as electron donors for low energy electron scattering experiments. High-ℓ electrons, in particular, have very narrowly defined velocity distributions which may benefit such studies.

Optimization of the sinusoidal driving techniques presented here may also lead to better transport efficiencies in the engineering of Rydberg wave packets. The frequency chirping used in the present experiments simply follows a linear dependence from n_i to n_f over the course of the experiment t_{exp}

$$f(t) = \frac{f_{n_f} - f_{n_i}}{t_{exp}} t + f_{n_i}. \tag{7.1}$$

The time dependent sinusoidal argument is, then,

$$g(t) = \int_0^t f(t')dt' = \frac{f_{n_f} - f_{n_i}}{t_{exp}} \frac{t^2}{2} + f_{n_i} t. \tag{7.2}$$

Fig. 7.1 shows CTMC simulations for such a chirp from $n_i \sim 305$ to $n_f \sim 1000$. While transfer is efficient and angular momentum remains narrowly localized, the final frequency is instantaneous. The effective final frequency, measured over the last few periods of drive, is clearly much less than $T_{n_f=1000} \approx 150$ ns for $n_f = 1000$. CTMC simulations presented in Fig. 7.2 predict a much higher effective final n state when a nonlinear chirp rate is used. Here,

$$f(t) = \frac{ct^2}{2} + \frac{f_{n_f} - f_{n_i} - \frac{1}{2}ct_{exp}^2}{t_{exp}} t + f_{n_i}, \tag{7.3}$$

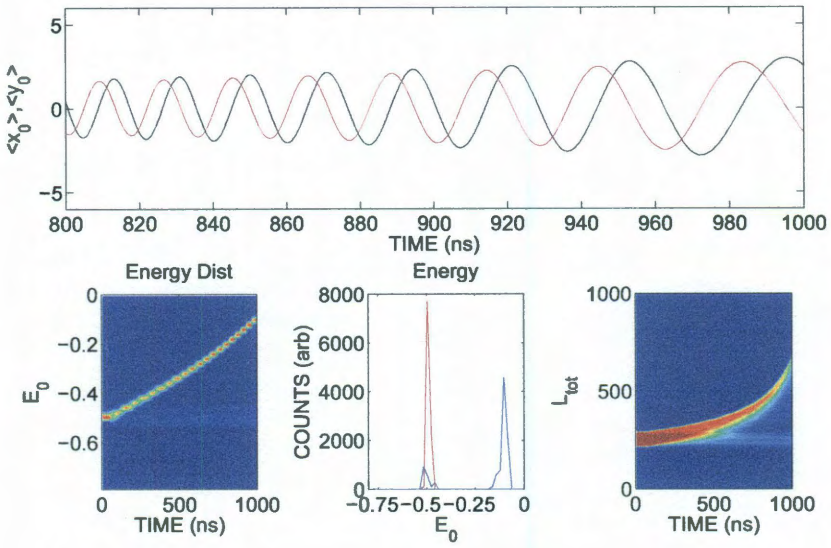

Figure 7.1 : CTMC simulations for sine chirping from $n_i \sim 305$ to $n_f \sim 1000$ at a linear rate.

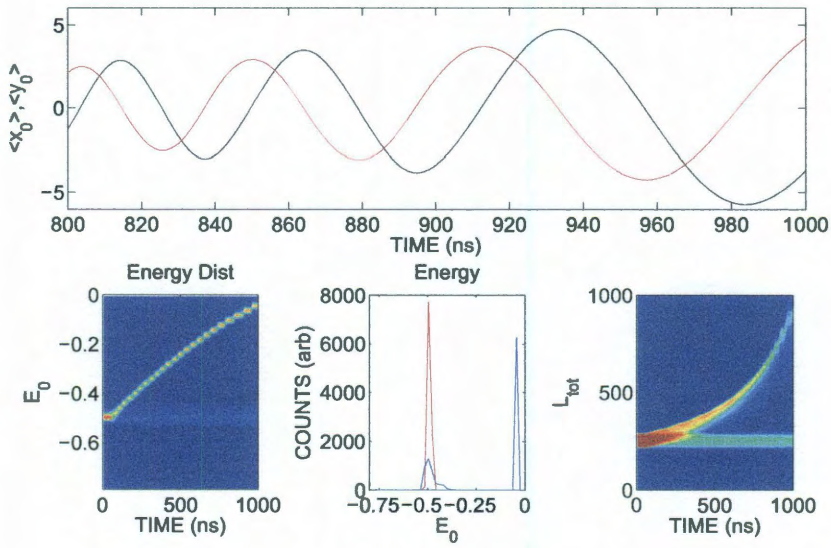

Figure 7.2 : CTMC simulations for sine chirping from $n_i \sim 305$ to $n_f \sim 1000$ at a nonlinear rate.

with adjustable parameter c. The time dependent sinusoidal argument here is

$$g(t) = \int_0^t f(t')dt' = \frac{ct^3}{6} + \frac{f_{n_f} - f_{n_i}}{t_{exp}}\frac{t^2}{2} + f_{n_i}t. \tag{7.4}$$

The empirically determined adjustable parameter used in these simulations is $c = 4 \times 10^{20}$ aut^{-3} (atomic units of time) producing a faster chirp rate at early times. Clearly the effective final period displayed in Fig. 7.2 is larger than in Fig. 7.1, however, initial pickup (and therefore transfer efficiency) is reduced. The chirp profiles chosen here, and the use of an adjustable parameter, are simply for illustrative purposes. Maximum transfer would require analysis of the energy dynamics of the driven system. Rather than transport to higher n states, the work of antihydrogen researchers would benefit from transport to lower n states [8–11]. Fig. 7.3 shows CTMC simulations chirping from $n_i \sim 305$ to $n_f \sim 250$.

Finally, multiple electrons excited to Rydberg levels in a single atom would provide a convenient laboratory in which to study systems of correlated electrons [73–75]. Control over relative initial correlation could be achieved by manipulation of the first Rydberg electron, using the techniques presented here, prior to excitation of the second. These techniques could also be applied to the entire system, possibly taking advantage of azimuthal energy correlation similar to that used with the narrowing kicks presented earlier.

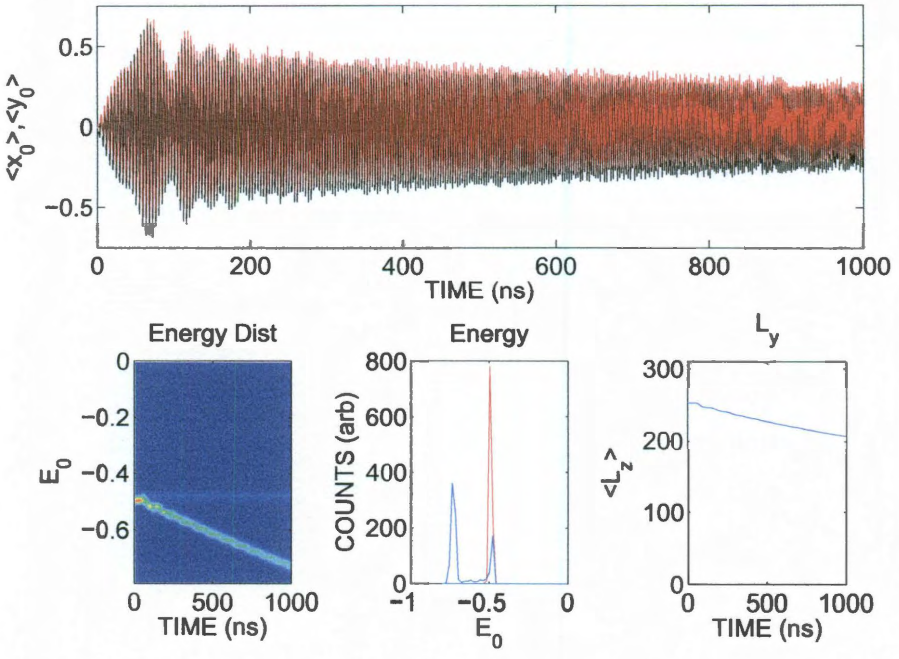

Figure 7.3 : CTMC simulations for sine chirping from $n_i \sim 305$ to $n_f \sim 250$.

Bibliography

[1] R. Bartels, S. Backus, E. Zeek, L. Misoguti, G. Vdovin, I. P. Christov, M. M. Murnane, and H. C. Kapteyn, *Nature*, **406**, 164 (2000).

[2] I. P. Christov, R. Bartels, H. C. Kapteyn, and M. M. Murnane, *Phys. Rev. Lett.*, **86**, 5458 (2001).

[3] N. L. Wagner, A. Wüest, I. P. Christov, T. Popmintchev, X. Zhou, M. M. Murnane, and H. C. Kapteyn, *Proc. Nat. Acad. Sci.*, **103**, 13279 (2006).

[4] A. V. Sokolov, D. R. Walker, D. D. Yavuz, G. Y. Yin, and S. E. Harris, *Phys. Rev. Lett.*, **85**, 562 (2000).

[5] R. A. Muniz, S. Haas, A. F. J. Levi, and I. Grigorenko, *Phys. Rev. B*, **80**, 045413 (2009).

[6] R. Carley, E. Heesel, and H. Fielding, *Chem. Soc. Rev.*, **34**, 949 (2005).

[7] M. Saffman, T. G. Walker, and K. Mølmer, *Rev. Mod. Phys.*, **82**, 2313 (2010).

[8] T. Kopyciuk and R. Parzyński, *Phys. Rev. A*, **75**, 055402 (2007).

[9] G. Gabrielse, N. S. Bowden, P. Oxley, A. Speck, C. H. Storry, J. N. Tan, M. Wessels, D. Grzonka, W. Oelert, G. Schepers, T. Sefzick, J. Walz, H. Pittner, T.

W. Hänsch, and E. A. Hessels, *Phys. Rev. Lett.*, **89**, 213401 (2002); *Phys. Rev. Lett.*, **89**, 233401 (2002).

[10] S. X. Hu and L. A. Collins, *Phys. Rev. A*, **69**, 041402 (2004).

[11] C. L. Cesar, F. Robicheaux, and N. Zagury, *Phys. Rev. A*, **80**, 041404 (2009).

[12] S. Gleyzes, S. Kuhr, C. Guerlin, J. Bernu, S. Delglise, U. Busk Hoff, M. Brune, J.M. Raimond, S. Haroche, *Nature* **446**, 297 (2007).

[13] P. Bertet, S. Osnaghi, A. Rauschenbeutel, G. Nogues, A. Auffeves, M. Brune, J. M. Raimond and S. Haroche, *Nature* **411**, 166 (2001).

[14] M. Brune, F. Schmidt-Kaler, A. Maali, J. Dreyer, E. Hagley, J. M. Raimond, and S. Haroche, *Phys. Rev. Lett.* **76**, 1800 (1996).

[15] E. Hagley, X. Matre, G. Nogues, C. Wunderlich, M. Brune, J. M. Raimond, and S. Haroche, *Phys. Rev. Lett.* **79**, 1 (1997).

[16] M. Gross and J. Liang, *Phys. Rev. Lett.* **57**, 3160 (1986).

[17] R. G. Hulet and D. Kleppner, *Phys. Rev. Lett.* **51**, 1430 (1983).

[18] C. H. Cheng, C. Y. Lee, and T. F. Gallagher, *Phys. Rev. Lett.* **73**, 3078 (1994).

[19] J. C. Day, T. Ehrenreich, S. B. Hansen, E. Horsdal-Pedersen, K. S. Mogensen, and K. Taulbjerg, *Phys. Rev. Lett.* **72**, 1612 (1994).

[20] J. Hare, M. Gross, and P. Goy, *Phys. Rev. Lett.* **61**, 1938 (1988).

[21] R. Lutwak, J. Holley, P.P. Chang, S. Paine, D. Kleppner, and T. Ducas, *Phys. Rev. A* **56**, 1443 (1997).

[22] D. Delande and J. C. Gay, *Europhys. Lett.* **5**, 303 (1988).

[23] M. T. Frey, Ph.D. Thesis, Physics & Astronomy, Rice University, (1996).

[24] S. Yoshida, Habilitationsschrift, Institute for Theoretical Physics, Technischen Universität Wien, Vienna, Austria (2007).

[25] M. T. Frey, X. Ling, B. G. Lindsay, K. A. Smith, and F. B. Dunning, *Rev. Sci. Instrum.* **64**, 3649 (1993).

[26] W. Zhao, Ph.D. Thesis, Physics & Astronomy, Rice University, (2007).

[27] H. J. Metcalf and P. van der Straten, *Laser Cooling and Trapping*, (Springer-Verlag, New York, 1999).

[28] B. G. Zollars, *CR-699-21 Single Frequency Ring Laser Alignment Manual*, (Internal Dunning Lab Documentation, Houston, TX, 1985).

[29] *Coherent CR-699 Ring Laser Manual*, (Coherent, Palo Alto, CA, 1982).

[30] B. G. Lindsay, *Superlock Manual*, (Internal Dunning Lab Documentation, Houston, TX, 1991).

[31] J. L. Hall and S. A. Lee, *Appl. Phys. Lett* **29**, 367 (1976).

[32] *Wavetrain Tunable CW Frequency Doubler User Manual*, Version 3.2, (Spectra-Physics GmbH, Berlin, 1999).

[33] R. W. Drever, J. L. Hall, et al., *Appl. Phys. B* **31**, 97 (1983).

[34] *KBL 25RS Product Documentation*, (Sjuts Optotechnik GmbH, Göttingen).

[35] T. F. Gallagher, *Rydberg Atoms* (Cambridge University Press, New York, 1992).

[36] R. F. Stebbings and F. B. Dunning, eds., *Rydberg States of Atoms and Molecules*, (Cambridge, London, 1983).

[37] M. T. Frey, F. B. Dunning, C. O. Reinhold, and J. Burgdörfer, *Phys. Rev. A.* **53**, R2929 (1996).

[38] H. Goldstein, C. Poole, and J. Safko, *Classical Mechanics*, 3rd ed., (Addison Wesley, New York, 2002).

[39] T. P. Hezel, C. E. Burkhardt, M. Ciocca, and J. J. Leventhal, *Am. J. Phys.*, **60**, 324 (1992).

[40] H. E. White, *Introduction to Atomic Spectra*, (McGraw-Hill, New York and London, 1934).

[41] Richard Morris (Salix alba), distributed under the GNU Free Documentation License Version 1.2.

[42] H. A. Bethe and E. E. Salpeter, *Quantum Mechanics of One- and Two-Electron Atoms*, (Springer-Verlag, Berlin, 1957).

[43] M. L. Zimmerman, M. G. Littman, M. M. Kash, and D. Kleppner, *Phys. Rev. A*, **20**, 2251 (1979).

[44] C. O. Reinhold, M. Melles, H. Shao, and J. Burgdörfer, *J. Phys. B*, **26**, L659, (1993).

[45] B. E. Tannian, C. L. Stokely, F. B. Dunning, C. O. Reinhold, and J. Burgdörfer, *Phys. Rev. A*, **64**, 021404 (2001).

[46] C. L. Stokely, J. C. Lancaster, F. B. Dunning, D. G. Arbó, C. O. Reinhold, and J. Burgdörfer, *Phys. Rev. A* **67**, 013403 (2003).

[47] S. Yoshida, private communication.

[48] W. Zhao, J. C. Lancaster, F. B. Dunning, C. O. Reinhold, and J. Burgdörfer, *Phys. Rev. A*, **69**, 41401 (2004).

[49] R. Loudon, *The Quantum Theory of Light*, 3^{rd} ed., (Oxford University Press, New York, 2000).

[50] C. E. Theodosiou, *Phys. Rev. A*, **30**, 2881 (1984).

[51] F. Gounand, *J. Phys. (Paris)*, **40**, 457 (1979).

[52] D. Kleppner, *Phys. Rev. Lett.*, **47**, 233 (1981).

[53] A. G. Vaidyanathan, W. P. Spencer, and D. Kleppner, *Phys. Rev. Lett.*, **47**, 1592 (1981).

[54] R. G. Hulet, E. S. Hilfer, and D. Kleppner, *Phys. Rev. Lett.*, **55**, 2137 (1985).

[55] M. R. Flannery, *Phys. Rev. A*, **22**, 2408 (1980).

[56] E. de Prunelé and J. Pascale, *J. Phys. B*, **12**, 2511 (1979).

[57] M. R. Flannery, *Ann. Phys.*, **61**, 465 (1970).

[58] M. Matsuzawa, *J. Phys. B*, **8**, 2114 (1975).

[59] I. I. Fabrikant, *J. Phys. B*, **17**, 4223 (1984).

[60] F. G. Kellert, Ph.D. Thesis, Physics & Astronomy, Rice University (1980).

[61] J. Hirschfelder, H. Eyring, and B. Topley, *J. Chem. Phys.*, **4**, 170 (1936).

[62] R. Arbines and I. Percival, *Proc. Phys. Soc. London*, **88**, 861 (1966).

[63] C. O. Reinhold and C. A. Falcón, *Phys. Rev. A*, **33**, 3859 (1986).

[64] B. Wyker, S. Ye, T. J. McKinney, F. B. Dunning, S. Yoshida, C. O. Reinhold, and J. Burgdörfer, "Decoherence of high-ℓ Rydberg wave packets", *J. Phys. B*, (in press, 2011).

[65] C. O. Reinhold, S. Yoshida, J. Burgdörfer, J. J. Mestayer, B. Wyker, J. C. Lancaster, and F. B. Dunning, *Phys. Rev. A*, **78**, 063413 (2008).

[66] E. A. Shapiro, *J. Exp. Theo. Phys.*, **91**, 449, 2000.

[67] S. Yoshida, C. O. Reinhold, J. Burgdörfer, B. Wyker, and F. B. Dunning, *Phys. Rev. A*, **81**, 063428 (2010).

[68] J. J. Mestayer, B. Wyker, F. B. Dunning, S. Yoshida, C. O. Reinhold, and J. Burgdörfer, *Phys. Rev. A*, **79**, 033417 (2009).

[69] S. H. Strogatz, *Nonlinear Dynamics and Chaos: With Applications to Physics, Biology, Chemistry, and Engineering*, (Perseus Books, Reading, MA, 1994).

[70] S. Yoshida, C. O. Reinhold, J. Burgdörfer, W. Zhao, J. J. Mestayer, J. C. Lancaster, and F. B. Dunning, *Phys. Rev. A*, **75**, 013414 (2007).

[71] C. O. Reinhold, J. Burgdörfer, and F. B. Dunning, *Nuc. Instr. Meth. B*, **233** 48 (2005).

[72] S. B. Hill, M. T. Frey, F. B. Dunning, and I. I. Fabrikant, *Phys. Rev. A*, **53**, 3348 (1996).

[73] F. Robicheaux and R. C. Forrey, *J. Phys. B*, **38**, S363 (2005).

[74] S. N. Pisharody and R. R. Jones, *Science*, **303**, 813 (2004).

[75] C. Såthe, M. Ström, M. Agåker, J. Söderström, J. E. Rubensson, R. Richter, M. Alagia, S. Stranges, T. W. Gorczyca, and F. Robicheaux, *Phys. Rev. Lett.*, **96**, 043002 (2006).

Appendix A

List of Publications

1. "Realization of Localized Bohr-Like Wave Packets", J. J. Mestayer, B. Wyker, J. C. Lancaster, F. B. Dunning, C. O. Reinhold, S. Yoshida, and J. Burgdörfer, *Phys. Rev. Lett.*, **100**, 243004 (2008).

2. "Generation of quasiclassical Bohr-like wave packets using half-cycle pulses", J. J. Mestayer, B. Wyker, F. B. Dunning, C. O. Reinhold, S. Yoshida, and J. Burgörfer, *Phys. Rev. A*, **78**, 045401 (2008).

3. "Tailoring very-high-n circular wave packets", C. O. Reinhold, S. Yoshida, J. Burgdörfer, J. J. Mestayer, B. Wyker, J. C. Lancaster, and F. B. Dunning, *Phys. Rev. A*, **78**, 063413 (2008).

4. "Creation of nondispersive Bohr-like wave packets", J. J. Mestayer, B. Wyker, F. B. Dunning, S. Yoshida, C. O. Reinhold, and J. Burgdörfer, *Phys. Rev. A*, **79**, 033417 (2009).

5. "Large-scale quantum coherence of nearly circular wave packets", C. O. Reinhold, S. Yoshida, J. Burgdörfer, B. Wyker, J. J. Mestayer, and F. B. Dunning, *J. Phys. B*, **42**, 091003 (2009).

6. "Long-time quantum coherence of near-circular wavepackets", S. Yoshida, C. O. Reinhold, J. Burgdörfer, J. J. Mestayer, B. Wyker, and F. B. Dunning, *J. Phys. Conference Series*, **194**, 032022 (2009).

7. "Creation of non-dispersive Bohr-like wavepackets", J. J. Mestayer, B. Wyker, F. B. Dunning, S. Yoshida, C. O. Reinhold, and J. Burgdörfer, *J. Phys. Conference Series*, **194**, 032028 (2009).

8. "Encoding and decoding phase information in high-n circular wave packets", S. Yoshida, C. O. Reinhold, J. Burgdörfer, B. Wyker, and F. B. Dunning, *Phys. Rev. A*, **81**, 063428 (2010).

9. "Decoherence of high-ℓ Rydberg wave packets", B. Wyker, S. Ye, T. J. McKinney, F. B. Dunning, S. Yoshida, C. O. Reinhold, and J. Burgdörfer, *J. Phys. B*, (in press, 2011).

10. "Probing the spatial distribution of high angular momentum Rydberg wave packets", B. Wyker, S. Ye, F. B. Dunning, S. Yoshida, C. O. Reinhold, and J. Burgdörfer, (in preparation, 2011).

11. "Transporting near-circular Bohr-like wave packets using chirped sine waves", B. Wyker, S. Ye, F. B. Dunning, C. O. Reinhold, S. Yoshida, and J. Burgdörfer, (in preparation, 2011).

12. "Experimental Measurement of Turnstiles as a Chaotic Ionization Mechanism

in Rydberg Atoms", K. Burke, K. A. Mitchell, B. Wyker, S. Ye, and F. B. Dunning, (in preparation, 2011).

13. "Ionization of kickced Rydberg atoms via a turnstile mechanism", K. Burke, K. A. Mitchell, B. Wyker, S. Ye, and F. B. Dunning, (in preparation, 2011).

Appendix B

Units

B.1 Atomic Units

The system of atomic units, particularly useful when considering atoms and electrons, is used in the current work. Each of the following is equal to one in atomic units:

Angular Momentum	Planck's Constant, $\hbar$	1.055×10^{-34} J s
Charge	Electron Charge, q	1.602×10^{-19} C
Mass	Electron Mass, m_e	9.109×10^{-31} kg
Length	Bohr Radius, a_0	5.292×10^{-11} m
Energy	Hartree Energy, E_h	4.360×10^{-18} J $= 27.2$ eV
Time	$\frac{\hbar}{E_h}$	2.419×10^{-17} s
Coulomb's Constant	$\frac{1}{4\pi\epsilon_0}$	8.988×10^{9} Nm^2/C^2

B.2 Scaled Units

The following scaled units are used in the current work:

$$\vec{r}_0 = \frac{\vec{r}}{n^2}$$

$$\vec{p}_0 = n\vec{p}$$

$$t_0 = \frac{t}{2\pi n^3}$$

$$\omega_0 = n^3\omega$$

$$E_0 = n^2 E$$

$$F_0 = n^4 F$$